UNIVERSITY OF LIVERPOOL

Single Multimode Fibre Imaging

by

Liang Deng

MEng, BSc

A thesis submitted in accordance with the requirements for the award of the degree of *Doctor of Philosophy* of the University of Liverpool

September 2017

I would like to dedicate this thesis to my loving girlfriend and parents.

Declaration

I hereby declare that except where specific reference is made to the work of others, the contents of this dissertation are original and have not been submitted in whole or in part for consideration for any other degree or qualification in this, or any other University. This dissertation is the result of my own work and includes nothing which is the outcome of work done in collaboration, except where specifically indicated in the text.

Liang Deng

2017

Acknowledgements

Looking back on my four-year PhD time, I am very grateful to a number of persons. First of all, I would like to thank my supervisor Dr Lei Su. I really appreciate your guidance and help during the four years and I have learnt a lot from you both academically as well as personally. Also, thank you for those valuable comments and suggestions on my research and my life. It is my great honour to work with you as a PhD student and I hope I am in line with your expectation. Secondly, I need to thank the other supervisor Prof. Joseph Yan for your kind support and academic guidance on this project.

Also, I would like to thank my girlfriend and parents. Your love and support have always been with me during the four years and I know they will always be there. This work is dedicated to you. Special thanks are also given to my bright and lovely friends: Zhouxiang Fei, Zhihao Tian, Chaoyun Song, Chongyang Liu, Jiajia Zhao, Jinshuai Zhang, Michael Ruddlesden, Karen Blankenagel. Thank you all for insightful discussions and joyful moments.

Last but not the least, the financial support from the University of Liverpool and the experimental setup and the computation facilities at Queen Mary University of London are highly appreciated.

Table of Contents

Table of Figures

Abbreviations

AI	Artificial Intelligence
ANN	Artificial Neural Network
CNN	Convolutional Neural Network
DMD	Digital Micromirror Device
ED	Eigenvalue Decomposition
EF	Enhancement Factor
EXP	Expectation
FBG	Fibre Bragg Grating
GI	Generalised Inverse
IP	Image Plane
LSV	Left-singular vector
MMF	Multimode Fibre
NA	Numerical Aperture
OP	Object Plane
prVBEM	phase retrieval Variational Bayes Expectation Maximization
RI	Regular Inverse

RSV	Right-singular vector
SLM	Spatial Light Modulator
SMF	Single Mode Fibre
STD	Standard Deviation
SVD	Singular Value Decomposition
TM	Transmission Matrix
VB-EM	Variational Bayes Expectation Maximization

List of Publications

Journal Publications

[1] **L. Deng**, J. Yan, D. Elson and L. Su, "Characterization of an imaging multimode optical fiber using digital micro-mirror device based single-beam system," *Optics Express* (Accepted).

[2] **L. Deng**, Y. Wang, C. Liu, D. Hu, P. Shum and L. Su, "Plasmonic nanopore-based platforms for single-molecule Raman scattering," *Optics Communications* **372**(1), 113-117 (2016).

[3] C. Liu*, **L. Deng***, D. Liu and L. Su, "Modeling of a Single Multimode Fiber Imaging System," *arXiv*:1607.07905 (2016).

Conference Publications

[1] **L. Deng,** C. Liu, L. Song, J. Yan and L. Su, "Design of Single-Shot Multimode Fiber Based Endoscope," in *Conference on Lasers and Electro-Optics*, 2016, JTu5A.98.

[2] **L. Deng**, Y. Wang, Z. Shen, C. Liu, D. Hu, P. Shum and L. Su, "Design of Plasmonic Nanopore Platforms for Single-Molecule Detection," in *Asia Communications and Photonics Conference*, 2014, ATh1l.5.

Abstract

Multimode fibre can be a promising imaging component candidate since it is with small cross section and supports a great number of spatial modes. But it cannot be used directly due to complex mode coupling and mode dispersion taking place during light propagation. In order to make the most of its advantages and to develop single multimode fibre imaging system, work is carried out on the following three topics: modelling of single multimode fibre imaging system, reference-less characterisation of multimode fibre imaging system and analysis on transmission matrix of the multimode fibre imaging system.

Firstly, free space optics and fibre optics are used to construct a theoretical model for our single fibre imaging system. Without losing generosity, light coupling from free space into a multimode fibre and that of fibre spatial modes are included in the model. Fibre characterisation is simulated with our model and corresponding transmission matrices is obtained. It is also demonstrated that original patterns could be well retrieved with the help of transmission matrix as it is able to undo the distortion inside multimode fibres. In addition, it is demonstrated that the multimode fibre imaging system is sensitive to environmental change such as bending since such change would change mode coupling situations. Moreover, a single-shot multimode fibre endoscope based on DMD is proposed. The critical part is to generate known illumination field on the object and to collect the backward light with the same multimode fibre. This backward field is processed with recorded TM and the effect of illumination field is removed to recover the original patterns finally.

Secondly, a Bayesian inference based algorithm is developed to infer the phase information in fibre output fields. Normally, phase information is obtained by holography as the camera can only record field intensity. Since holography is extremely sensitive to environmental change, it is widely used in sensing applications but is problematic in our imaging setup. In order to address the problem of unstable conditions, output images are recorded without reference beam and processed the data with the algorithm. In this way, the transmission matrix of multimode fibre imaging system is achieved successfully without holography. In order to validate the transmission matrix, our results are tested by three criterion. Firstly, it is shown that TM-predicted output images were highly in line with actual recorded output images for arbitrary input patterns. Secondly, original patterns are retrieved with the help of the recorded TM and

demonstrated that the system imaging resolution is diffraction limited. Thirdly, the information in transmission matrix is utilised to generate a clean focus on the distal fibre end and scanned the focus across it. It is shown that the enhancement factor could be 70 and it is not uniform across the fibre end. Further improvement is expected with more precise modulation device such as SLM.

Thirdly, extensive data analysis on the obtained transmission matrices is carried out to extract further insights from them. Firstly, it is shown that one is able to measure the number of travelling modes in multimode fibre by calculating the effective rank of its transmission matrix since spatial modes are degrees of freedom in the imaging system and rank indicates the transmission matrix's degrees of freedom. Secondly, it is disclosed that eigenchannels for a specific multimode fibre are achievable by performing singular value decomposition for its transmission matrix. The energy delivery efficiency was improved by 50% in the experiment and can be further enhanced by more accurate modulation device such as SLM. Thirdly, it is shown that the TM would experience severe change with additional fibre bending and that the TM phase change is much more apparent than that of TM amplitude.

The work in this thesis has demonstrated successfully novel and practical implements of single multimode fibre imaging systems as complements to current approaches. Moreover, further insights have been extracted from transmission matrix to understand the physical process from different angles and to open new ways for broad applications. The results presented in this thesis should have enriched research contents on this topic and have arisen research interests in further developments in this area.

Chapter 1 Introduction

In this opening chapter, a brief introduction of the research topic and background will be given. Specifically, the reasons for distorted images and needs for special imaging components are introduced concisely. Moreover, a literature review was carried out on imaging through scattering media as well as multimode fibres. In the last section, this chapter is closed with the introduction of our work on multimode fibre imaging.

1.1 Distorted images

Everyone is performing imaging in daily life but probably even without realising it. For instance, the readers are using their own imaging systems to read this thesis. The readers' eyes and possibly a pair of glasses or contact lenses are actually components of the imaging system enabling them to see the content.

What happens when observing the object is basically as follows. The light from the source is reflected by the object and its information is embedded in the reflected wavefront. The wave carrying object information goes through space before arriving our eyes. But this wavefront does not remain unchanged. An optical field propagating in free space can be described by diffraction equations. From basic geometrical optics, it is known that a single lens is enough to do imaging. An optical lens can undo such transformation and retrieve the original object information. This is exactly what one's eyes do when seeing as illustrated in Fig. 1.1. The lens in normal eyes can adjust itself to focus the light on the retina while problematic eyes can be short-sighted or far-sighted. Another interesting fact is that the image on the retina is upside down. But humans are not seeing a rotated world due to smart brain processing.

However, if the distortion is more complicated than linear transformation, our eyes are not sufficient to retrieve the object information. This is what one experiences if trying to observe through fog or a piece of frosted glass. Fig. 1.2 is a picture taken by Janice Fairhurst on Flickr.

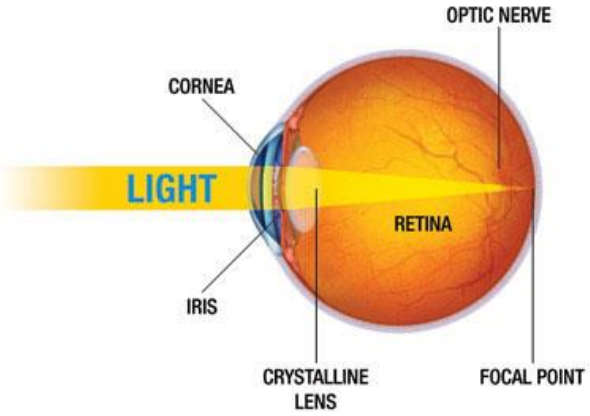

Fig. 1.1. A schematic diagram of working principle of human eyes, © 2016 NKCF.

The fence and plants at the near end can be clearly seen as the light is basically propagating in the air. However, the light reflected by the trees in the background has to go through the small water droplets in the air to reach our eyes or camera. Since the light is scattered in different directions each time it meets a water droplet, its propagation becomes very complicated and the field reaches sensors is distorted. If one still observe with a lens-based imaging system, he/she will end up with seeing part of the objects (such as the trees in the centre of background) or not seeing them at all. Since the distortion is not a linear transformation anymore, the inverse transformation by the lens in our eyes is not correct and will not help generate any meaningful images for the brain.

Fig. 1.2. A picture taken in fog by Janice Fairhurst, © 2017 Flickr.

The airspace with water droplets on a foggy day is behaving as the so-called scattering media. And it is almost impossible to image through it with conventional lenses. Biological tissue is also an example of scattering media since inhomogeneities in the tissue scramble the optical wavefront, making it is hard to observe tissue parts in deep layers with traditional optical components such as lenses.

1.2 Observing behind scattering media

As experienced during a foggy day, light scattering severely affects our ability to see. One special approach to address the distortion issue is to utilise the ballistic photons which travel through the media without being scattered by inhomogeneities. These ballistic photons would leave the media earlier than the non-ballistic counterparts that would experience scattering when travelling through the media. Therefore, the distortion of images due to scattering can be averted if one only captures ballistic photons by gated approaches such as optical coherence tomography[1-3]. This method is straightforward but the propagation distance of ballistic light in strongly scattering media is quite limited (around 1 mm in biological tissues). So image quality would experience severe degradation if one would like to observe tissues deep inside[4,5].

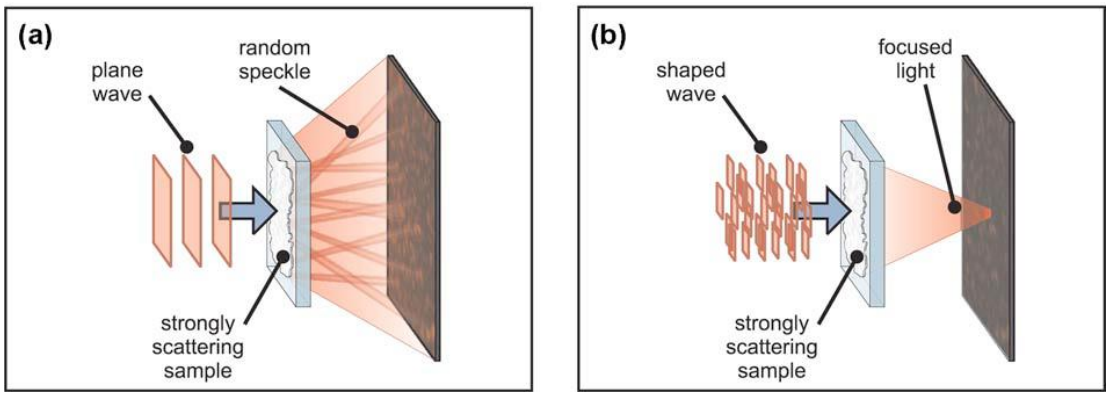

Fig. 1.3. Experiment design to generate a focus through a scattering media. (a) A plane wave is propagating through the scattering media, resulting in speckle patterns. (b) The input field is shaped in order to generate a focus. Adapted from Ref[6], © 2007 OSA.

Although the light scattering in the media seems random, it is actually a deterministic process. Therefore it is possible to construct a predictive model to build a connection between objects and corresponding images. Wavefront shaping technology has been studied extensively in the past decade to characterise scattering media and to turn it into useful imaging component. It was demonstrated by Vellekoop and Mosk[6,7] that light can be concentrated into a clear focus

through strongly scattering media by controlling the wavefront with a spatial light modulator (SLM). Normally, random input fields will generate the so-called speckle patterns after propagating through the scattering media. In order to inverse diffusion wavefront, the authors utilised a direct search algorithm to find the necessary input field which can result in a focus behind the scattering media. Their experiment design is shown in Fig. 1.3 where the outputs for plane wave and shaped wave are clearly compared.

With proper modulation, it is demonstrated possible to focus the light. Considering the SLM has N pixels, then the output field on a specific position, E_m, is a weighted linear combination of all the N fields on the SLM:

$$E_m = \sum_{n=1}^{N} t_{mn} A_n e^{j\phi_n} \tag{1-1}$$

where A_n stands for amplitude for each mode and the detailed scattering process determines the coefficients t_{mn}. The phase of each mode ϕ_n is modulated by the SLM and the purpose is to find an optimal set of ϕ_n to undo the effect brought by t_{mn} and to produce a clean focus. The authors assigned phase between 0 and 2π for each SLM pixel and recorded the corresponding phase which can lead to the highest intensity at the target position. The overall phase pattern was confirmed after this was done for all the pixels. It was also demonstrated that the enhancement of the focus depends on the count of pixels used to modulate input field. This pioneering work also arose research interests of the photonics community in seeing through scattering media where conventional imaging components are not able to retrieve information.

The same group further demonstrated that the focus generated through scattering media can be even sharper[8] than that produced by conventional lens since the scattering process can capture more high order modes, leading to the higher numerical aperture (NA). They utilised this technique to produce a scanning sub-100 nm focus and to image gold nanoparticles at sub-100 nm resolution[9]. With precise wavefront control, scattering media was successfully transformed to work as a conventional optical lens. In addition, the light transmission through complex media in both space and time is studied by the group for applications such as coherent control, focusing and imaging[10,11]. With wavefront shaping technology, strongly scattering media was also studied to send more power[12], to perform temporal and spatial focusing[13,14] and to work as mirrors[15], wave-plates[16] and optical manipulators as well as tweezers[17,18].

Phase conjugation has been investigated to focus light by Yang's group[19-23] over the past years. Thanks to the reciprocity of light propagation, one can generate input wavefront by using the phase conjugation of corresponding output wavefront through the scattering medium. In 2002, Vellekoop *et al*. utilised this approach to focus light and to enhance fluorescence[21]. Its principle is illustrated in Fig. 1.4. Basically, the scattered fluorescence light is recorded and its phase conjugation is generated to produce a focus on the target to enhance fluorescence.

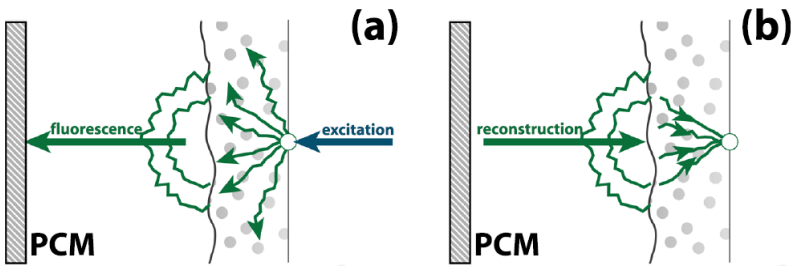

Fig. 1.4. The principle of phase conjugation fluorescence. (a) The fluorescence target is excited and its fluorescence light is scattered by the medium and collected by the phase-conjugating mirror (PCM). (b) The PCM produces conjugated wavefront which refocuses on the fluorescence target. Adapted from Ref[21], © 2012 AIP.

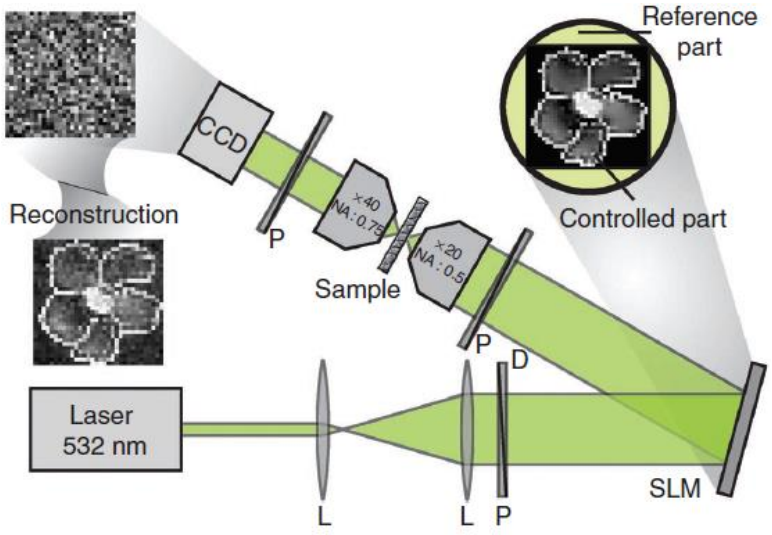

Fig. 1.5. Experimental setup to measure the transmission matrix of a scattering media. The laser light is expanded by two lenses and modulated by the SLM. The phase-modulated beam goes through the scattering media and the output speckles are captured by the CCD camera. L: lens, P: polarizer, D: diaphragm. Adapted from Ref[26], © 2010 MPL.

Another extensively investigated direction is to characterise scattering media by recording its so-called transmission matrix (TM) which could describe its full transmission characteristics[24,25]. In 2010, Popoff and coworkers introduced a method to measure the transmission matrix of complex media[24]. They used SLM to modulate input fields and utilised

phase-shift holography to obtain full information of output fields. The TM was constructed with sufficient calibration measurements and was used to perform focusing as well as detection. Further, the same group demonstrated image transmission through a scattering media[26]. By using the measured TM, they were able to reconstruct arbitrary images through the complex media. Their experimental setup is illustrated in Fig. 1.5.

The same group also demonstrated compressive imaging using a scattering media[27] with the experimental setup shown in Fig. 1.6. This method is different from other more classical compressive imagers using pseudo-random projections since it involves the calibration step, which can be done in a few minutes and can be accelerated by parallel measurement or using digital mirror device. Other related works include invariance property[28] of the scattered wavefront and spectral control of scattered broadband light by wavefront shaping[29] or multispectral transmission matrix[30].

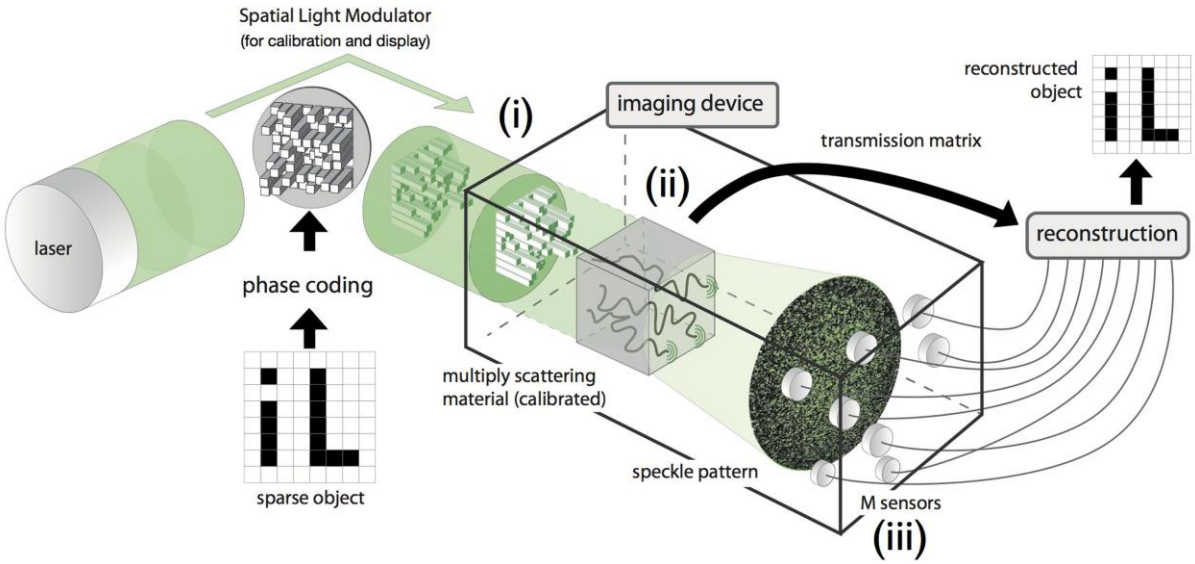

Fig. 1.6. Experimental setup for compressive imaging with scattering media. The laser beam is modulated by the SLM (i) before going through the scattering material (ii) which scrambles the information into M sensors (iii). With the measured transmission matrix of the media, image reconstruction can be achieved with a limited count of sensors which can be much smaller than that without the scattering media. Adapted from Ref[27], © 2014 MPL.

In addition to in-line holography, off-axis setup was also studied extensively to measure the transmission matrix of scattering media[31,32]. In 2011, Choi and co-workers measured the TM[33] by using a scanning mirror and off-axis holography based on their work on speckle-field digital holographic microscopy[34]. Here, the modulator was the scanning mirror which was used to generate different plane waves for calibration. The main disadvantage of this setup is that it is

necessary to measure the input field produced by the scanning mirror without the scattering media. It means two sets of scanning are needed to finish the calibration. Off-axis holography was utilised as a straightforward method to retrieve phase information since it does not require additional phase-shifted measurements or phase retrieval algorithms. Their imaging principle is shown in Fig. 1.7. In short, angular responses are recorded to construct TM which can inverse distortion in the imaging step.

Furthermore, the same group proposed synthetic aperture microscopy[35] to enhance system resolution by taking a number of distorted images during the imaging step (step (c) in Fig. 1.7). Since the object is imaged with a set of plane waves, system numerical aperture is effectively increased, leading to higher resolution. Also, they improved light energy delivery through scattering medium by studying time-resolved reflection matrix[36] as well as eigenchannels[37,38] of the media.

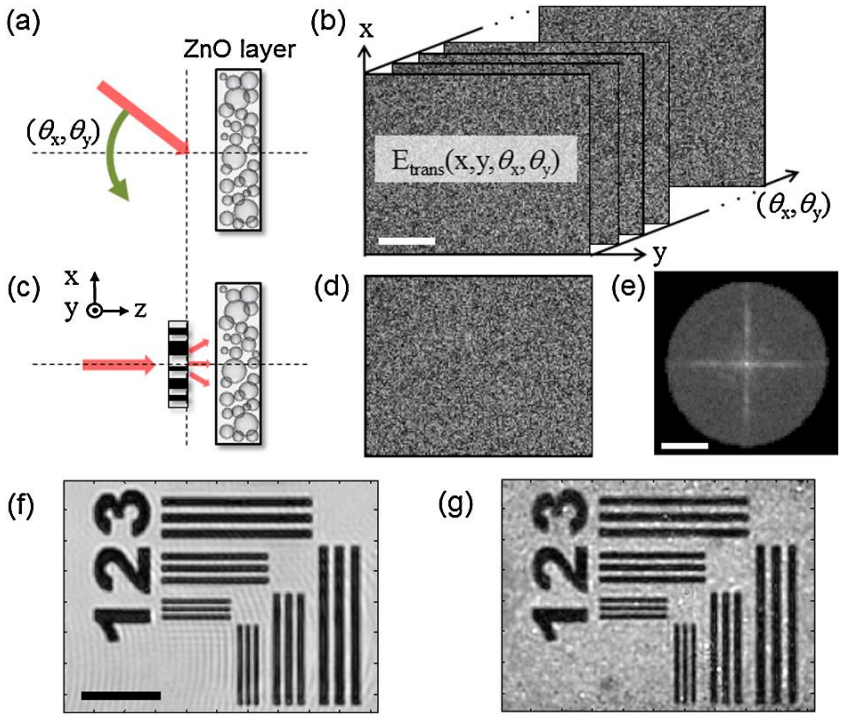

Fig. 1.7. Schematic of turbid lens imaging. (a) Measuring transmission matrix for a scattering media. Plane waves with different incident angle go through the media and corresponding output fields are recorded. (b) Transmission matrix is constructed with recorded information. (c) Measuring the image of a resolution target. (d) The acquired distorted image. (e) Fourier spectrum of the image in (d). (f) Original object. Scale bar: 0.5 um. (g) Reconstructed object. Adapted from Ref[33], © 2011 APS.

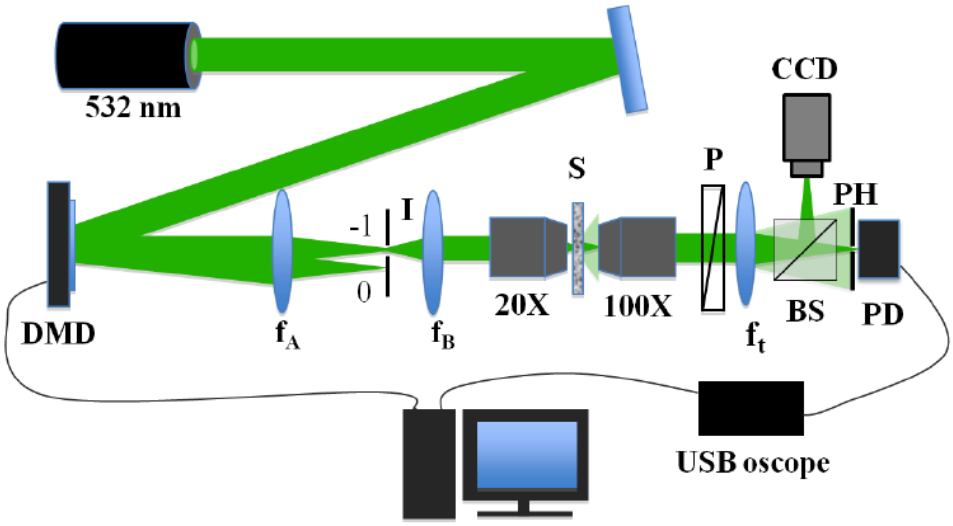

Fig. 1.8. Experiment setup for real-time characterisation. The laser beam is modulated with Lee binary amplitude holograms using a DMD to generate desired phase patterns on the scattering medium. The iris (I) is used to filter light in unwanted orders. S: scattering media. P: polarizer. BS: beamsplitter. PH: pinhole. PD: photodetector. Adapted from Ref[39], © 2012 OSA.

In terms of implementation, one may want to calibrate the system as fast as possible for the time reason and for averting possible problems due to instability. Speaking of speed, the most advantageous modulation component is a digital micro-mirror device (DMD). It can operate at over 10 kHz which is much quicker than SLM (50 Hz typically). In 2012, Conkey and co-workers demonstrated real-time TM acquisition[39] of scattering media and focus generation through it. By using a DMD as the modulator, they successfully measured TM with 256 input modes in 33.8 ms and produced a clean focus whose signal to background ratio was 160. Their experimental setup is presented in Fig. 1.8. Note that the DMD was actually used as an SLM to offer phase modulation here. In this way, one can have efficient phase modulation as well as the high speed of DMD. This is realised by using the Lee method[40] where the amplitude hologram $t(x, y)$ encoding the designed phase pattern $\varphi(x, y)$ is given as

$$t(x,y) = 0.5[1+\cos(2\pi(x-y)\alpha - \varphi(x,y))] \tag{1-2}$$

where α is carrier frequency, x and y denote spatial coordinates. The carrier frequency needs to be selected to provide enough separation between the 1st-order light and the 0th-order light. The binary amplitude hologram $h(x, y)$ that can be expressed by the DMD is achieved by thresholding the calculated amplitude hologram $t(x, y)$:

$$h(x,y)=\begin{Bmatrix}1;t(x,y)>0.5\\0;else\end{Bmatrix} \tag{1-3}$$

The desired phase pattern is produced in the -1st-order light. So the iris on Fourier plane can block all the light in other orders. After another Fourier transform by the following lens, the desired phase image $\varphi(x, y)$ is generated. The calibration process is similar to that in Ref[33] and can be finished in tens of milliseconds thanks to the high speed of DMD. Moreover, Nixon *et al*. demonstrated that complex field required to produce a clean focus through the turbid medium can be generated within 1 ms by all-optical feedback[41].

In addition, memory effect in scattering media has been investigated towards non-invasive imaging[42-45]. In 2014, Katz and coworkers demonstrated single-shot imaging through scattering media via speckle correlations[44]. The idea is briefly expressed in Fig.1.9. Although the raw image seems random and information-less, its autocorrelation is actually identical to object autocorrelation, thanks to the angular memory effect[46-48]. The memory effect indicates that light from close points is scattered by the turbid material to generate highly correlated but shifted speckle patterns. For incoherent illumination, since there is no interference between speckle patterns, the image is a superposition of these correlated and shifted patterns. Therefore the system has a shift-invariant point spread function (PSF) within memory effect range. The camera image $I(y)$ is expressed as the convolution:

$$I(\theta)=O(\theta)*S(\theta) \tag{1-4}$$

where (*) denotes convolution, O is object pattern and S stands for the point spread function. Further, one can have the autocorrelation of camera image as:

$$\begin{aligned}&[I\otimes I](\theta)=[(O*S)\otimes(O*S)](\theta)\\&=[(O\otimes O)*(S\otimes S)](\theta)\approx O\otimes O(\theta)\end{aligned} \tag{1-5}$$

where ($\otimes$) denotes autocorrelation. Since the autocorrelation of the PSF is a sharply peaked[49] as autocorrelation of random noise, the autocorrelation of the camera image is nearly that of the object. This autocorrelation is further processed with Fienup phase retrieval algorithms[50] to produce the final reconstructed image.

Also in 2014, Katz *et al*. demonstrated two-photon fluorescence imaging through scattering

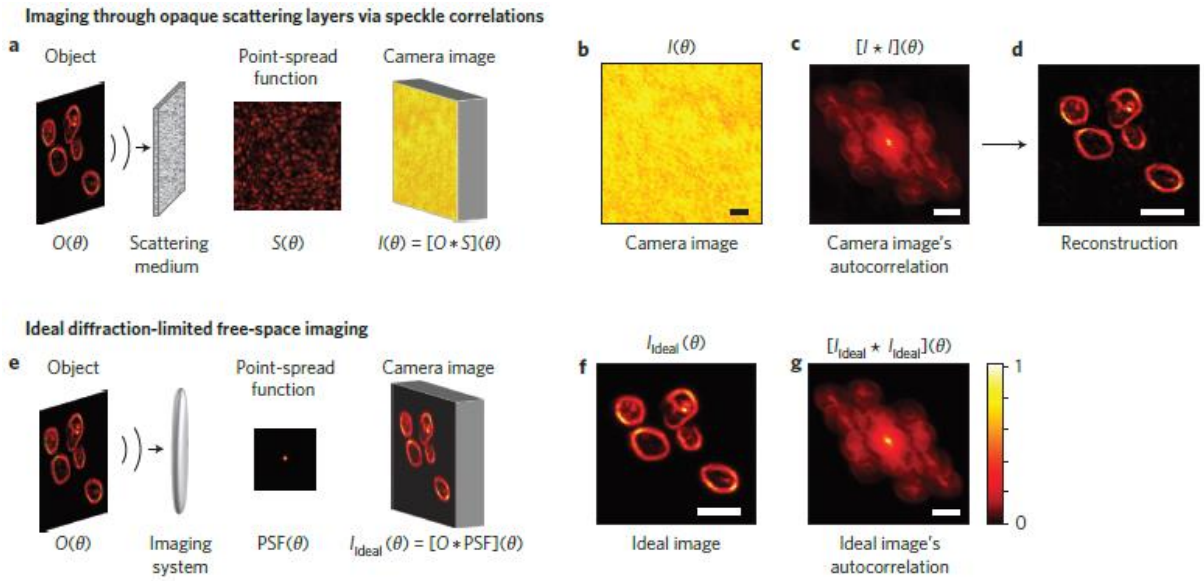

Fig. 1.9. Single-shot imaging through scattering media via speckle correlations: concept and examples. (a) Experimental setup: The object is illuminated with an incoherent narrowband source and the camera measures the distorted image on the other side of the turbid media. (b) Raw camera image which is expressed as the convolution of the intensity pattern of the object and a random speckle pattern. (c) The autocorrelation of the raw image is equivalent to that (g) of the object pattern. (d) Reconstructed image from (c) by a phase-retrieval algorithm. (e) The experimental setup where the scattering medium is replaced with a lens. (f) Ideal image for (e). (g) Autocorrelation of (f). Adapted from Ref[44], © 2014 MPL.

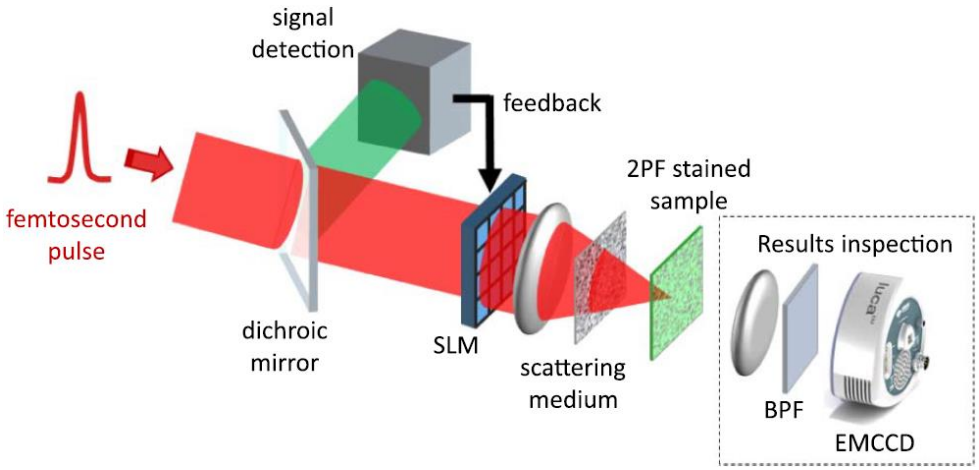

Fig. 1.10. Experimental setup for non-invasive nonlinear focusing and imaging. 100-fs pulses are modulated by the SLM to generate a focus on the two-photon fluorescence sample. The backward signal is collected and used for genetic algorithm optimisation. Adapted from Ref[45], © 2014 OSA.

media without access to the distal end[45]. The experimental setup is shown in Fig. 1.10. The SLM is used to modulate the field going through the scattering medium. The two-photon fluorescence sample is excited and the backward fluorescence signal is monitored. Note that the EMCCD camera is used to inspect results but is not involved in the SLM modulation. By

using genetic algorithm[51], the optimal phase mask is found to generate a focus on the sample. Since nonlinear fluorescence is used here, a produced focus on sample leads to maximum backward fluorescence power. Although genetic algorithm can result in a clean focus on the sample, its position is not controlled. With the help of memory effect, the focus can be scanned by using the SLM as a scanner[52]to generate a microscopic image. Therefore the field of view of this approach is limited by the range where memory effect is valid.

1.3 Seeing through multimode fibre

Fibre imaging is widely used in biomedical endoscopy thanks to its small cross section and flexibility. Normally, this is realised with a bundle of single-mode fibres[53,54] where each fibre core is contributing as a pixel in the observed image. Since there is only one spatial mode travelling in each core, the object information is well preserved even with fibre geometry changes, making it suitable for real applications. However, an obvious drawback of this method is that there is inevitable spacing between fibre cores. As the light is guided in the cores, the object parts not collected by the cores cannot be observed, leading to the so-called image pixelation and limiting the system resolution. Typical images taken by single-mode fibre bundle is shown in Fig. 1.11 where pixelation is clearly observed.

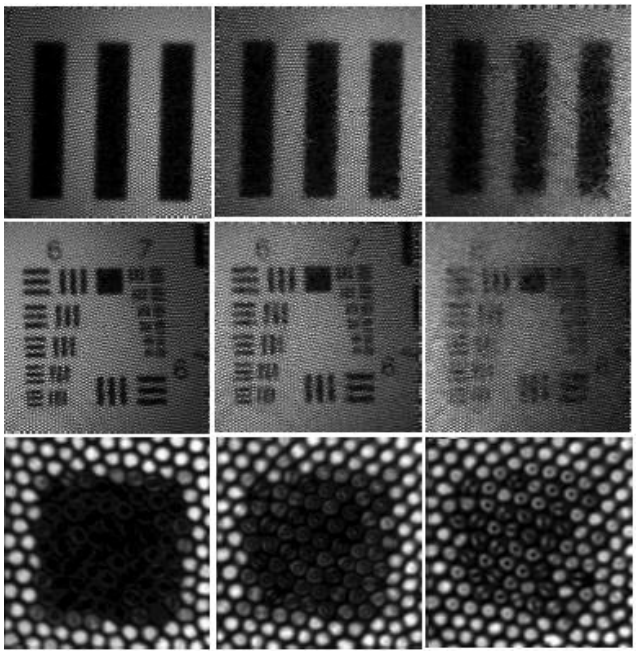

Fig. 1.11. Typical images taken by single-mode fibre bundle. Adapted from Ref[54], © 2008 OSA.

In contrast, the light propagation in multimode fibre is supported by a great number of spatial modes in a single core. These modes are working as degrees of freedom in the imaging system as those fundamental modes in the single-mode fibre bundle. Therefore if one can make the most of these spatial modes, it is possible to achieve high-resolution imaging and to reduce the cross-section further. But multimode fibres cannot deliver images directly due to two main reasons. Since each mode is travelling in the fibre with its own propagation constant, there will be mode dispersion among the spatial modes. In addition, each mode field is interacting with others when travelling, leading to possible energy exchange which is the so-called mode coupling. These two reasons result in normally observed speckle patterns shown in Fig. 1.12. Here, multimode fibre is working as a specific type of scattering medium introduced in the last section. Therefore it is reasonable to treat it as scattering media and to characterise it with previous methods, turning it into useful imaging components.

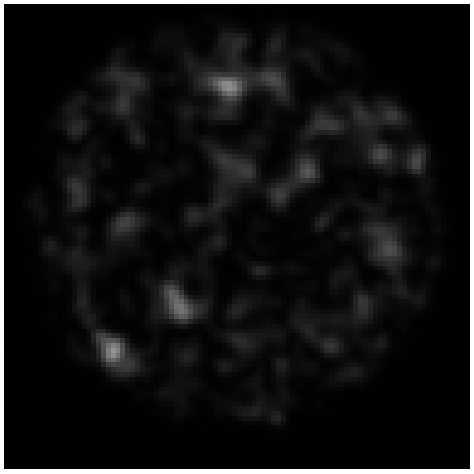

Fig. 1.12. A typical speckle pattern on fibre distal end

In 2012, Choi *et al*. realised endoscopic imaging with a single multimode fibre[55]. Working principle of their system is illustrated in Fig. 1.13. The difficulty in this setup is one has to deal with distortion in illumination step (way in) and that in imaging step (way out). In short, the multimode fibre is characterised as described in Ref[33], which can inverse the way-out distortion. Note that the object is illuminated with speckle patterns due to the distortion of illuminating light. To tackle this problem, they chose to illuminate the object with hundreds of speckle patterns by modulating the field going into the fibre with the scanning mirror. According to speckle imaging method[34], one can acquire a clean object image if averaging sufficient images taken with different speckle illuminations, which was used to address the way-in distortion.

Based on the similar setup, the same group also disclosed mode count[56] in multimode fibre by

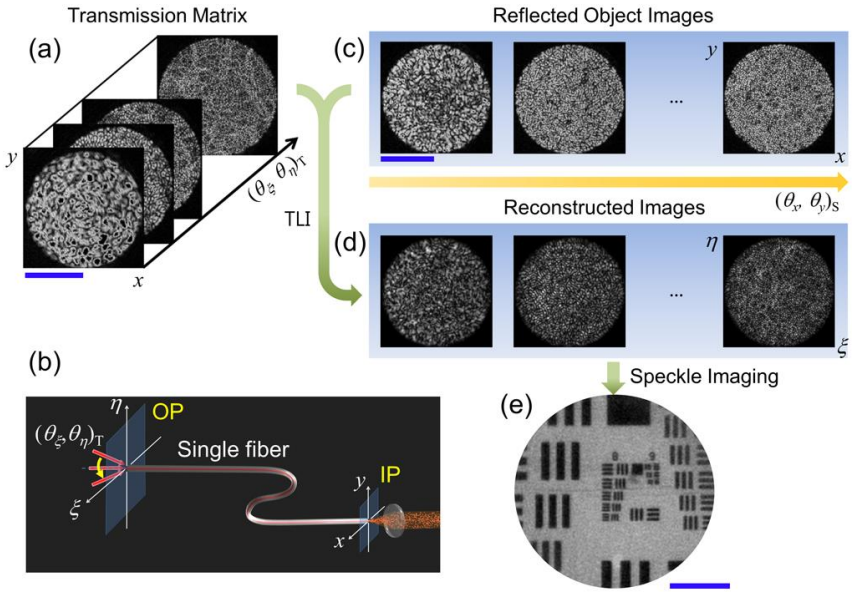

Fig. 1.13. Working flow of multimode fibre based endoscopic imaging. (a) Example images measured during calibration. (b) Calibration setup. Incident angle at OP is scanned and corresponding responses are recorded. (c) Reflected images taken at different illuminations. (d) Reconstructed results of images in (c) with measured transmission matrix. (e) Averaged image of results in (d). Scale bars: 100 μm in (a), (c) and 50 μm in (e). Adapted from Ref[55], © 2012 OSA.

studying its transmission matrix and improved fibre numeral aperture[57] by coating scattering media on fibre end, leading to better resolution. In addition, their calibration method was applied to fibre bundle as well in order to address the pixelation problem[58]. The experimental setup is shown in Fig. 1.14. The laser beam is modulated by DMD rather than scanning mirror

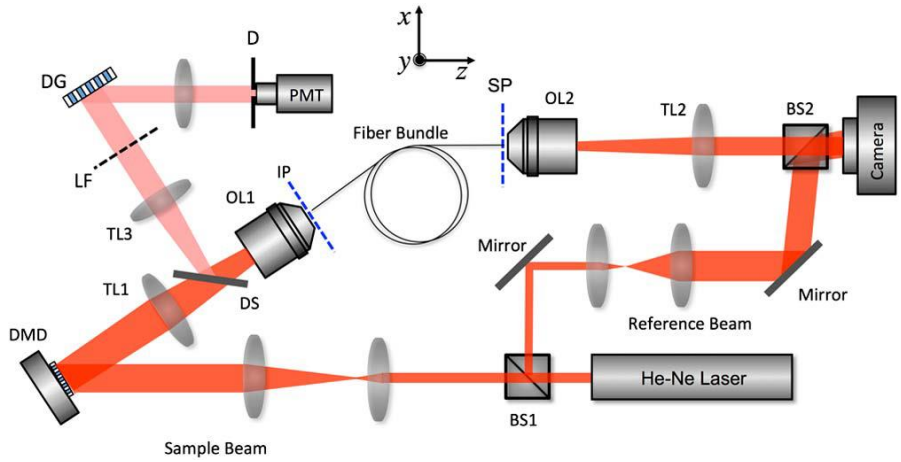

Fig. 1.14. Experimental setup for pixelation-free fibre bundle imaging. The He-Ne laser beam is separated into the sample beam and the reference beam with the beam splitter (BS1). Sample beam is modulated by the DMD and goes through the fibre bundle. Two beams are combined again with another beam splitter (BS2) to generate holograms on the camera. When imaging the sample, a clean focus is scanned across sample plane (SP) and backward light power is recorded by the photomultiplier (PMT). Adapted from Ref[58], © 2014 OSA.

here. It is straightforward to turn on one DMD pixel each time to record point spread functions. But this approach will lead to low signal to noise ratio (SNR). Therefore random amplitude patterns are used on DMD to improve SNR and corresponding output are recorded by the camera to construct the TM. In the imaging step, a clean focus is scanned across the sample by using binary phase conjugation with the information in TM. Corresponding backward light is recorded with the PMT and power information is used to construct an image of the sample.

Point-scanning based MMF imaging has also been extensively studied by other groups. In 2012, Papadopoulos *et al*. utilised digital phase conjugation to produce and to scan a focus[59]. Their experimental setup is shown in Fig. 1.15. In short, the light is focused with OBJ1 on fibre end and corresponding output field is combined with the reference beam to generate a hologram on the CMOS camera. The calculated phase conjugation field is produced by the SLM and goes through the fibre backwards to produce a clean focus on the original position on input fibre end. In order to realise point scanning, one needs to focus the laser beam on a different position on the input fibre end and to record all the output fields. Corresponding calculated phase conjugation patterns can be displayed in sequence to scan the focus across input fibre end. Based on this setup, the same group further demonstrated a point-scanning endoscope with sub-micron resolution[60].

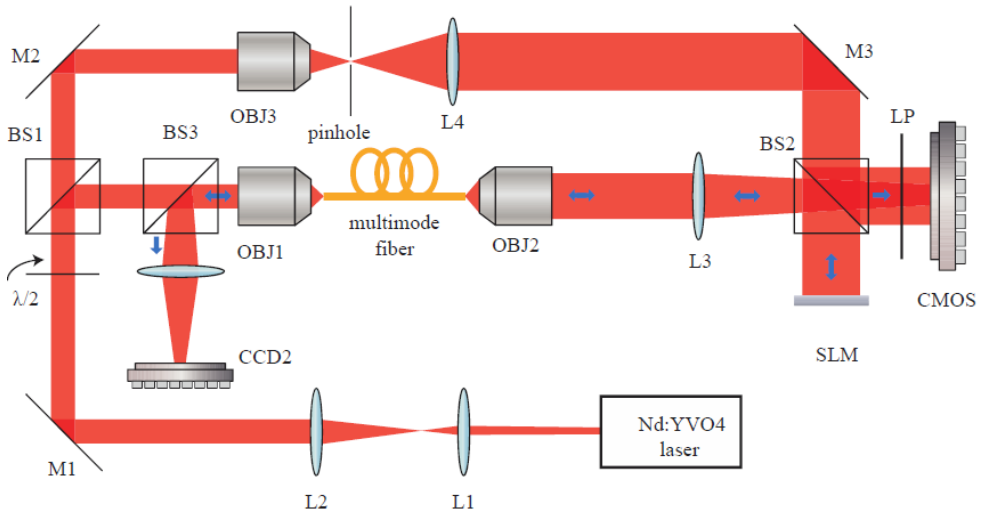

Fig. 1.15. Experimental setup of digital phase conjugation based focusing and scanning. The laser beam is split into the sample beam and the reference beam. The sample beam is focused on the fibre end and output is combined with the reference beam and is recorded to calculate phase conjugation field. Adapted from Ref[59], © 2012 OSA.

Shaping the light delivery through multimode fibres has been well studied by Cizmar *et al* to generate desired patterns on distal fibre end[61,62]. Very recently, they realised real-time (20 Hz) beam shaping by using GPU to accelerate algorithms[63]. Also, the sample group exploited multimode fibres as an endoscope to perform fluorescence imaging[64]. The experimental setup is shown in Fig. 1.16. The system calibration is the same as in Ref[62] and a scanning focus is generated on the sample plane by SLM modulations. The fluorescence emission light is guided by the sample fibre and collected by the PMT after the dichroic mirror (DM1).

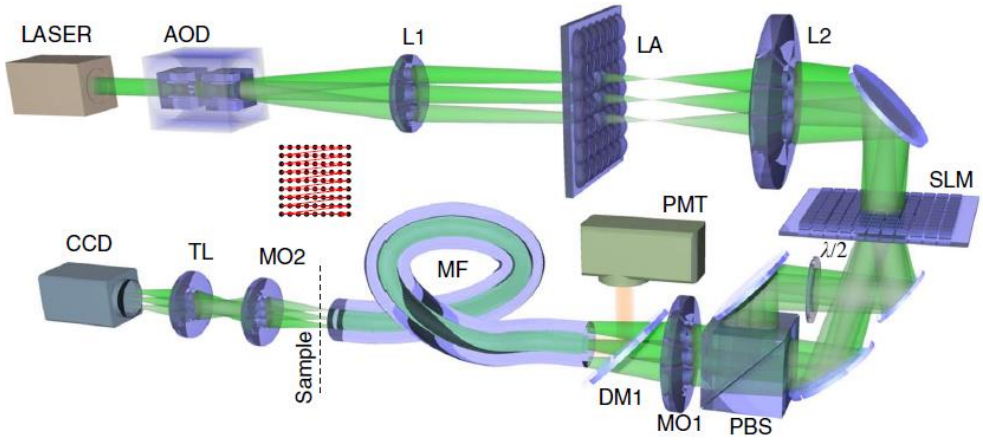

Fig. 1.16. Experimental setup for fluorescent microscopy based on multimode fibre. In the calibration step, the system is modelled to generate desired patterns as studied in Ref62. In the imaging step, the laser beam is modulated by the SLM to generate a scanning focus on the sample. The backward fluorescence signal is collected by the PMT. Adapted from Ref[64], © 2012 MPL.

Moreover, Kim *et al*. proposed a computational endoscope[65] using the incoherent source. The experimental setup and some imaging results are shown in Fig. 1.17. During calibration, the blue LED and the photomask on a translation stage work as a point source. By moving the translation stage, a set of point responses through the multimode fibre is recorded by the camera, which is used for image reconstruction. In the imaging step, a single-shot image is captured for the object. In this setup, the complex image is a linear superposition of point responses. In order to reconstruct object information, they applied the direct-binary-search algorithm[66] to minimise the error defined as:

$$\varepsilon = \sqrt{\sum_{x,y} \left| O_{image}(x,y) - I(x,y) \times P_{image}(x,y) \right|^2} \tag{1-6}$$

where $O_{image}(x, y)$ is the captured image, $I(x, y)$ defines estimated object and $P_{image}(x, y)$ is point response. The optimal $I(x, y)$ leads to minimised error and is returned as the reconstructed

image. Based on this setup, they further demonstrated a computational fluorescence microscopy[67] as well.

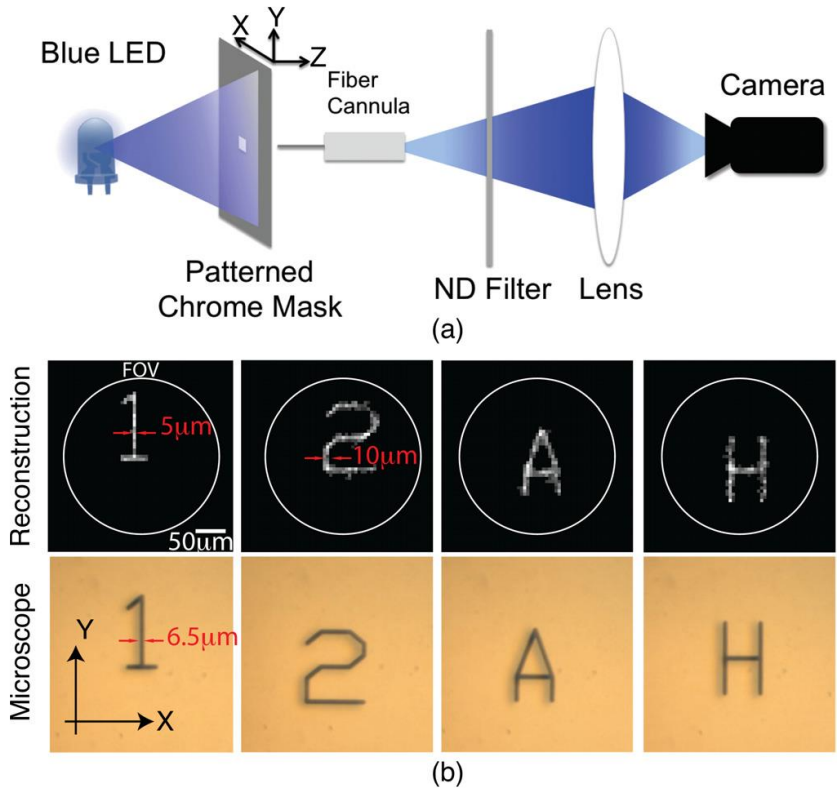

Fig. 1.17. Computational endoscope. (a) Experimental setup. (b) Reconstructed images compared to those by conventional microscopy. Adapted from Ref[65], © 2014 AIP.

Along with characterising multimode fibres, works have also been done regarding further resolution enhancement. For instance, the Moser group achieved enhanced resolution by placing scattering media in front of MMF[68] and by using saturated excitation and temporal modulation[69]. Rather than using focus scanning, Mahalati *et al*. utilised a set of random intensity patterns to sample the object and used linear optimisation to reconstruct the image, leading to 4 times resolution enhancement[70]. Moreover, Bianchi *et al*. demonstrated multimode fibre numerical aperture close to 1 by using micro-fabricated optics[71] shown in Fig. 1.18. The light leaving the outer fibre core is reflected by the parabolic surface due to total internal reflection. The spherical shape of the central part of the microstructure is centred on the focus of the parabolic surface. The NA was estimated to be 0.98, however, with the price of reduced field of view.

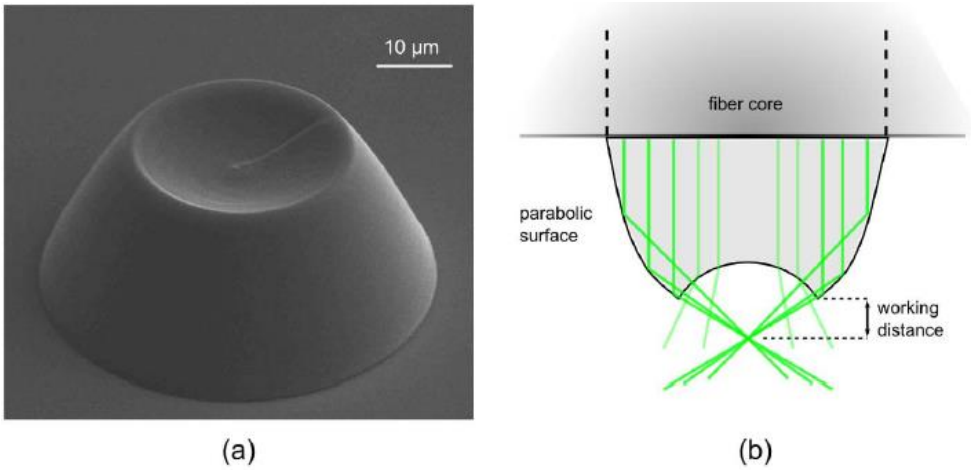

Fig. 1.18. Multimode fibre with micro-fabricated optics. (a) Scanning electron microscope (SEM) image of the micro-reflector on the fibre end. (b) Working principle of the micro-reflector in ray optics. Adapted from Ref[71], © 2013 OSA.

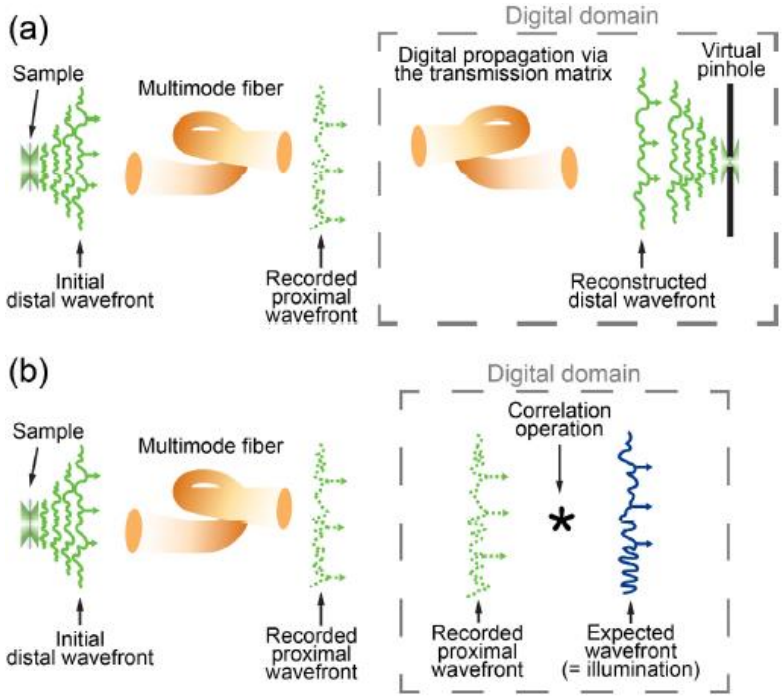

Fig. 1.19. Digital methods for contrast enhancement. (a) Digital confocal method. Backward field virtually propagates back by transmission matrix and is filtered by the digital pinhole. (b) Correlation method. The backward field is compared with excitation field to check correlation. Adapted from Ref[72], © 2015 OSA.

In order to improve image contrast, Loterie *et al*. proposed digital confocal method and correlation method[72]. In their experiments, multimode fibre is first calibrated with an SLM. In the imaging step, a clean focus is scanned across the sample and backward fields are recorded. The reference image is obtained by simply integrating total intensity of each backward field without any additional processing. The working principles of the two proposed digital filtering

methods are shown in Fig. 1.19. For the digital confocal method in Fig. 1.19 (a), the backward field virtually travels back again with the measured transmission matrix. Then, a digital pinhole is used to filter out the light beyond the radius of 1 μm of the position of excitation spot. The light energy left after such filtering is integrated to generate one pixel in the final image. In contrast, the correlation method as shown in Fig. 1.19 (b) is based on calculating the correlation between backward field and corresponding excitation field. Due to the reversibility of light propagation, the backward field should be quite similar to the excitation field if it is from the excitation focus. Therefore, the focus intensity can be estimated this way and such correlation is done for all focus positions to construct the final image.

Moreover, the same group proposed optical correlation setup[73] shown in Fig. 1.20 where backward light is modulated by the SLM again and then filtered by a pinhole. According to the reversibility of light propagation, the backward field from a focus on the distal end is ideally the phase conjugation of the modulated field to generate the focus. Therefore, it will be perfect plane wave if it is modulated by the SLM again. When concentrated by a lens and filtered by a pinhole on the lens Fourier plane, the light not from the focus will be blocked. One pixel intensity is obtained this way and the final image is achieved by scanning the focus.

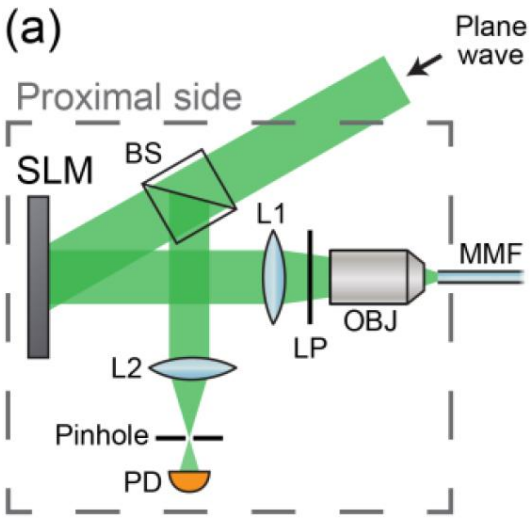

Fig. 1.20. Experimental setup for optical correlation. Backward light is modulated by the SLM again. The resulted field is filtered by a pinhole to remove the contribution, not from the focus. Adapted from Ref[73], © 2015 OSA.

Due to the characteristics of mode coupling and mode dispersion, multimode fibre is extremely sensitive to changes (e.g. geometry and temperature). It means one has to calibrate the system again if there is additional change, which is the primary obstacle on its way to commercial

imaging applications. Flexible fibre imaging has also been actively studied over the past few years. In 2013, Farahi *et al*. proposed to use virtual beacon source to realise dynamic focusing on a specific range[74]. The working principle is illustrated in Fig. 1.21. Here, the authors proposed to use double-clad fibre with photosensitive polymer coated on the distal end. The virtual beacon is produced by generating a focus on the distal end by phase conjugation technique[59]. The photosensitive polymer records corresponding field information and works as a virtual beacon. In order to realise dynamic focusing, speckle patterns on proximal end are recorded for a set of known fibre conformations. When doing dynamic focusing, the current speckle pattern is compared with stored speckle patterns to find the closest one. Corresponding phase pattern is then applied to generate a focus dynamically. The drawbacks of this approach are also obvious. Firstly, the dynamic range is up to how much data is recorded. Secondly, it is not possible to scan the focus across fibre end and not possible to do imaging. In contrast, Caravaca-Aguirre *et al*. demonstrated real-time focusing through multimode fibre[75]. The experimental system is similar to that in their work on focusing through scattering medium[39]. By exploiting FPGA and DMD, the system is able to refocus light in 37 ms and to overcome the bending issue. Besides, since full transmission matrix is obtained in real-time, it is possible to perform point-scanning imaging as well.

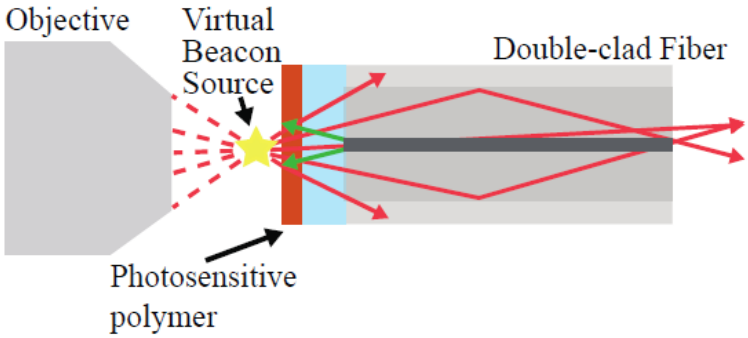

Fig. 1.21. Working principle of virtual beacon source based dynamic focusing. Photosensitive polymer works as a virtual beacon source and generates speckle patterns indicating fibre conformations. The current speckle pattern is compared with saved ones to confirm fibre geometry. Adapted from Ref[74], © 2013 OSA.

Moreover, the same group compared different fibre types and found graded-index fibre is less sensitive due to small mode dispersion[76]. Moser group also studied different fibres and found that fibres with small core diameter and larger numerical aperture are more robust[77]. These works, therefore, offer simple guidelines when choosing multimode fibres. In addition, modelling of the multimode fibre imaging has also been studied towards flexible applications.

In 2015, Gu *et al*. designed a flexible multimode fibre endoscope with a partial reflector on fibre distal end[78]. This reflected light enables measurement of mode coupling in the fibre and leads to flexible imaging. Also in 2015, Cizmar group proposed a very precise model to describe light propagation in multimode fibre and it is doable to predict transmission matrix with additional bending, leading to flexible imaging[79]. To predict transmission in multimode fibres requires accurate models especially for long fibres since errors may accumulate during the modelling process. In this work, the fibres used were no longer than 30 mm. Besides, it is necessary to exactly know the fibre geometry when modelling its transmission characteristics. Fibre bending was therefore carefully controlled in the work. This is another difficulty for real applications since fibre conformation is random.

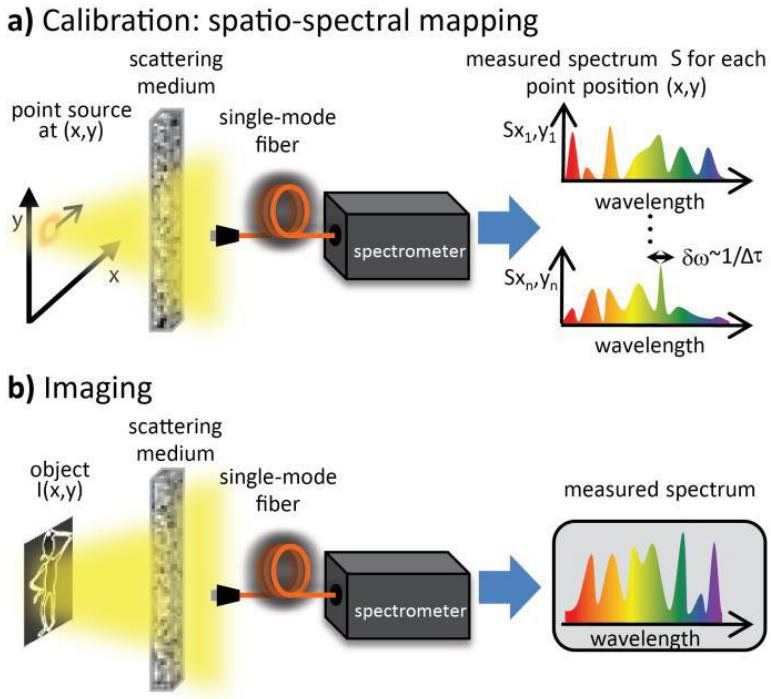

Fig. 1.22. Working principle of spatio-spectral encoding based fibre imaging. (a) Calibration: point responses are measured as a spectrum. (b) Imaging: Object is reconstructed by linear superposition of point responses. Adapted from Ref[80], © 2013 OSA.

The previous methods depend on fibre characterisation before imaging. Therefore it would be desirable if the system is calibration-free. On example is multimode fibre imaging by spatio-spectral encoding[80]. The working principle is shown in Fig. 1.22. Here, a piece of the scattering medium and a single-mode fibre work as the imaging component together. During calibration, the point responses are recorded by the spectrometer as a set of the spectrum. In the imaging step, the spectrum of the object is captured and the object information is reconstructed as the

object spectrum is the linear combination of all the recorded point responses. Since the scattering medium is fixed and the single-mode fibre is used here, the whole system is insensitive to bending. However, the resolution is not as good as previous approaches.

Another interesting method is to use Anderson localisation in disordered medium[81], allowing localised beam transport if the medium is transversely disordered and longitudinally constant. Karbasi *et al*. studied fibre design[82] in depth for this phenomenon and successfully realised image transport[83] through disordered fibres. Two types of fibres used in their experiments are shown in Fig. 1.23. This approach also suffers from low resolution. And it is proposed to enlarge material index difference and to increase air fill-fraction to enhance Anderson localisation and to improve imaging results.

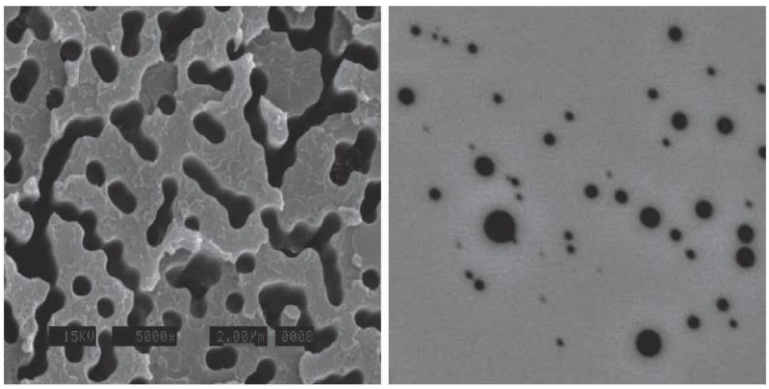

Fig. 1.23. SEMS images of two disordered fibres. (a) p-ALOF disordered fibre. (b) glass-air disordered fibre. Scale bar: 4 µm. Adapted from Ref[83], © 2014 MPL.

Memory effect has also been studied for fibre imaging as in scattering medium. However, angular memory effect is absent in multimode fibre since it is not thin and wide as a piece of the scattering medium. And rotational memory effect[84] is not strong in multimode fibre either. In order to do calibration-free imaging with memory effect, multicore fibres and fibre bundles are studied by Moser group[85] and Gigan group[86] respectively. The working principle of the latter is shown in Fig. 1.24. According to memory effect, two points close to each other on object plane will generate highly correlated but shifted speckle patterns through fibre bundle as illustrated in Fig. 1.24 (b). The shift distance is given as

$$\delta Y = \delta X \cdot V / U \tag{1-7}$$

where $\delta X / U$ denotes angular tilt of input wavefront. Therefore, there is a shift-invariant point spread function within the range where memory effect is valid. This is equivalent to the angular memory effect in the scattering medium. As demonstrated in Equation (1-4) and (1-5), the

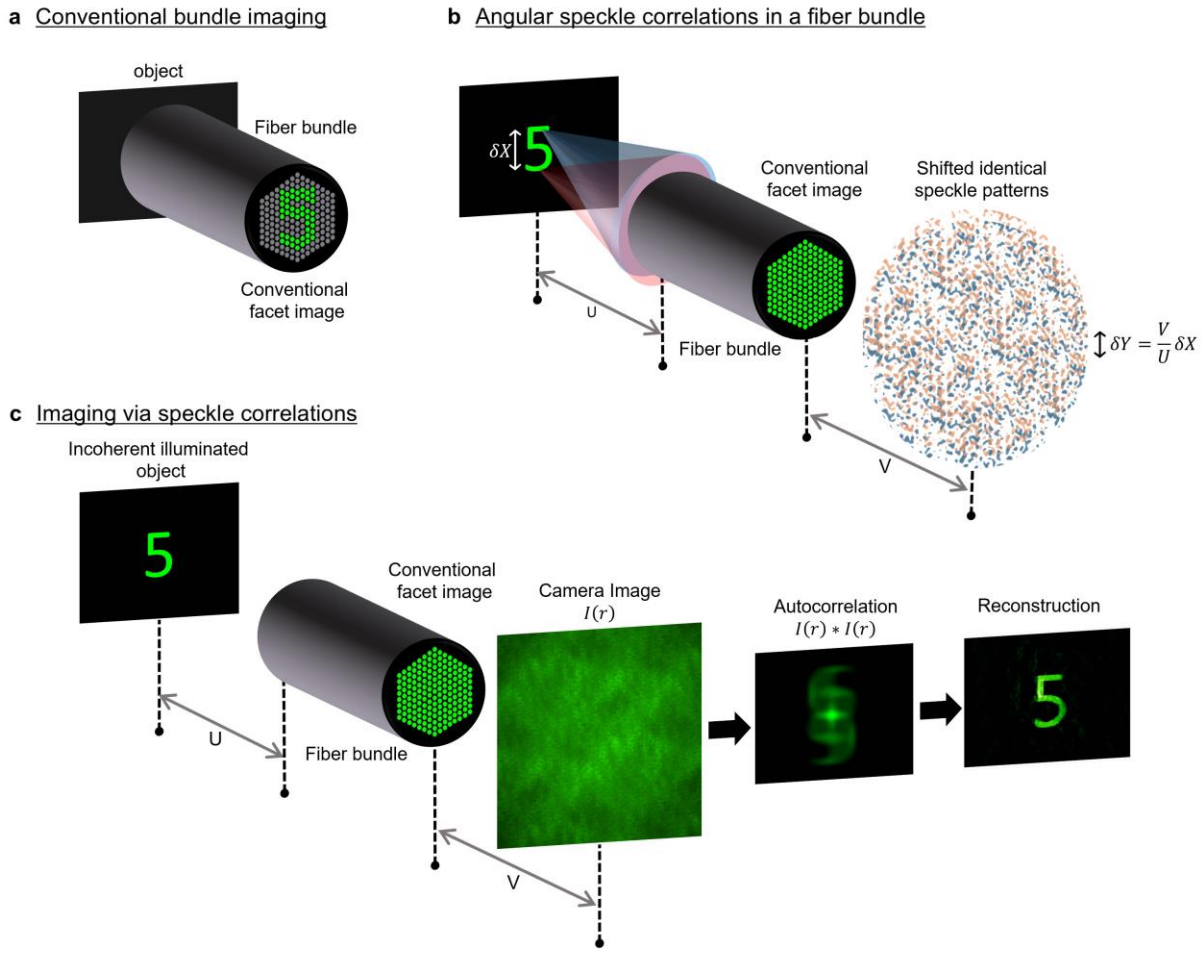

Fig. 1.24. Working principle of fibre bundle imaging. (a) Conventional fibre bundle imaging. (b) Angular memory effect in the fibre bundle. (c) Memory effect based fibre bundle imaging. Adapted from Ref[86], © 2016 OSA.

autocorrelation of the camera image is equivalent to that of the object. And it is doable to reconstruct object information by using phase recovery algorithms[50]. Since the memory effect is not up to fibre geometry, one can realise flexible imaging based on this approach. The resolution is also diffraction-limited as demonstrated in multimode fibre based methods.

1.4 Summary of the thesis

The purpose of the thesis is to develop a single multimode fibre imaging system. Multimode fibre can be a promising imaging component candidate since it is with small cross section and supports a great number of spatial modes. Basically, the work on this topic in this thesis consists of three parts: modelling of single multimode fibre imaging system (Chapter 3), reference-less characterisation of multimode fibre imaging system (Chapter 4) and analysis on transmission matrix of the multimode fibre imaging system (Chapter 5).

In Chapter 3, free space optics and fibre optics are used to construct a theoretical model for our single fibre imaging system. Without losing generosity, light coupling from free space into a multimode fibre and that of fibre spatial modes are included in the model. Fibre characterisation is simulated with our model and obtained corresponding transmission matrices. It was also demonstrated that original patterns could be well retrieved with the help of transmission matrix as it is able to undo the distortion inside multimode fibres. In addition, it is demonstrated that the multimode fibre imaging system is sensitive to environmental change such as bending since such change would change mode coupling situations. Moreover, a single-shot multimode fibre endoscope based on DMD is proposed. The critical part is to generate known illumination field on the object and to collect the backward light with the same multimode fibre. This backward field is processed with recorded TM and the effect of illumination field is removed to recover the original patterns finally.

In Chapter 4, a Bayesian inference based algorithm is developed to infer the phase information in fibre output fields. Normally, phase information is obtained by holography as the camera can only record field intensity. Since holography is extremely sensitive to environmental change, it is widely used in sensing applications but is problematic in our imaging setup. In order to address the problem of unstable conditions, output images are recorded without reference beam and processed the data with the algorithm. In this way, the transmission matrix of multimode fibre imaging system is achieved successfully without holography. In order to validate the transmission matrix, our results are tested by three criterion. Firstly, it was shown that TM-predicted output images were highly in line with actual recorded output images for arbitrary input patterns. Secondly, original patterns are retrieved with the help of the recorded TM and demonstrated that the system imaging resolution is diffraction limited. Thirdly, the information in transmission matrix is utilised to generate a clean focus on the distal fibre end and scanned the focus across it. It was shown that the enhancement factor could be 70 and it is

not uniform across the fibre end. Further improvement is expected with more precise modulation device such as SLM.

In Chapter 5, extensive data analysis on obtained transmission matrices is carried out to extract further insights from them. Firstly, it was shown that one is able to measure the number of travelling modes in multimode fibre by calculating the effective rank of its transmission matrix since spatial modes are degrees of freedom in the imaging system and rank indicates the transmission matrix's degrees of freedom. Secondly, it is disclosed that eigenchannels for a specific multimode fibre are achievable by performing singular value decomposition for its transmission matrix. The energy delivery efficiency was improved by 50% in the experiment and can be further enhanced by more accurate modulation device such as SLM. Thirdly, it was shown that the TM would experience severe change with additional fibre bending and that the phase change is much more apparent than that of amplitude, demonstrating phase change contributes more to TM deformation.

This page is left blank intentionally.

Chapter 2 Basic optical fibre theory

In this chapter, a concise overview of the basic optical fibre theory is given in order to understand light propagation in fibres and to explain why it is necessary to implement wavefront shaping technologies to image through multimode fibres. Most content of this chapter is from Ref[87,88].

2.1 Geometry optics in fibre

Optical fibres are flexible and transparent fibres produced by drawing silica or plastic to a diameter in the level of tens/hundreds of micrometres. Due to a small loss for signals travelling inside, optical fibres are used in communications widely instead of metal wires. Also, they do not suffer from electromagnetic interference, which is an obvious advantage over metal wires. Based on its transmission features and sensitivity to the environment, other applications include illumination, imaging, sensing, etc.

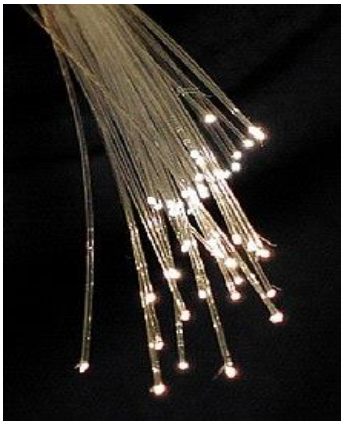

Fig. 2.1. A bundle of illuminating optical fibres, © 2017 Wikipedia.

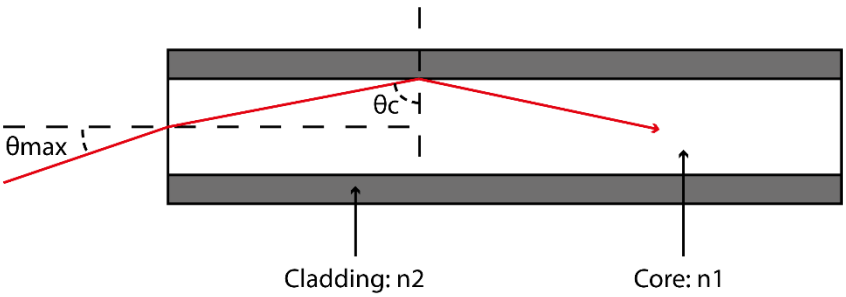

Fig. 2.2. Structure of step-index optical fibre

Normally, the optical fibre is made of the transparent core with high-index material and transparent cladding with the low-index material. From the perspective of geometry optics, the total internal reflection (TIR) confines the light in the core and gets the fibre working as a waveguide. A simple step-index fibre's structure can be described by Figure 2.2. The condition of TIR is that the incident angle on the core-cladding interface is larger than the critical angle:

$$\theta_c = \arcsin(n_2 / n_1) \tag{2-1}$$

Considering the normal case that the fibre is working in air whose refractive index is 1, with Snell's law, one can obtain the fibre numerical aperture (NA) by:

$$NA = n_{air} \sin(\theta_{\max}) = n_1 \cos(\theta_c) = \sqrt{n_1^2 - n_2^2} \tag{2-2}$$

The maximum angle of light the fibre can collect is also related to NA and the critical angle, which can be expressed as:

$$\theta_{\max} = \arcsin(\sqrt{n_1^2 - n_2^2}) \tag{2-3}$$

The incident light beyond the NA cannot be reflected totally by the core-cladding boundary and therefore cannot propagates in the fibre stably due to a significant loss. However, even if the incident angle is with NA, it does not necessarily mean the light can propagate in the core. This is due to the fact that propagation angle α (angle between the light ray and fibre axis, such as 90 - θ_c in Figure 2.2) needs to meet a phase matching condition given as:

$$\tan(k_0 n_1 a \sin\alpha - \frac{m\pi}{2}) = \sqrt{\frac{n_1^2 - n_2^2}{n_1^2}\frac{1}{\sin^2\alpha} - 1} \tag{2-4}$$

where $k_0 = 2\pi / \lambda$ is the wavenumber in the vacuum, λ denotes wavelength and a is the fibre core radius. This condition indicates that allowed propagation angles are discrete and depend on fibre parameters such as core radius, core index and cladding index. Following equation 2-4, a mode can be understood as a light ray with a permitted angle for stable propagation. The mode corresponding to $m = 0$ is the so-called fundamental mode while the others ($m > 1$) are high-order modes.

2.2 Wave optics in fibre

In the view of wave optics, a mode is an optical field distribution that is able to propagate in a particular fibre. For the sake of clarity, wave equation applied to the step-index fibre is briefly introduced and its model structure is presented here. Considering fibre geometry: circular cross-section and uniform in longitude direction, it is convenient to use cylindrical coordinates r, ϕ, z. By taking the positive z as propagation direction, the Laplacian in cylindrical coordinates is as follows:

$$\nabla^2 E = \frac{1}{r}\frac{\partial}{\partial r}(r\frac{\partial}{\partial r}E) + \frac{1}{r^2}\frac{\partial^2}{\partial \phi^2}E + \frac{\partial^2}{\partial z^2}E \tag{2-5}$$

Here, the following ansatz for the optical field is used:

$$E = E_0 NZT \tag{2-6}$$

where

$$N = N(r, \phi) \tag{2-7}$$

is the transverse field amplitude distribution and

$$Z = Z(z) = e^{-i\beta z} \tag{2-8}$$

stands for a propagation wave with wavenumber β and

$$T = T(t) = e^{i\omega t} \tag{2-9}$$

denotes a monochromatic wave whose angular frequency is ω. With cylindrical coordinates and previous ansatz, the wave equation is in the form:

$$\frac{1}{r}\frac{\partial}{\partial r}(r\frac{\partial}{\partial r}E_0NZT) + \frac{1}{r^2}\frac{\partial^2}{\partial \phi^2}E_0NZT + \frac{\partial^2}{\partial z^2}E_0NZT = \frac{n^2}{c^2}\frac{\partial^2}{\partial t^2}E_0NZT \tag{2-10}$$

By separating coordinates further, the azimuthal and the radial part of field can have independent equations respectively:

$$\frac{\partial^2}{\partial \phi^2}\Phi + m^2\Phi = 0 \tag{2-11}$$

$$r^2\frac{\partial^2}{\partial r^2}R + r\frac{\partial}{\partial r}R + r^2(k^2 - \beta^2)R = Rm^2 \tag{2-12}$$

Before arriving at wave equation solutions, three more parameters are defined:

$$u^2 = ((n_1k_0)^2 - \beta^2)r^2 \tag{2-13}$$

$$w^2 = (\beta^2 - (n_2k_0)^2)r^2 \tag{2-14}$$

$$V = \frac{2\pi a}{\lambda}\sqrt{n_1^{\,2} - n_2^{\,2}} = \frac{2\pi a}{\lambda}NA \tag{2-15}$$

where V is the normalised frequency of a particular fibre and determines how many modes are supported for propagation. Actually, the mode count in step-index fibre can be estimated well by $V^2/2$. With the help of u and w, the general solution for wave equation of step-index fibre can be given as:

$$N_1 = C_1J_m(ur/a)\cos(m\phi + \phi_0), r \le a \tag{2-16}$$

$$N_2 = C_2K_m(wr/a)\cos(m\phi + \phi_0), r > a \tag{2-17}$$

where J_m and K_m are Bessel functions. Note that the field distribution is not as ideal as explained by geometry optics: 100% energy in the core and 0% in the cladding. Since discontinuity on the core-cladding interface is not expected, the solution can be simplified as:

$$\frac{J_m(u)}{uJ_{m+1}(u)} = \frac{K_m(w)}{wK_{m+1}(w)} \tag{2-18}$$

Usually, the term of linearly polarised (LP) modes is used to describe field distribution as they have a simple form for transverse component and are linearly polarized. For LP_{lm} mode, l denotes the number of node pairs in radical coordinate while m is the possibilities in a radial direction. Note that LP_{01} is the fundamental mode and can always propagate in the optical fibre. Besides, cut-off frequency for step-index fibre is $V_c = 2.405$, which means the fibre can only support fundamental mode if $V < V_c$. In Figure 2.3, a number of patterns of low-order modes are shown for instance.

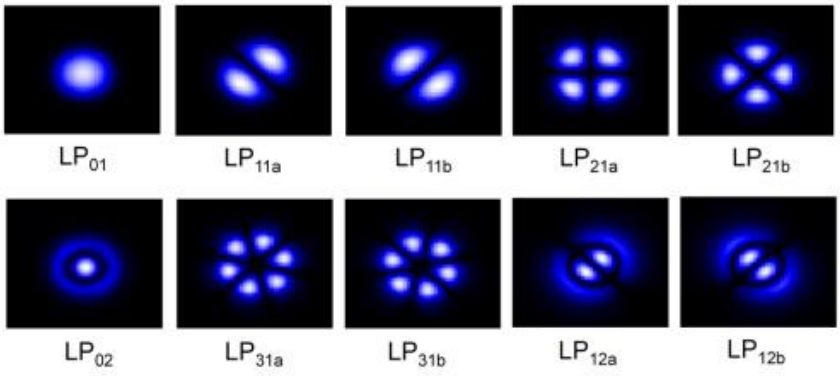

Fig. 2.3. Patterns of low-order LP modes. Adapted from Ref[89], © 2014 OSA

2.3 Wave propagation in multimode fibre

In terms of the light propagation in multimode optical fibres, it is necessary to evaluate the properties of a larger number of spatial modes that interact among themselves. Such interaction is the so-called mode coupling. In addition, different spatial modes are propagating with different propagation constants, which is known as mode dispersion. And mode coupling and mode dispersion are the fundamental reasons that multimode fibre outputs are normally 'random' speckles as shown in Fig. 2.4.

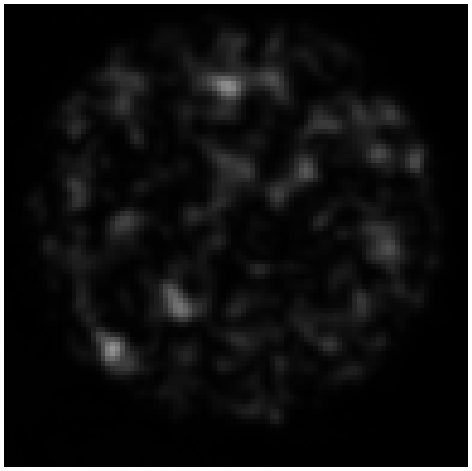

Fig. 2.4. A normal 'random' speckle pattern from multimode fibre

Mode coupling has a considerable impact on fibre transmission characteristics and is caused by certain irregularities of the fibre refractive index distribution, which are due to deviations of fibre geometry from its ideal shape. The fibre index distribution can be given as

$$n^2(r,\phi,z) = n_0^2 + n_d^2(r,\phi,z) \tag{2-19}$$

where $n_0(r)$ is the ideal refractive index distribution of the absolutely symmetric optical fibre. And $n_d(r,\phi,z)$ stands for index changes in azimuthal as well as axial directions. If the refractive index does not change too much in the distance comparable to the working wavelength of the fibre, the wave equation can be transformed into three independent equations for all Cartesian coordinates. For x-axis, it is expressed as

$$\nabla^2 E_x + n^2 k_0^2 E_x = 0 \tag{2-20}$$

where $k_0 = 2\pi/\lambda$ denotes the wave number. The Equation of (2-20) leads us to a set of LP modes which are discussed in the last section if the refractive index is only dependent on the radial coordinate. Therefore, there is no mode coupling for different modes and polarizations in optical fibres with ideal shape and index profile.

The general solution of Equation (2-20) is up to detailed index profile described in Equation (2-19), which is a combination of LP modes and is given as

$$E_x(z) = \sum\nolimits_n V_n(z) E_n(r,\phi) \tag{2-21}$$

where $E_n(r,\phi)$ is normalised the transversal distribution of the field of the *n*-th mode and $V_n(z)$ denotes complex amplitude coefficient and is expressed as

$$V_n(z) = A_n(z)e^{\pm\gamma_n z} \tag{2-22}$$

where γ_n is the complex propagation constant and is given as

$$\gamma_n = \alpha_n + j\beta_n \tag{2-23}$$

where α_n is attenuation while β_n denotes propagation constant. The negative sign in Equation (2-22) means backward propagation while the positive one stands for forwarding propagation. Also note that since different modes have different complex propagation constants, Equation (2-21) and (2-22) also imply mode dispersion during propagation process, which is another reason for the random speckle outputs.

The field $E_n(r,\phi)$ in Equation (2-21) is the solution of transversal wave equation expressed as

$$\nabla_t^2 E_n + (n_0^2 k_0^2 + \gamma_n^2)E_n = 0 \tag{2-24}$$

where *t* denotes transversal. If Equation (2-24) is multiplied by the one corresponding to E_m, the following equation is returned:

$$E_m \nabla_t^2 E_n - E_n \nabla_t^2 E_m + (\gamma_n^2 - \gamma_m^2)E_m E_n = 0 \tag{2-25}$$

If one integrates the first two terms of the fibre cross-section and applies the Green theorem, the following equation can be obtained:

$$\int_0^{2\pi}\int_0^{r}(E_m \nabla_t^2 E_n - E_n \nabla_t^2 E_m)r dr d\phi = \int_0^{2\pi}\left(E_m \frac{\partial E_n}{\partial r} - E_n \frac{\partial E_m}{\partial r}\right)r d\phi \tag{2-26}$$

Since two modes with $\gamma_n \neq \gamma_m$ are orthogonal, one can have the orthogonal condition as

$$\iint E_m E_n r dr d\phi = 0 \tag{2-27}$$

Furthermore, the following normalization condition can be applied

$$\iint E_n E_n r dr d\phi = 1 \tag{2-28}$$

The coupled differential equation of the system can be achieved with previous Equations (2-19), (2-25) and (2-28):

$$\frac{d^2 V_m}{dz^2} - \gamma_m^2 V_m = -\sum_n V_n k_0^2 \iint n_d^2(r) E_n E_m r dr d\phi \tag{2-29}$$

Here, mode coupling coefficient between *n*-th mode and *m*-th mode is defined as:

$$\chi_{nm} = \frac{k_0^2}{2\gamma_m} \iint n_d^2(r) E_n E_m r dr d\phi \tag{2-30}$$

Mode coupling process in multimode fibres can be expressed as follows

$$\frac{dA_m}{dz} = \sum_n \chi_{nm} A_n e^{(\gamma_m - \gamma_n)z} \tag{2-31}$$

Equation (2-31) indicates that the changing rate of the amplitude of one specific mode is related to all the other modes, leading to a complex coupling process and random field distributions. Since the fibres used for imaging are normally short, the loss of the light can be neglected in order to better study mode coupling phenomenon. In this scenario, the complex propagation constant is simplified as:

$$\gamma_n = j\beta_n \tag{2-32}$$

And by assuming

$$\chi_{nm} = -jc_{mn} \tag{2-33}$$

c_{mn} and β_n are then both real numbers and mode coupling Equation (2-31) is given as:

$$\frac{dA_m}{dz} = -j\sum_n c_{mn} A_n e^{j(\beta_m - \beta_n)z} \tag{2-34}$$

Fibre bending can significantly change mode coupling degree among different spatial modes. The change of fibre geometrical structure can be transformed into equivalent deviations in the index profile and can be expressed as:

$$n_d^2 = 2n_{axis}^2 \cdot x / \rho \tag{2-35}$$

where n_{axis} stands for the index at fibre central axis and ρ denotes bending radius as shown in Fig. 2.5. The normalised coupling coefficient c_{mn} in bent fibres is derived as

$$c_{mn} = \frac{k_0^2}{2\beta_m} \frac{\int\int n_d^2 E_n E_m r dr d\phi}{\left(\int\int E_m^2 r dr d\phi \int\int E_n^2 r dr d\phi\right)^{1/2}} \tag{2-36}$$

which can express coupling from the *n*-th mode to the *m*-th mode.

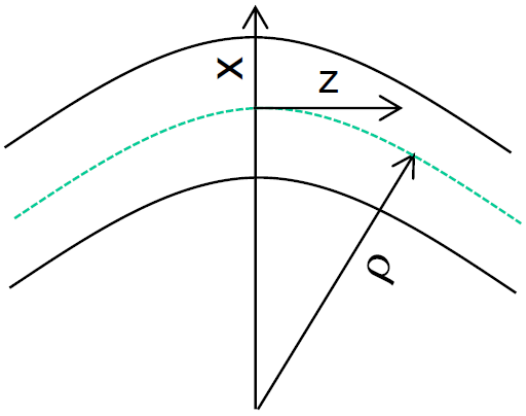

Fig. 2.5. Geometry of bent fibres. Adapted from Ref[88], © 2013 Artech House

2.4 Summary

In this chapter, the basic theory of optical fibres are introduced. As mentioned, the light propagating in the fibres can be treated as optics rays and it is easy to derive concepts like

numerical aperture by total internal reflection. Also, the light travelling inside fibres can be seen as the sum of optical fields of supported spatial modes. Different modes are propagating with diverse speed since they have different propagation constants, which is defined as mode dispersion. Furthermore, different modes are exchanging energy when travelling, which is known as mode coupling. When arriving at the fibre end, different mode fields are summed up to generate normal speckle patterns due to amplitude and phase differences at various positions of the fibre end. It is also shown that mode coupling is highly related to fibre geometry, which is limiting the system flexibility and indicating the need of recalibration when additional fibre bending is introduced.

As a theoretical chapter, the content here explains normal observations and the difficulty in multimode fibre imaging and serves our work in fibre imaging system modelling presented in chapter 3 where knowledge of optical fibres are used to confirm mode count, mode propagation constants, mode distributions, mode dispersion/coupling in order to construct a full theoretical model for the system.

This page is left blank intentionally.

Chapter 3 Modelling of single multimode fibre imaging system

Following the previous theory introduction, a theoretical model for the single multimode fibre imaging system is constructed in this chapter with the equations introduced before. Basically, our model is built from fibre optics and Fourier optics and includes critical processes such as mode coupling and mode dispersion. The effectiveness of the model is validated by TM based image retrieval and its parameters' influence is studied as well. Moreover, it is further demonstrated that a single-shot multimode fibre imaging system can be achieved by using controlled illumination fields.

3.1 Introduction

The use of a tiny probe for image transmission has attracted much attention owing to its great potential in in-vivo endoscopy. To achieve this, a conventional approach is to reduce the size of the imaging fibre bundle (i.e. by reducing the number of individual fibres contained in the bundle). This, unavoidably, results in low-resolution images since each core contributes as one pixel in the image. Another approach is to use the so-called scanning single fibre probe where a single mode fibre is installed with a piezo-actuator at the distal end. The optical fibre tip can, therefore, be scanned across the area of interest in order to produce an image[90]. The use of mechanical actuators, however, cannot effectively reduce the imaging probe cross-section. Recently, a study demonstrated that images can be reconstructed after travelling through a single multimode fibre (MMF), leading to a scanner-free and wide-field single MMF imaging system[55]. Such MMF based imaging approaches are advantageous over existing fibre bundles or scanning single fibre probes, including ultra-high resolution limited by diffraction and the ultra-thin diameter of hundreds of microns.

There have been considerable experimental investigations on the single MMF imaging system in recent years. In Ref[91], special sampling patterns were used to enhance the image resolution and to reduce noise. In order to overcome the image distortion due to fibre bending, a coherent beacon source was proposed to be placed at the distal end of MMF to obtain bending information by comparing the current speckle pattern with the pre-saved ones[74]. In addition, digital phase conjugation was utilised to undo the distortion from model scrambling and to generate a clean focus through multimode fibre[59], resulting in high-resolution and lensless endoscopes[60]. The same group further added scattering medium in front of the fibre end to achieve higher numerical aperture, leading to higher resolution and longer working distance[68]. In Ref[72], a single MMF confocal microscope was demonstrated where collected signals were filtered with a virtual digital pinhole to obtain high contrast images. Apart from MMF based confocal microscope, a scanning-free computational microscope[65] was proposed to perform 3D fibre imaging. Here, calibration was carried out by applying point sources at different locations. The single-frame image was then captured and used to reconstruct object information with a nonlinear optimisation algorithm. In a recent theoretical work, a design of flexible fibre imaging system was presented. Here, the MMF coupling was modelled by Haar-distributed random unitary without considering the transmission and coupling of individual modes. Very recently, it was demonstrated experimentally in Ref[79] that even significant bent fibres can be predictable since it is possible to calculate fibre transmission matrix if the fibre geometry is completely known. Flexible fibre imaging has therefore been demonstrated for fibres with a certain length. The remaining problem is that the model has to be very precise to express the light propagation in the MMF. And the error is accumulated when increasing fibre length. In this work, the fibre used was no longer than 30 cm. Besides, the fibre shape was carefully controlled in their experiment since the shape information is critical to modelling, which would be problematic in real applications as one has to measure the random shape.

The number of guided modes in an MMF usually exceeds thousands, determined by factors such as fibre diameter, fibre index and working wavelength. These spatial modes will inevitably couple with each other during the transmission, leading to distorted images when delivering through MMFs. In such image transmission system, every single pixel on the object will have a distinctive point spread function (PSF) according to the spatial mode coupling. In order to reconstruct the object information from the scrambled output, one needs to find the relationship between inputs and outputs of the imaging system[92,93]. Normally, transmission matrix is used to represent the PSFs from the input plane to the output plane[24,26] and to perform

image reconstruction. Therefore, it is necessary to develop MMF imaging models to understand and predict imaging process, thereby designing appropriate experimental approaches to address existing challenges such as limited flexibility and to enhance system robustness and efficiency.

In this chapter, a theoretical model is developed to describe the single MMF imaging system involving diffraction and propagation of optical fields in free space as well as MMF. Our focus is on building a mathematical model and to explore the influence of the MMF on the imaging transmission. The model is based on analysing the propagation of each mode and is verified by conducting simulations for illumination and image reconstruction. Therefore, our model is capable of expressing specific mode coupling conditions in the MMF and of providing insightful guidelines for imaging system design. The chapter is organised as follows: firstly, the complex field transmission in the optical system involving a multimode fibre is expressed, using free-space diffraction theory and fibre model coupling theory. Secondly, we demonstrated numerically the idea of image recovery with the help of transmission matrix recorded in calibration. Thirdly, we studied the impact of system parameters on imaging quality, such as fibre core diameter, image size and bending radius. Lastly, we proposed a single-shot multimode fibre imaging system by using knowledge of *TM* to precisely control the illumination field and to retrieve object information.

3.2 Theoretical model

In this study, the optical system is simplified as a combination of object plane, multimode fibre and imaging plane. Here, it is assumed that the modulated field by DMD or SLM propagates to object plane without distortion and that the field on imaging plane travels to the camera without distortion. In practice, the possible slight distortion is considered in transmission matrix as one has only access to modulation patterns on DMD/SLM and images captured by the camera. Since the transmission matrix is actually for the system from modulation device to camera, the slight distortion by objective and lens etc. is well covered. Our simplified imaging system is shown in Fig. 3.1 where OP is object plane, MMF denotes the multimode fibre and IP stands for imaging plane. Normally, one may assume there is no distance between object plane and proximal fibre end since light is supposed to be focused on the fibre end. In experiments, distance tuning is achieved by maximising the fibre output power while slowly moving the fibre end. It is observed in experiments that the fibre output power is maximum in

a certain range of distances. Therefore, without losing generalisation, it is assumed that object plane and proximal fibre end are separated slightly (d1). The same assumption applies to distal fibre end and imaging plane (d2).

Fig. 3.1. A simplified model of the multimode fibre imaging system.

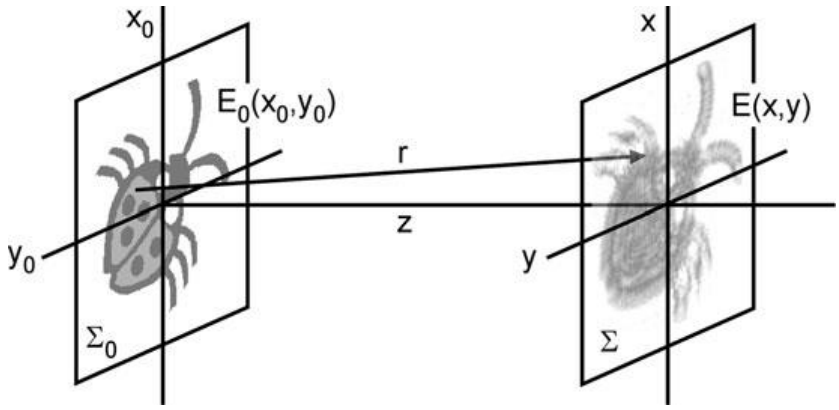

Fig. 3.2. Diffraction of an insect pattern. Adapted from Ref[94], © 2011 Springer

The light field will also experience change when travelling in free space and such transformation can be expressed by scalar diffraction theory. The diffraction of a 2D pattern shown in Fig. 3.2 as an example. According to the Huygens-Fresnel principle, we have:

$$E(x,y;z)=\frac{z}{j\lambda}\iint E_0(x_0,y_0)\frac{e^{jkr}}{r^2}dx_0dy_0 \tag{3-1}$$

$$r=\sqrt{(x-x_0)^2+(y-y_0)^2+z^2} \tag{3-2}$$

where r is the distance between one point one on start plane and another on end plane. Fresnel approximation is the Huygens-Fresnel principle in a more simple form:

$$E(x,y;z)=\frac{\exp(jkz)}{j\lambda z}\iint E_0(x_0,y_0)\exp\left\{\frac{jk}{2z}\left[(x-x_0)^2+(y-y_0)^2\right]\right\}dx_0dy_0 \tag{3-3}$$

In our model, however, Equation (3-1) is used to avert further approximation on *r*. The diffraction theory is then used to calculate field propagation from object plane to proximal fibre end and that from distal fibre end to the imaging plane.

Once the field on fibre proximal end is obtained, it is time to calculate the light coupling into the fibre. As introduced in Chapter 2, light propagation in multimode fibre is supported by a certain number of spatial modes with specific field distributions. Here, the following equation is used to express such coupling and to get initial mode coefficients:

$$A_i = \iint E_{in} \cdot E_i^* dxdy \tag{3-4}$$

where A_i is the initial coefficient of the *i*-th fibre mode, E_{in} denotes input field on proximal fibre end, E_i is for normalised field distribution of the *i*-th fibre mode and * stands for conjugation. Note that E_{in} and E_i need to be polarised in the same direction. Otherwise, there would be no energy transferring from E_{in} into E_i.

After calculation with Equation (3-4), one can initialise the fibre modes and turn to mode coupling and dispersion during light propagation in MMF. As introduced in Chapter 2, the light field in multimode fibre can be expressed as the sum of fields of individual modes:

$$E(z) = \sum_n V_n(z) E_n(r, \phi) \tag{3-5}$$

Here, $E_n(r, \phi)$ is the normalised transverse field distribution of *n*-th linearly polarised mode and $V_n(z)$ denotes its complex amplitude. Also, it is assumed linearly polarised laser is used in the system and corresponding linearly polarised modes are excited in the multimode fibre. During the light propagation, fibre modes interact with each other and each mode complex amplitude $V_n(z)$ is changing owing to mode coupling and mode dispersion. The light field on fibre distal end is again the sum of all the mode fields and is normally presented as a speckle pattern due to mode coupling and mode dispersion. Specifically, Equation (2-2) and (2-3) are used to calculate the numerical aperture and maximum collection angle of the fibre. And Equation (2-5) to (2-17) are used to obtain simplified wave equation (2-18) which is solved in order to confirm mode count and fibre mode propagation constants. Fibre normalised frequency can be calculated by Equation (2-15) and standard LP mode distributions are used in the

following calculations. In order to consider the mode coupling and mode dispersion process, Equation (2-19) to (2-33) are used to obtain propagation equation (2-34) which is describing how fibre modes are interacting inside the fibre when travelling. Also, the coupling coefficient is highly related to fibre geometry according to Equation (2-35) and (2-36). In this way, fibre bending degree is connected with fibre coupling coefficients and it is straightforward to study the impact of fibre geometry on fibre transmission characteristics afterwards. With the equations introduced previously, the light field on fibre distal end after complex mode coupling and mode dispersion can be successfully calculated.

With the light field on fibre distal end, one can apply Equation (3-1) again to calculate the light field on the imaging plane. Therefore a full model can be constructed to describe the light propagation from object plane to imaging plane. Since the whole process is linear, it is possible to describe the field transformation by a matrix, which is the so-called transmission matrix (*TM*). By considering input and output fields as vectors, one can have:

$$E_{output} = TM \cdot E_{input} \tag{3-6}$$

According to Equation (3-6) and linear algebra, it is easy to have:

$$[E_{output\_1}, E_{output\_2}, E_{output\_3}, ..., E_{output\_n}] = TM \cdot [E_{input\_1}, E_{input\_2}, E_{input\_3}, ..., E_{input\_n}] \tag{3-7}$$

If naming matrix $[E_{output\_1}, E_{output\_2}, E_{output\_3}, ..., E_{output\_n}]$ as M_{output} and name matrix $[E_{input\_1}, E_{input\_2}, E_{input\_3}, ..., E_{input\_n}]$ as M_{input}, the following equation is obtained:

$$M_{output} = TM \cdot M_{input} \tag{3-8}$$

Therefore *TM* can be obtained by

$$M_{output} \cdot M_{input}^{-1} = TM \tag{3-9}$$

where M_{input}^{-1} means the inverse of M_{input}. Equation (3-9) indicates the general method to do the system calibration. Note that in order to calculate *TM* successfully, the columns of M_{input} (input patterns in calibration) are chosen to be linearly independent. This can be easily achieved

by using point sources in simulations. For the experiment, binary random input patterns can be pre-generated and are selected to be linearly independent. Besides, it is normal that the count of measurements in calibration is equal to the pixel count in input patterns. Therefore M_{input} can be guaranteed to be invertible. One needs to modulate a set of input fields and couple them into MMF imaging system. Corresponding output fields need to be recorded and transmission matrix can be calculated by Equation (3-9). Note that the input fields are supposed to be linear independent but not necessarily to be in any special forms. In Ref[55,72], plane waves were chosen as input fields while point sources were used as input basis in Ref[79]. Actually, random input fields are sufficient to construct the *TM* as demonstrated in Ref[58]. Also, if the image size is not equal to the count of scanning, the matrix M_{input} is not a square matrix and therefore has no strict inverse. In this case, the pseudoinverse can be used to calculate the *TM*. And Equation (3-10) is transformed to

$$M_{output} \cdot M_{input}^{+} = TM \tag{3-10}$$

where M_{input}^{+} stands for the pseudoinverse of M_{input}. The pseudoinverse of a matrix is a generalisation of the inverse matrix. In mathematics, a generalised inverse (GI) of element x is an element y which has some features of a strict inverse element but not necessarily all of them. Generalised inverses can be defined in any mathematical structure that involves associative multiplication, that is, in a semigroup. Formally, given a matrix A and a matrix A^{g}, A^{g} can be a generalised inverse of A if it meets the following equation:

$$AA^{g}A = A \tag{3-11}$$

The purpose of making a generalised inverse of a matrix is to achieve a matrix that is able to serve in some sense for a wider class of matrices than invertible matrices. A generalised inverse exists for an arbitrary matrix. And this generalised inverse is its unique generalised inverse when a matrix has a regular inverse.

The motivation of constructing generalised inverse is from solving linear equation problems. Considering the following linear system:

$$Ax = y \tag{3-12}$$

where A is an $m \times n$ matrix. If A is invertible, therefore the solution of the system is

$$x = A^{-1}y \tag{3-13}$$

Suppose A is singular or $m \neq n$ which is more general. Then it is necessary to have a right candidate G of order $n \times m$ such that

$$AGy = y \tag{3-14}$$

This indicates that Gy is a solution of linear system by Equation (3-12). Therefore, what in need is a matrix G of order $n \times m$ such that

$$AGA = A \tag{3-15}$$

which is line with Equation (3-11). According to Equation (3-12) to Equation (3-15), the generalised inverse or g-inverse is defined as follows: given a matrix A and a matrix G, G is a generalised inverse of A if they meet the Equation (3-15).

The most widely known type of generalised inverse of a matrix is pseudoinverse. Unlike inverse, it exists for all the matrix and it is equal to inverse if A is invertible. Therefore Equation (3-10) contributes as a general way to calculate TM no matter M_{input} is invertible or not. The pseudoinverse A^+ exists for any matrix A and A^+ satisfies the following four criteria:

$$AA^+A = A \tag{3-16}$$

$$A^+AA^+ = A^+ \tag{3-17}$$

$$(A^+A)^* = A^+A \tag{3-18}$$

$$(AA^+)^* = AA^+ \tag{3-19}$$

Note that if A^+ only satisfies Equation (3-16), it is a generalised inverse. If it meets Equation (3-16) and Equation (3-17), it is called a reflexive generalised inverse. When A is invertible, any generalised inverse equals to the inverse of A and is unique:

$$A^g = A^{-1} \tag{3-20}$$

But in other scenarios, there is infinite matrices meeting Equation (3-16). In contrast, pseudoinverse is always unique however A is.

Another type of generalised inverse is one-sided inverse including right inverse and left inverse. The right inverse is defined as follows: if the matrix A is in order of $m \times n$ and rank of A is m, then there is an $n \times m$ matrix A_R^{-1} called the right inverse of A such that

$$AA_R^{-1} = I_m \tag{3-21}$$

where I_m is an $m \times m$ identity matrix. Similarly, left inverse is defined as follows: if the matrix A is in order of $m \times n$ and rank of A is n, then there is an $n \times n$ matrix A_L^{-1} called the left inverse of A such that

$$AA_L^{-1} = I_n \tag{3-22}$$

where I_n is an $n \times n$ identity matrix.

Note that A^+ is equal to A^{-1} when A is invertible. In addition, when A has full rank, A^+ can be calculated simply. Specifically, if A has linearly independent columns, matrix A^*A is invertible and A^+ can be given as:

$$A^+ = (A^*A)^{-1}A^* \tag{3-23}$$

In this case, A^*A is also a left inverse of A since $A^+A = I$. And when A has linearly independent rows, matrix, matrix AA^* is invertible and A^+ can be given as:

$$A^+ = A^*(AA^*)^{-1} \tag{3-24}$$

In this case, A^+ is also a right inverse of A since $AA^+ = I$. In contrast, a general and accurate method to calculate the pseudoinverse is by utilising the singular value decomposition. If the singular value decomposition of A is expressed as

$$A = USV^* \tag{3-25}$$

Then the pseudoinverse of A is calculated by

$$A^+ = VSU^* \tag{3-26}$$

Note that in order to construct the *TM* effectively, it is suggested to have scanning count around image pixel number. When scanning count is not sufficient, the construction of *TM* will not be accurate. Considering the extreme case, if both M_{output} and M_{input} have only one column, one

can still construct a *TM* based on Equation (3-10). However, this *TM* would not work since too much information on transmission characteristics is missing. Besides, it is not necessary to take too many measurements since it would slow down the whole calibration process. Also, note that the *TM* only works to connect input fields and output fields rather than intensity images captured directly by the camera. Therefore holography, no matter in off-axis or in-line form, is normally used in MMF imaging systems to obtain the full information of output fields.

3.3 Imaging in transmission mode

According to Equation (3-6), the output field of a point source would be one column of the TM. This approach can be easily implemented in modelling process and one can also avert matrix inverse calculation in Equation (3-6). Also, since the light fields are modelled directly,

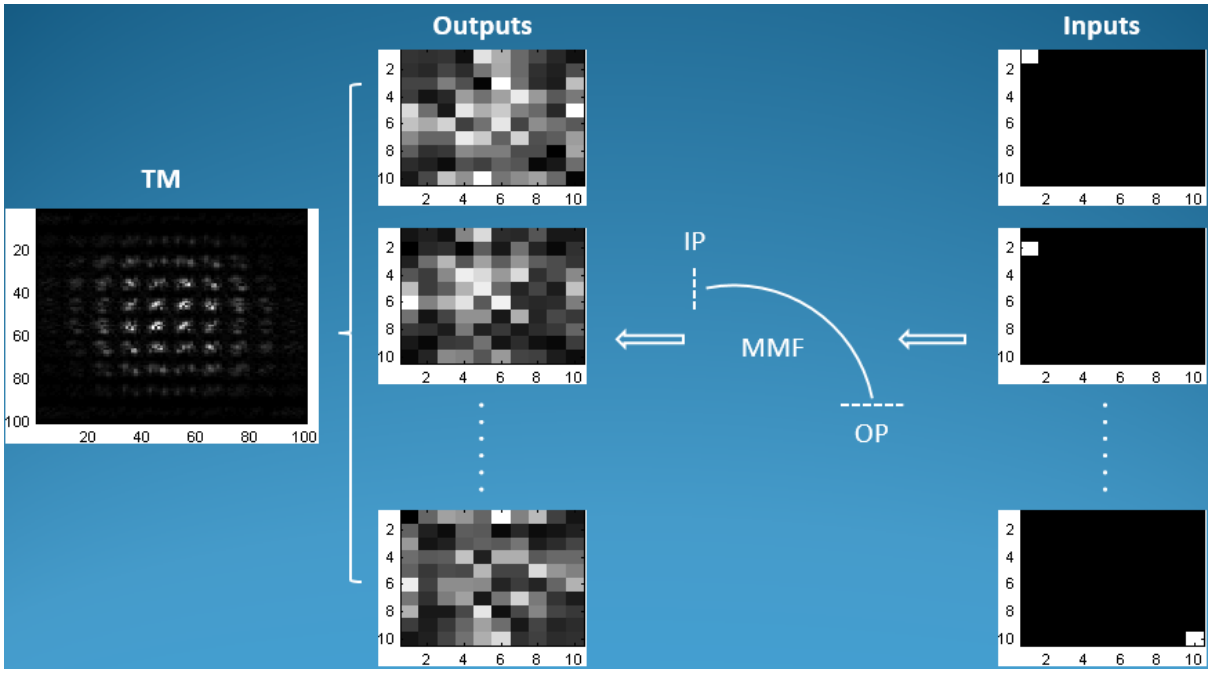

Fig. 3.3. TM recording process in the model.

the holography issue is not considered here. A 100-mm multimode fibre with a uniform bending radius of 500 mm is studied firstly here. The core index and cladding index are 1.45 and 1.44 respectively and core radius is 10 um. In order to acquire the TM, a point source is scanned across the object plane and corresponding outputs on imaging plane is recorded as shown in Fig. 3.3. As a proof-of-concept study, both inputs and outputs consist of 100 pixels. In this case, a scanning over 100 point sources is sufficient to confirm the transmission

characteristics of the imaging system. Note that the outputs are complex fields and only amplitude is shown here. As mentioned before, a column in the TM is one output in calibration if using point sources. Therefore it is convenient to construct the TM by reshaping each output into a column and by combining these columns in order as a matrix. To examine our calculated TM, a test pattern of 'EE' was working as the object and its transmission image was simulated by the model. According to Equation (3-5), it is easy to have:

$$E_{input} = TM^{-1} \cdot E_{output} \tag{3-27}$$

Therefore, with the help of TM^{-1}, one can undo the distortion during the propagation and actually see through the MMF. The reconstruction process is shown in Fig. 3.4. Clearly, the image on the fibre distal end looks very 'random' although the object information is well preserved. The TM/TM^{-1} is working as a key to unveiling object information behind MMF distortion. In addition to Equation (3-9), it is also possible to obtain object information by solving linear equations as stated in Equation (3-5). Although not as straightforward as Equation (3-9), it is a faster and more accurate implementation in MATLAB.

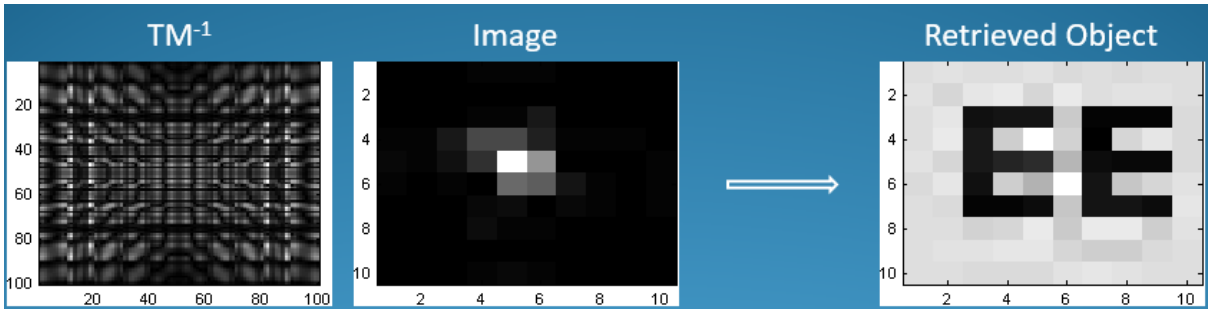

Fig. 3.4. Object reconstruction in the model.

So far, it has been numerically demonstrated the image reconstruction by the TM. It is reasonable that the system imaging ability is up to the MMF parameters. Here, the impact of mode count on imaging quality was studied firstly. In order to evaluate imaging quality, it is straightforward to calculate the correlation coefficient of the retrieved object and original object. Since conventional correlation coefficient is for real numbers, it is defined for complex fields as:

$$cc = \frac{\left|\sum_m \sum_n (A_{mn} - \bar{A})(B_{mn} - \bar{B})^*\right|}{\sqrt{\left(\sum_m \sum_n \left|(A_{mn} - \bar{A})\right|^2\right)\left(\sum_m \sum_n \left|(B_{mn} - \bar{B})\right|^2\right)}} \tag{3-28}$$

where A and B are 2-dimensional full fields. In Fig. 3.5, MMFs supporting different numbers of modes are studied and compared their imaging quality by the correlation coefficient. The object used here is a same 16×16 pattern and one can see the apparent increase in correlation

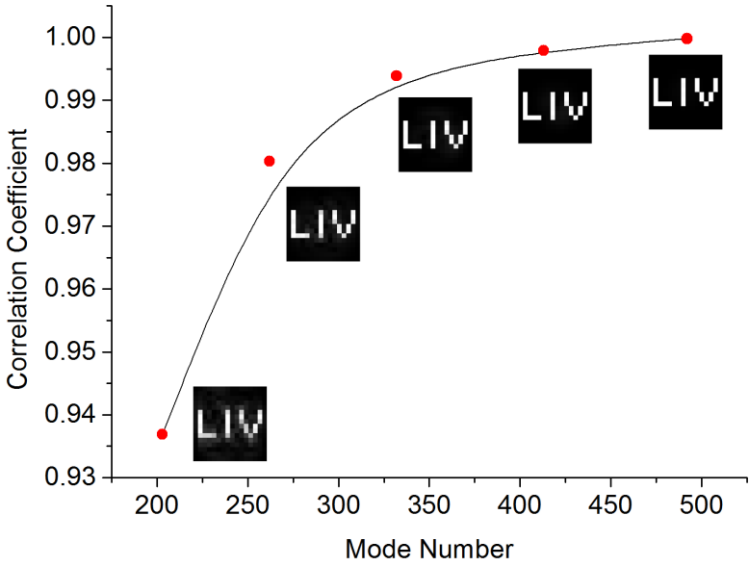

Fig. 3.5. The relationship between correlation coefficient and mode number.

coefficient when there are not many spatial modes supported in the MMF. The turning point is around 256 modes and the increasing of the correlation coefficient is quite limited afterwards. In order to understand the change in Fig. 3.5, one can take each spatial mode in the MMF as a degree of freedom of the imaging system. In the extreme case, one can do imaging with single-mode fibre and still do the calibration for multi-pixel inputs and outputs. However, since there is only one mode travelling in the fibre, the values in output pixels are completely related. Therefore, it is not possible to express the multi-pixel change in the input patterns. With the increase of degrees of freedom, i.e. the number of spatial modes, the expression ability of the system is stronger. And it is necessary to have N degrees of freedom to retrieve information of an N-pixel object. This is why the turning point is around 256 which is the image pixel number in this case. With even more spatial modes, one can observe further quality improvement but very limited. This is implying that it is necessary to consider which multimode fibre to use

depending on the size of the image. For commercial multimode fibres, one can easily have tens of thousands of spatial modes which should be enough to generate with high-resolution images.

In addition to the requirement on mode count, the flexibility of the MMF imaging system is also investigated. In order to do this, different multimode fibres are calibrated without any bending and images with various bending radius are acquired. Here, the step-index multimode fibre with core diameter being 40 or 44 μm, core and cladding index being 1.45 and 1.44 respectively, is used. One can know that they can support 413 and 492 spatial modes respectively by solving eigenfunction. And the fibre length is 10 cm. The objects are

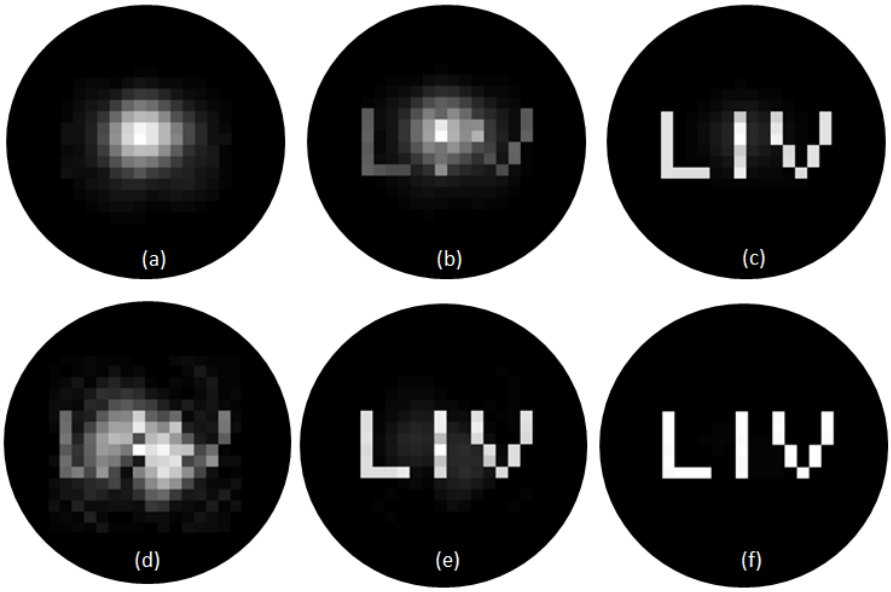

Fig. 3.6. Retrieved objects through bent fibres using the TMs of corresponding straight fibres. (a) mode count = 413, bending radius = 1 m; (b) mode count = 413, bending radius = 10 m; (c) mode count = 413, bending radius = 100 m; (d) mode count = 492, bending radius = 1 m; (e) mode count = 492, bending radius = 10 m; (f) mode count = 492, bending radius = 100 m.

reconstructed with the original TM and the results are presented and compared in Fig. 3.6. As shown, with the changing of bending radius, the quality of the reconstructed objects is decreasing obviously. And imaging results are worst with the severest bending. Since the mode coupling process is highly up to fibre geometry as expressed in Equation (2-35) and (2-36), the transmission characteristics of a multimode fibre depend on fibre deformation. Therefore, one cannot retrieve object information effectively with the original TM from an image captured after fibre deformation. As the imaging system is calibrated with straight fibres, it is reasonable that one cannot see through severely bent fibres. Note that the imaging system has the flexibility to some degree, which is various for different types of multimode fibres. It is also clear that the image quality degradation is improved for fibres supporting more spatial modes.

It is believed that the system change is shared by all the modes and the mode complex amplitude change will be smaller with more mode travelling in the fibre. Since the optical field on fibre distal end is the sum of all the mode fields, it is more flexible with more spatial modes supported inside, which is also a guidance when flexibility of imaging system is in need. In addition to mode coupling, mode dispersion is another reason for output speckle patterns. Since graded-index fibre has much smaller mode dispersion, it is supposed to be more robust to additional deformation. This idea has been demonstrated experimentally in Ref[76].

In addition, the noise effect and thresholding are also considered in the imaging model. Specifically, Gaussian noise is implemented on the supposed object (i.e. 'LIV' pattern). The MMF used here is still the one supporting 492 spatial modes as in Fig. 3.6 (core diameter: 44 μm, core index: 1.45, cladding index: 1.44). As shown in Figs. 3.7 (a-f), it is found the expectation (EXP) of the normal distribution of the noise does not matter much since the original pattern can be well retrieved by thresholding (threshold=0.5) in all three cases. This attributes to the fact that noise is contributing as bias because its standard deviation is small. Therefore, original patterns can be recovered if the threshold is appropriate. In contrast, the impact of noise standard deviation (STD) is more obvious as presented in Figs. 3.7 (g-l). Firstly, it is clear that direct recovery results get worse when noise standard deviation is increasing. Since noise is more diverse, it is harder to tell the pattern from the background. Secondly, the thresholding results are also worse with the increase of noise standard deviation. Although thresholding still generates binary results in these cases, the count of wrongly classified pixels is increasing. This is because thresholding is no longer able to completely differentiate pattern pixels from background pixels due to diverse noise.

Another concern of the theoretical work here is the calculation speed. The current code is written in MATLAB and it would take roughly one hour to calculate the output image of one specific input pattern. In order to finish the whole calibration more quickly, parallel jobs are normally running on computation nodes, leading to calibration time of 5 hours roughly. This also depends on how much calculation resource is available on high-performance computation nodes. Normally, it is practical to acquire around 50 cores. To further improve the model performance, it is suggested to rewrite the code in C++ or other low-level languages since they are running much faster in general.

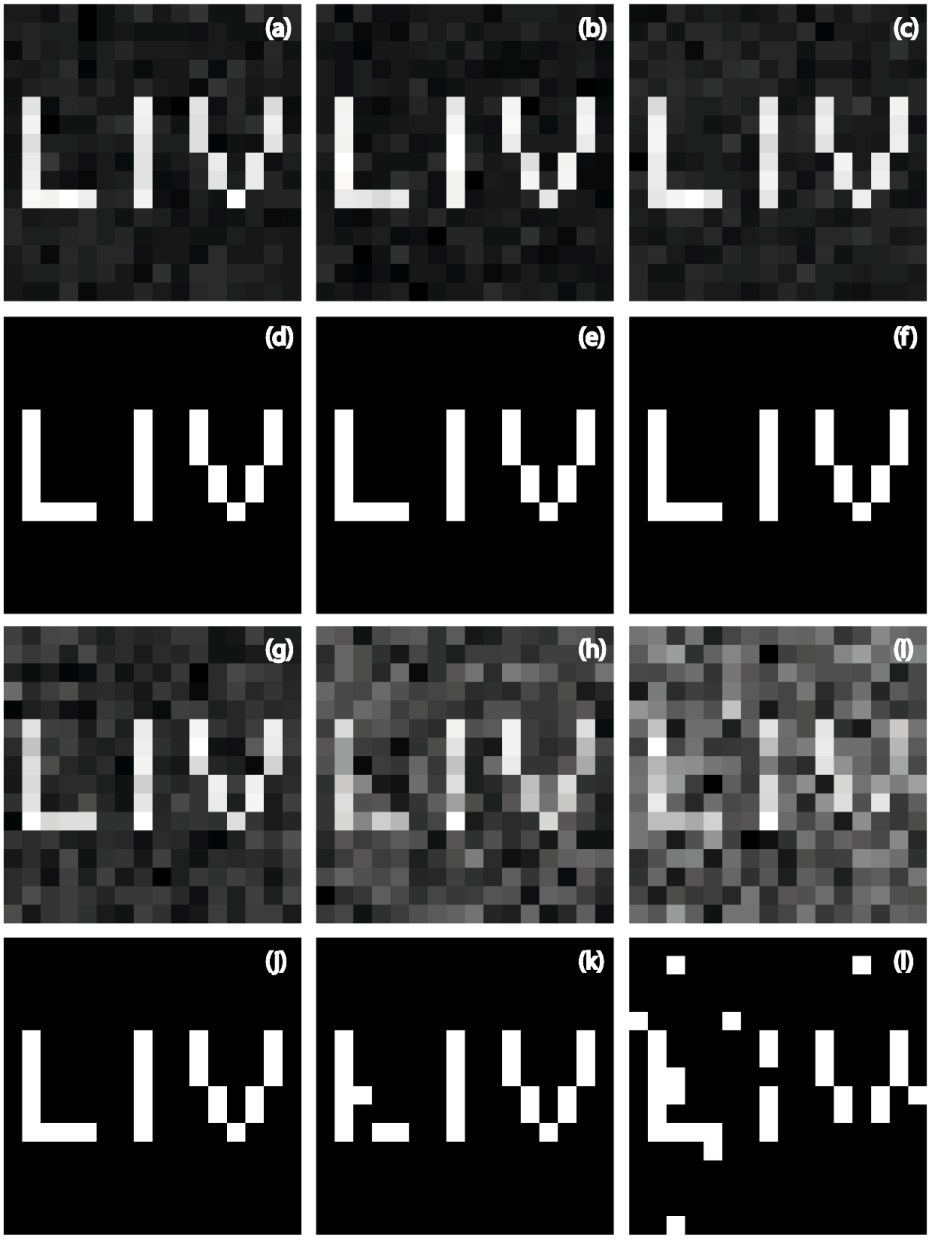

Fig. 3.7. Retrieved objects with object noise and thresholding (a) noise EXP = 0.1, noise STD = 0.05; (b) noise EXP = 0.2, noise STD = 0.05; (c) noise EXP = 0.3, noise STD = 0.05; (d) thresholding result of (a); (e) thresholding result of (b); (f) thresholding result of (c); (g) noise EXP = 0, noise STD = 0.1; (h) noise EXP = 0, noise STD = 0.2; (i) noise EXP = 0, noise STD = 0.3; (j) thresholding result of (g); (k) thresholding result of (h); (l) thresholding result of (i);

3.4 Single-shot multimode fibre based endoscope

Previously demonstrated endoscopes working in reflection mode necessitate a certain form of scanning (e.g. plane wave, sharp spot and random pattern). In this section, however, a single-

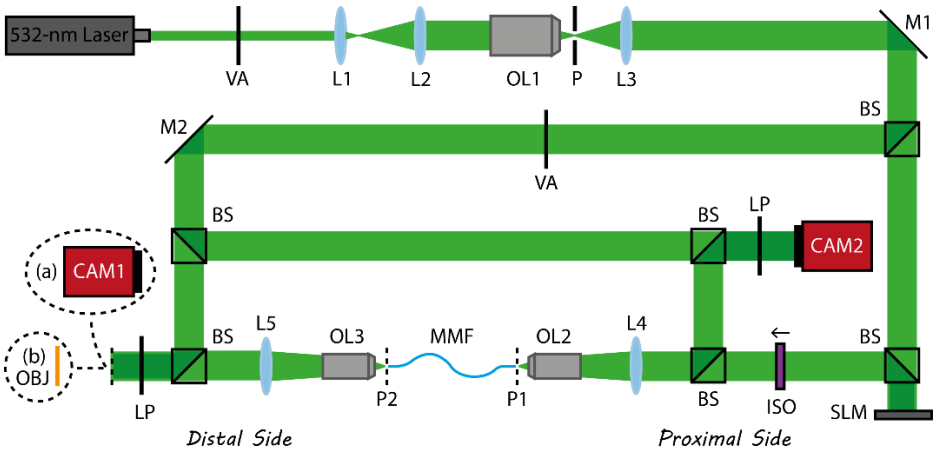

Fig. 3.8. Proposed single-shot endoscopic setup for (a) calibration and (b) imaging.

shot single-MMF endoscope is demonstrated based on theoretical modelling. With the obtained TM, a controlled illumination field (e.g., uniform illumination) can be generated through the imaging MMF, thereby eliminating the need for scanning at the proximal end. The captured single image is then recovered by TM method and this allows the direct acquisition of the original object in one go. This leads to a truly scanning-free and single-shot single-optical-fibre endoscope. The proposed endoscopic setup is shown in Fig. 3.8. Here, the fibre side with a spatial light modulator (SLM) is defined as the proximal side while the other side is called the distal side. During the calibration step, wavefronts consisting of a basis generated by SLM propagate through the MMF and the corresponding holograms are recorded on Camera 1. The TM is then calculated based on the inputs and outputs. During the imaging stage, a single input field is sent to the MMF. The backward light reflected by the Objective is guided by the same MMF and generates a hologram on Camera 2 after interfering with the reference beam. Our theoretical model is built for light propagation between P1 and P2 with Fourier optics (free space propagation) and fibre optics (mode coupling and mode dispersion), assuming fields on P1 and P2 are well recovered by corresponding off-axis holography. In this proof-of-concept study, in order to reduce the calculation time, 256-pixel images are processed and MMFs supporting no more than 500 modes are used. In our calculation, the MMF core and cladding indices are 1.45 and 1.44 respectively, and the pixel size is set as 2μm, which is close to the fibre diffraction limit.

Highly controlled illumination is critical for the single-shot imaging process, depending on recovery ability of TM. It is accepted that the number of spatial modes is of great importance to the recovery accuracy, as it represents the degrees of freedom in the imaging system. In Fig. 3.4, recovery results of a “LIV” pattern with 10-cm straight fibres (in transmission mode)

supporting different numbers of modes are presented. It is evident that a larger count of modes leads to cleaner images. The turning point where mode number (262) is close to pixel number (256) marks that information in all the pixels can be recovered well, resulting in correlation coefficients (CC) over 0.98.

In principle, arbitrary illumination field can be utilized to perform the proposed single-shot imaging. In terms of experiments, however, one may prefer to control input wavefront to generate uniform illumination or to input simple plane waves. In Fig. 3.9, single-frame imaging is demonstrated for a 10-cm 492-mode bent MMF (bending radius 1 m) with uniform illumination as well as even input for a pattern of "QM". Calculated required input field (only

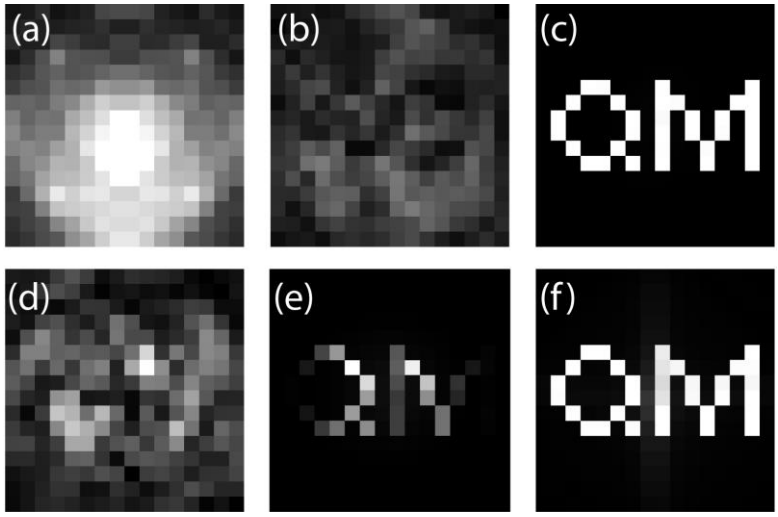

Fig. 3.9. Single-shot imaging process. (a) Input pattern to generate uniform illumination on object; (b) Backward image corresponding to (a); (c) Retrieved object corresponding to (b); (d) Illumination field on object from a uniform input pattern; (e) Initial retrieved object corresponding to backward image (not shown here); (f) Final retrieved object without impact from illumination corresponding to (d).

amplitude here) to generate uniform illumination is shown in Fig. 3.9 (a) while obtained backwards image and recovery results are presented in Fig. 3.9 (b) and Fig. 3.9 (c) respectively. Since target illumination field is uniform, it is not necessary to filter out illumination impact afterwards and final CC is over 99.98%. In contrast, uniform input leads to the image in Fig. 3.9 (d) and initial recovery result in Fig. 3.9 (e) which is severely deviated from original pattern (CC of 7.63%) as uneven illumination results in amplitude and phase differences. A clean image (CC of 99.27%) obtained after illumination impact filtering is shown in Fig. 3.9 (f). Such filtering can be easily achieved using element-wise right division in MATLAB.

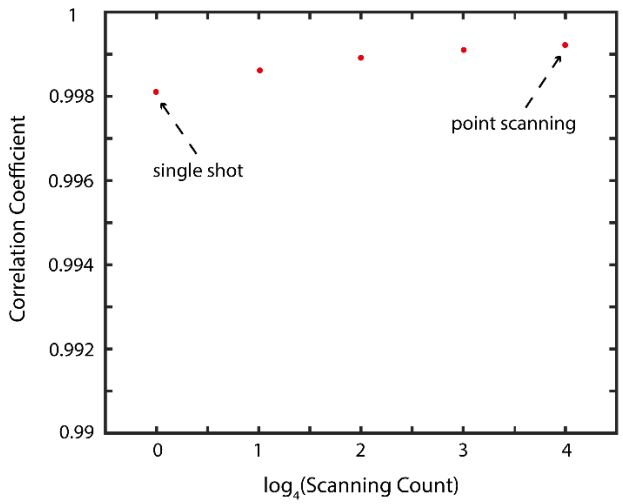

Fig. 3.10. Retrieval quality comparison between single-shot method and scanning approaches

So far, the working principle of our single-shot imaging system has been demonstrated. In addition, it is necessary to compare it with popular scanning approaches. In a general point of view, one can scan the bright illumination field across the object to perform imaging. If the bright illumination field has only one pixel, it is the so-called point scanning method. If the bright illuminated field covers the whole object, it is the single-shot approach here. In addition, one can also carry out imaging in the middle. For instance, bright zones of different size can be generated through MMF and scanned over the whole object. For each case, the final image is the combination of recovery results of all the possible illumination conditions. Corresponding results are shown in Fig. 3.10. Here, the count of scanning is increased by splitting each previous illumination square zone into four equal but smaller square zones. Therefore the scanning count is increasing exponentially and the exponentiation base is 4. The largest scanning count is 256 corresponding to the point-scanning method and the smallest scanning times is 1 corresponding to the single-shot approach. It is shown that larger scanning numbers lead to slightly better recovery results and one can hardly tell the quality difference. The single-shot method could offer CC over 99.98% and does not require a time-consuming scanning process. Considering typical SLM operation speed of 30 Hz, image capture time is considerable for high-resolution (e.g., 512×512) images. But it is believed scanning approach could reduce random system noises better and therefore offer a certain degree of improvements in experiments. Additionally, the illumination field in the model is processed as the combination of pixels, which is different from the real case. Such deviations may lead to imaging result differences. Also, the modulation ability of the modulation device is of great importance in this setup as one needs to generate highly controlled output patterns through the

multimode fibre. Given this fact, one may prefer SLM over DMD since phase modulation is continuous and more efficient. Another approach is to use DMD as SLM with the help of additional lenses and computed holograms. In this theoretical work, it is assumed necessary input field can be perfectly modulated and delivered into multimode fibres. Although MMF imaging could offer some flexibility, it is favourable to be used as a rigid endoscope. The small diameter (around 200 um) of the MMF matches that of the thinnest needle gauges, and therefore the MMF can be embedded into practical applications.

3.5 Summary

In this chapter, a theoretical model for single multimode fibre imaging system is constructed based on fibre optics as well as Fourier optics. Specifically, the light propagation in free space is described with diffraction to generalize the model since there may be space between object/image plane and fibre end. In addition, mode theory is used to deal with light travelling inside fibre. By solving wave equation, mode count and mode propagation constants can be calculated and light field in fibre core can be expressed as the sum of fields of all the supported spatial modes. Also, it is shown that multimode fibre would normally scramble the original information and lead to speckle outputs due to complex processes including mode coupling and mode dispersion. The former is highly related to fibre geometry since fibre bending would impact mode energy change degree (i.e. coupling coefficient). This also explains why the multimode fibre imaging system is not flexible and offers a way to study the bending impact on fibre transmission characteristics.

Besides, the idea of TM based image retrieval was demonstrated with our model. And it is shown that original object information can be well retrieved if TM is available after calibration. The influence of system parameters was also studied. It is demonstrated necessary to have fibre mode count around original image pixel count to recover the information effectively because fibre mode count stands for the degree of freedom in the imaging system. It is also shown that multimode fibres supporting more spatial modes are more flexible as additional bending impact are shared among all the modes. Finally, a single-shot multimode fibre imaging system by illuminating objects with highly controlled fields was proposed and demonstrated. This system utilises knowledge of TM to generate engineered illumination fields and to retrieve object information. The TM is used more sufficiently and the setup, therefore, enables faster image

acquisition. The recovery result is also demonstrated comparable with that obtained by conventional point scanning approach.

This page is left blank intentionally.

Chapter 4 Reference-free characterisation and bending analysis of single multimode fibre imaging system

As investigated in the last chapter, a theoretical model was developed to express the light propagation in the multimode fibre. It was clearly shown that the transmission characteristics of a specific MMF can be described by a so-called transmission matrix since the fibre is a linear system and that the transmission matrix can be used to undo the information distortion due to mode coupling and mode dispersion, leading to imaging through the chaos. However, to construct the transmission matrix necessitates calibration of the system and extraction of phase information in the fibre output fields. Normally, phase acquisition is achieved by off-axis or phase-shifted holography. But both of them require very stable system since interference is extremely sensitive to environmental perturbations, e.g. deformation and temperature.

In this chapter, experimental approaches have been demonstrated to characterise a single multimode fibre imaging system without a reference beam, leading to a simplified and robust system. Spatial light modulation is performed with a digital micromirror device which enables high-speed binary amplitude modulation. Intensity-only images are recorded by the camera and processed by a Bayesian inference based algorithm to retrieve the phase information of output optical field and to infer the transmission matrix of the fibre. The calculated transmission matrix is validated by three standards: prediction accuracy, transmission imaging, and focus generation. Also, it is demonstrated experimentally that fibre transmission characteristics are highly related to fibre geometry and that bending sensitivity can be suppressed effectively with strong initial coupling.

4.1 Introduction

Recently, multimode fibre (MMF) has been shown to be a promising candidate for endoscopic imaging due to a great number of spatial modes travelling within a cross-section down to tens of micrometres[95]. Typically, wave propagation in MMFs suffers from mode coupling and mode dispersion and generates complex speckle patterns, which is a fundamental problem for imaging applications. Although fibre mode dispersion and coupling scramble the transmitted image information and lead to 'random' output patterns, the light propagation process inside can actually be modelled. With appropriate characterization, MMFs can also work as conventional imaging components like lenses.

Over the past few years, wavefront shaping technology has been investigated extensively to characterize MMFs so that a single MMF can be used to transmit images. Light propagation in the linear medium is a linear process and can, therefore, be described by its transmission matrix (TM)[24,26], which is calculated from a set of system's input-output pairs. In Ref[55], Choi *et al.* used a scanning mirror to modulate the input fields and obtained the output fields with off-axis holography. All the data was processed to construct the TM, leading to imaging with diffraction-limited resolution. However, this method necessitates recording of input fields as well, which is time-consuming and lowers experiment operability. Alternatively, by offering phase-only modulations, liquid crystal-based spatial light modulators (LC-SLM) are more widely used in wavefront shaping. Using an LC-SLM, Papadopoulos *et al*. demonstrated focus generation[59] and point scanning based fluorescence imaging[60] with digital phase conjugation. Also, Loterie and co-workers utilized an SLM to measure the TM of the MMF and further achieved high imaging with digital confocal[72] and optical confocal setup[73]. The importance of monitoring system stability and phase drift is stressed in the works since phase correction is essential for TM effectiveness. In addition, digital mirror device (DMD) has been used as a cheap and high-speed alternative to SLM. The rotation of micro-mirrors on board can realize binary amplitude modulation, which can also be used to measure fibre TM and to perform point-scanning imaging[58]. The previously mentioned approaches all require a reference beam, either co-propagating in fibre or in an external form. However, extracting the full information on the optical field by phase-shifted or off-axis holography comes at the cost of a complicated setup and suffers from instability issues arising from the holographic interference process for phase retrieval.

Since the mode coupling is highly up to the fibre geometry, MMF sensitivity to perturbations is a long-lasting obstacle for real applications. To tackle this problem, A. M. Caravaca-Aguirre *et al*. demonstrated a real-time re-focusing system based on feedback and wavefront control[75]. However, it is hard to implement *in vivo* since it requires the access to fibre distal end. Besides, Farahi *et al*. proposed a dynamic bending compensation system with the help of another single mode fibre and a virtual beacon source[74]. But the possible change of MMF is carefully limited in this setup and enough data should be pre-measured to perform the following re-focusing. Moreover, recent developments in theoretical models enable the prediction of fibre output after deformation[79]. To match the experimental results with theoretical ones, the model has to be extremely accurate. Since the errors are accumulated with increasing distance, this method is only valid with short fibres (no more than 300 mm). Another related difficulty is that the geometry of the fibre should be completely known to model the propagation, which is hard for real applications as the fibre will be randomly shaped. With the angular memory effect in the fibre bundle, Porat and co-workers proposed a bend-insensitive, single-shot imaging system based on speckle correlation and without wavefront shaping[86]. However, this interesting scheme is not suitable for MMF since angular memory effect is not obvious in MMF. In terms of the type of MMF, it has been demonstrated that graded-index MMF[76] and high-NA MMF[77] suffer less from fibre deformations.

In this chapter, the acquisition of complete transmission matrix of MMF using DMD and without a reference beam has been demonstrated. It involves an advanced phase retrieval algorithm[96] and therefore leads to a simplified and robust optical setup. A sufficiently large number of output fields can be measured quickly thanks to the high speed of DMD. The algorithm itself runs in a parallel format such that distributed computations can be used to accelerate the data acquisition. The calculated TM is verified with three criteria. Firstly, predicted outputs for random inputs are compared with corresponding actual outputs for prediction accuracy estimation. Secondly, imaging in the transmission mode is demonstrated with pre-defined patterns and resolution is studied. Lastly, a set of focuses is generated on the distal fibre end with the information in TM as a focus-scanning process. Besides, the geometry sensitivity of the MMF in our system is investigated and it is found that flexibility can be effectively improved with strong initial coupling.

4.2 Experimental setup

The diagram of our experimental setup is shown in Fig. 4.1. A DMD with 1024×768 micro-mirrors (Discovery 1100, Texas Instruments) driven by an interface board (ALP-1, ViALUX) was used to modulate the 632.8-nm laser beam (25-LHP-925-230, Melles Griot), which was direction-adjusted by two mirrors (M1 and M2) and expanded by two lenses (L1 and L2). The DMD modulated light field was coupled into the 50-μm-core MMF (1.5-m long and bent into a circle of diameter ~200-mm, FG050UGA, Thorlabs) with a tube lens TL1 (AC254-200-A-ML, Thorlabs) and a microscope objective OL1 (Nikon CFI Plan Achro 40X, 0.65 NA, 0.56 mm WD, tube lens focal length: 200 mm). Corresponding MMF outputs, magnified by another microscope objective OL2 (Olympus 20X Plan Achro, 0.4 NA, 1.2 mm WD, tube lens focal length: 180 mm) and the tube lens TL2 (AC254-100-A-ML, Thorlabs), were passed through a polarizer (LPVISE100-A, Thorlabs) and recorded by the camera (C1140-22CU, Hamamatsu). In our setup, we set 2×2 micromirrors as a single macro pixel in the modulation to enhance the difference between the "ON" and the "OFF" pixels. We also used input patterns consisting of N = 1296 macro pixels and captured output patterns with M = 9216 pixels on the camera. The number N is limited by the maximum number of modes supported in the MMF, as sufficient degrees of freedom are required to describe the change of input patterns. Also, if there are too many macro pixels, the beam diffracted by the DMD will be too wide to be collected and

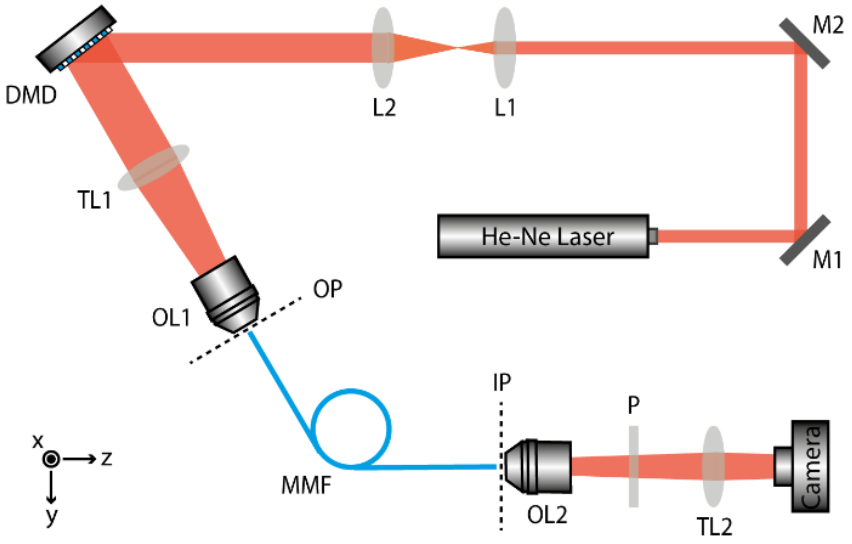

Fig. 4.1. Schematic experimental setup of reference-less MMF characterization. He-Ne Laser: 25-LHP-925-230, Melles Griot; M1, M2: Mirrors; L1, L2: Bi-Convex Lenses; DMD: Digital Mirror Device, Discovery 1100, Texas Instruments; TL1: Tube Lens, AC254-200-A-ML; TL2: Tube Lens, AC254-100-A-ML; OL1: 40X Objective Lens, Nikon; OL2: 20X Objective Lens, Olympus; MMF: Multimode Fiber, FG050UGA, Thorlabs; P: Polarizer, LPVISE100-A, Thorlabs; Camera: C1140-22CU, Hamamatsu; OP: Object Plane; IP: Image Plane.

resized by the tube and objective lenses. The size of the fibre core and magnification of the objective lens constrains the input pattern size and in addition, the computation time will increase with the size of the input and output patterns. The number M is determined by the parameters of the MMF used in our experiment particularly the core diameter and by the magnification of the objective lens. In order to retrieve phase information successfully using this algorithm, $M/N \geq 2$ is needed.

In calibration, the system is fed with around $P = 8000$ input fields which are random binary patterns whose pixels were either turned on or off with equal probability. In the most straightforward way, one can light up one macro pixel each time and record the generated output (if with phase), which is actually a point spread function of the system and one column of its TM. However, calibration is not carried out this way since it was found that the light diffracted by only one pixel is very weak, resulting in a poor signal to noise ratio (SNR). With turning around half of the pixels on, the response of a single macro pixel is actually measured $P/2$ times, which means the SNR is improved $\sqrt{P/2}$ times compared to the simple approach of turning on each macropixel in order. Moreover, the DMD pattern displaying was operated at 250 Hz, which is limited by our camera as the DMD speed can be up to 8 kHz. However, the speed of the USB cable that connects the DMD to the computer for data loading is the main limiting factor of the speed if the modulation data is more than the DMD on-board memory. In our case, due to the on-board memory limitation with the current DMD, it is only possible to display 20 images successively. Therefore most of the calibration time is used in loading data into DMD memory. In total, calibration will take around 25 minutes. The camera will be the limiting factor if there is no DMD memory limit and the whole system can operate at around 250 Hz. With the latest models such as Discovery 4100 from Texas Instruments, the calibration can be done easily in one minute. Also, note that system stability is critical and needs to be monitored during the whole experiment. Stability check is performed by calculating correlation coefficients of outputs for the same input over time and the system was ensured 99% stable. The input and output data was processed with the prVBEM (phase retrieval Variational Bayes Expectation Maximization) algorithm after recording. In short, this algorithm infers one row of the output field phases and one row of the TM according to each other iteratively in a Bayesian way. The iteration is stopped if the changes of both are below the threshold (i.e., in stable states). The steady values are then returned as the most possible and estimated values for each item. This algorithm is also suitable for parallel computation since estimations of different TM rows are independent. In our implementation, high performance computing

facilities were used to perform parallel calculation and it took 1 to 3 minutes to calculate one TM row, depending on algorithm convergence time. The high performance computing facility at Queen Mary University of London has a group of computation nodes with Intel Xeon E5645 and AMD Opteron 6234. The acceleration comes from parallelized jobs running on different nodes concurrently. Although it is possible to run all the parallel jobs concurrently in theory and to finish the calculation in a few minutes, it is found not practical to get that much computation resource due to jobs submitted by other users. Typically, the count of running jobs is between 100 and 200 and it would take around 4 hours to calculate the TM. With serial computation, it would take over 300 hours considering 2 minutes for one job on average.

4.3 Bayesian inference based phase retrieval

To reconstruct a complex field with only the magnitude information is the so-called phase retrieval problem. To be clear, the problem can be expressed as: with an observation y and an $M \times N$ complex-measurement matrix D, the target is to recover the signal x, such that

$$y = |Dx| \tag{4-1}$$

Translating problem (4-1) in a Bayesian framework, the missing phase information of observations and measurement noise are introduced as new variables. Therefore, each absolute value in y is given as

$$y_u = e^{j\theta_u}\left(\sum_{i=1}^{N} d_{ui} x_i^* + n_u\right) \tag{4-2}$$

where $u \in \{1 \ldots M\}$, $\theta_u \in [0, 2\pi]$ denotes missing conjugate phase of y_u and n_u stands for a zero-mean Gaussian noise with standard deviation σ_n. Moreover, it is also supposed that

$$p(x) = \prod_{i=1}^{N} p(x_i) \tag{4-3}$$

$$p(x_i) = CN(0, \sigma_x^2) \tag{4-4}$$

$$p(\theta) = \prod_{u=1}^{M} p(\theta_u) \tag{4-5}$$

$$p(\theta_u) = \frac{1}{2\pi} \tag{4-6}$$

where *CN* is circularly symmetric and complex normal distribution. With these assumptions, the missing phases in observations are taken into account naturally in the model as marginalizing on θ_u results in a distribution of y_u, only up to the moduli of y_u and $\sum_{i=1}^{N} x_i d_{ui}$.

Based on the previous model, the retrieval of the complex signal *x* can be given as the solution of the marginalized Maximum A Posterior (MAP) estimation problem as follows

$$\hat{x} = \arg\max_{x} p(x \mid y) \tag{4-7}$$

$$p(x \mid y) = \int_{\theta} p(x, \theta \mid y) \tag{4-8}$$

Due to the marginalization of the uncovered variable θ, it is intractable to calculate the $p(x|y)$ directly. However, it is possible to use sub-optimal methods to solve Equation (4-7). Here, the solution by the mean-field approximation is introduced. The mean-field approaches are to approximate the posterior joint distribution $p(x, \theta \mid y)$ by a distribution $\hat{q}(x, \theta)$ as

$$q(x, \theta) = \prod_{i=1}^{N} q_i(x_i) \prod_{u=1}^{M} q_u(\theta_u) \tag{4-9}$$

and can be addressed efficiently by VB-EM algorithm[97].

The VB-EM algorithm works in an iterative manner and updates successively the factors of the MF approximation in consideration. Considering the model and the MF approximation described previously, the following update equation can be obtained

$$q(x_i) = CN(m_i, \sum_i) \tag{4-10}$$

where *CN* denotes circularly symmetric and complex normal distribution and

$$\sum\nolimits_i = \frac{\sigma_n^2 \sigma_x^2}{\sigma_n^2 + \sigma_x^2 d_i^H d_i} \tag{4-11}$$

$$m_i = \frac{\sigma_x^2}{\sigma_n^2 + \sigma_x^2 d_i^H d_i} \langle r_i \rangle^H d_i \tag{4-12}$$

$$\langle r_i \rangle = \bar{y} - \sum_{k \neq i} m_k^* d_k \tag{4-13}$$

with

$$\bar{y} = \left[y_u e^{(j \arg(y_u^* \langle z_u \rangle))} \frac{I_1(\frac{2}{\sigma_n^2} | y_u^* \langle z_u \rangle |)}{I_0(\frac{2}{\sigma_n^2} | y_u^* \langle z_u \rangle |)} \right] \tag{4-14}$$

$$\langle z_u \rangle = \sum_{i=1}^{N} m_i d_{ui} \tag{4-15}$$

where $u \in \{1, ..., N\}$. In the previous equations, I_0 (resp. I_1) denotes order-0 (resp. 1) the modified Bessel function of the first kind, $(.)^H$ stands for the conjugate transpose and $(.)^*$ denotes scalar conjugate.

In terms of problem Equation (4-8), the approximation of $p(x|y)$ can be given as

$$\begin{aligned} p(x \mid y) &= \int_\theta p(x, \theta \mid y) \\ &\simeq \int_\theta q(x, \theta) \\ &\simeq \int_\theta \prod_i q(x_i) \prod_u q(\theta_u) \\ &\simeq \prod_i q(x_i) \end{aligned} \tag{4-16}$$

leading to the estimation of $\hat{x}_i$:

$$x_i = \arg\max_{x_i} q(x_i) = m_i \tag{4-17}$$

where $i \in \{1,...,N\}$. Therefore, the mean-field approximation results in the solution maximizing the posterior probability distribution of each x_i, rather than the complete vector x. In fact, the KL divergence decays at each iteration and the algorithm is assured of convergence because it is bounded.

In short, this algorithm jointly infers one row of the output field phase and one row of the TM iteratively in a Bayesian way. The iteration is stopped if the change to both is below the threshold (i.e., in a stable state), and the steady values are returned as the best estimates. This algorithm is also suitable for parallel computation since estimations of different TM rows are independent. In our implementation, high performance computing facilities (a group of Intel Xeon E5645 and AMD Opteron 6234) were used to perform parallel calculations, requiring 1 to 3 minutes to calculate one TM row, depending on the algorithm convergence time. The acceleration comes from parallelized jobs running concurrently on different nodes, although this approach was not extended to be fully parallel – with a theoretical calculation time of a few minutes – due to the practical limitation of jobs submitted by other users. Typically, the number of parallel jobs (number of CPU cores acquired) was between 100 and 200 requiring approximately 4 hours to calculate the TM, a large improvement over the serial case (calculated at 300 hours).

4.4 TM evaluation

In order to test the calculated TM, the TM-predicted outputs are compared with the actually recorded outputs by the camera for the same inputs in terms of the correlation coefficient, which is realized with the *corr2*/*corr* functions in MATLAB. The amplitude correlation coefficient was averaged over around 8000 input patterns and the relationship between data amount and calculated TM's prediction ability is described in Fig. 4.2. Here, P denotes the number of input patterns and N is the macro pixel count on DMD as mentioned before. It is found that more input fields for calibration could result in stronger prediction ability. In the view of Bayesian inference, the posterior probability distribution of the item being estimated will get updated and narrowed down when feeding the algorithm more and more data. Since the expectation value of the latest posterior probability is returned as the inferred value in the algorithm, the estimated value tends to deflect more from the true value if the data is not enough as the posterior is still relatively wide in this scenario, which could explain the undesirable TM

performance when P/N is insufficient. As the data is becoming bigger, the posterior would be sharp enough and the estimated value would, therefore, be very close to the true value, leading to clearly improved performance. For our setup, $P/N = 6$ is thought to be the threshold for a

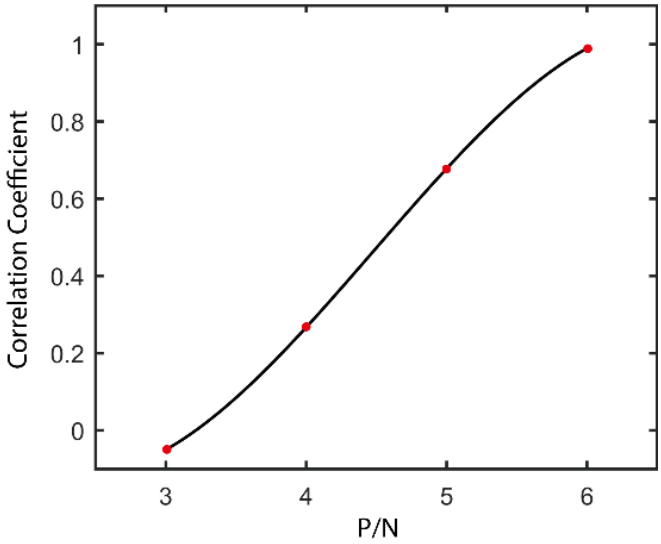

Fig. 4.2. Prediction performance expressed by correlation coefficient as a function of *P*/*N*. *N* is the count of macro pixels used on DMD while *P* denotes the number of measurements performed during calibration.

successful implementation as the corresponding prediction accuracy is around 99%, demonstrating high-quality TM estimation and precise prediction as offered by holography based methods. In the following parts, $P/N = 6$ was therefore used to ensure good performance and calculation was accelerated in a parallel way. With the help of TM, one is able to deduce the displayed DMD patterns based on recorded images on camera as well, which represents image transmission through the MMF. To demonstrate this, three pre-defined patterns ('LIV', 3.14 and a smiley face) were included intentionally in the input basis. And the phases of corresponding outputs were recovered with the algorithm as done with other random input patterns. The inferred DMD patterns E_{OP} were calculated by solving the following linear equation:

$$TM \cdot E_{OP} = E_{IP} \tag{4-18}$$

where E_{OP} and E_{IP} stand for electric field on proximal fibre end and that on distal fibre end respectively. During calibration, the DMD is working as an object so the proximal end is defined as OP while the other end is defined as IP. Typically, one may calculate E_{OP} by getting the inverse of TM first. However, the TM is not a square matrix ($N \neq M$) in most cases.

Therefore it does not have a strict inverse matrix. The *pinv* function in MATLAB can be used to calculate the so-called pseudoinverse instead and it can work as a substitute of the strict inverse. Considering our TM shape (N is a few times of M), such replacement may cause additional noise. To solve the linear equation directly can avert this problem and this implementation is faster, especially for large TM. This step is done in MATLAB and the effectiveness of TM is checked afterwards. Due to noise, TM cannot predict outputs with 100% precision but be able to achieve 98% correlation. In contrast, to calculate pseudoinverse of large matrix can be very calculation-intensive. In our case, one can save around 25% calculation time by solving linear equations directly. The inferred patterns are compared with the actual input patterns in Fig. 4.3. As shown, patterns can be observed distinctly through the MMF, demonstrating that the TM was estimated correctly and capable of undoing the information distortion caused by MMF effectively. Besides, the line width of three patterns was designed to be around 1.4 μm as an evaluation of system imaging resolution. Since the adjacent lines, as in Fig. 3 (d) and Fig. 3 (e), and small dots, as in Fig. 4.3 (e) and Fig. 4.3 (f), were separated well from the background and imaged clearly, the system imaging resolution is thought to be around 1.4 um, which is actually very close to the MMF's Abbe diffraction limit calculated as $\lambda/(2\mathrm{NA}) = 1.44$ μm. Besides, the line plots for three retrieved results are presented in Fig. 4.3 (g-i) where one can clearly see the contrast between bright pixels and dark ones. Therefore, our MMF has been demonstrated to be fully exploited and working with diffraction-limited resolution. To further improve imaging performance, one may want to utilize higher-NA MMF or to work with shorter-wavelength laser. In order to further refine the images without changing the physical setup, thresholding was performed and corresponding results are shown in Fig. 4.3 (j-l). Here, 0.5 was set as the threshold so that any values over 0.5 were reset as 1 and those below 0.5 were reset as 0. It is clear that noise was removed effectively this way, leading to very clean images. Note that binary thresholding is working here because the objects were binary. It is necessary to know the grayscale levels of the objects to carry out thresholding effectively. In addition, simple patterns were used in the experiments due to fibre mode count since the degree of freedom of the system (i.e. fibre mode count) should be sufficient to express object changes. According to our tests, the 50-μm-core MMF can work with 36×36 objects well. In order to retrieve higher resolution ones (e.g. 100×100), it is necessary to work with 100-μm-core MMF which can support around 4 times modes. The left problem is calculation speed which is at least 4 times slower. To further accelerate the computation, it is suggested to rewrite the algorithm with lower level languages (e.g. C++ or Java). In this part, DMD patterns

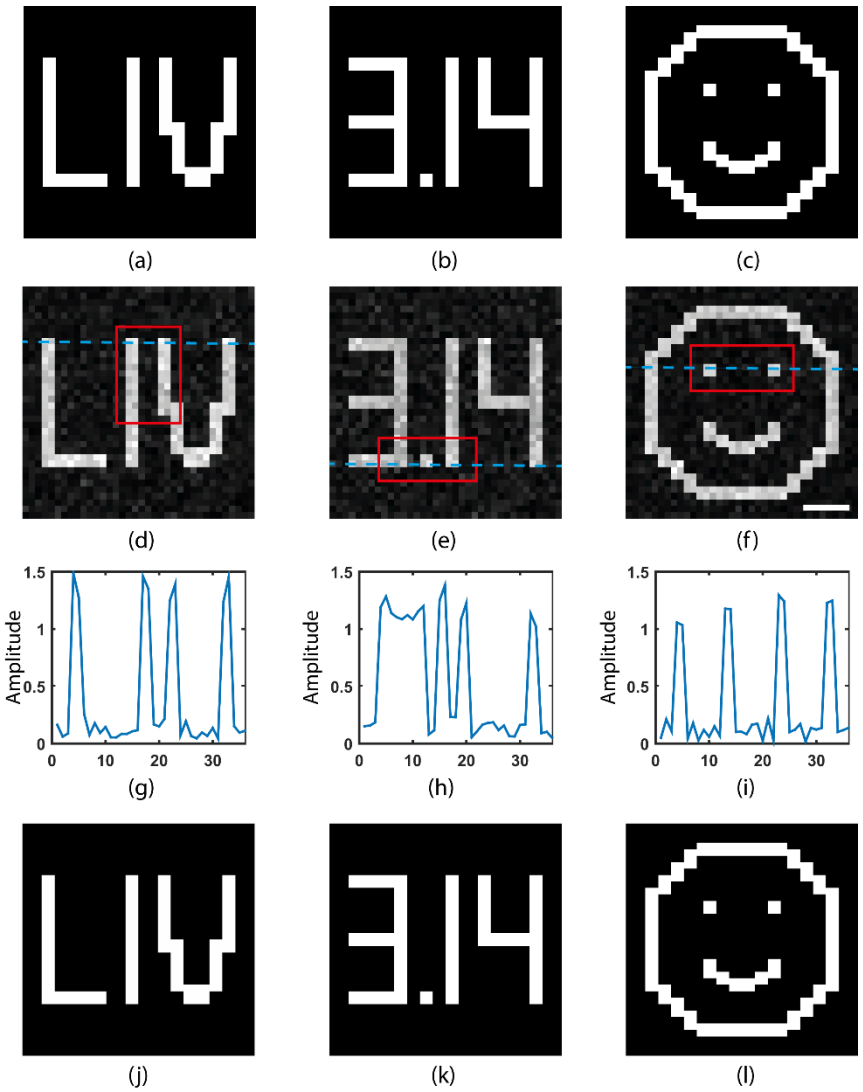

Fig. 4.3. MMF Imaging in transmission mode. (a) Original pattern of 'LIV'; (b) Original pattern of 3.14; (c) Original pattern of a smiley face; (d) Imaging result for the pattern in (a); (e) Imaging result for the pattern in (b); (f) Imaging result for the pattern in (c); (g) Line plot for (d); (h) Line plot for (e); (i) Line plot for (f); (j) Thresholding result for (d); (k) Thresholding result for (k); (l) Thresholding result for (f). Red boxes indicate the parts for resolution evaluation. Blue lines are for amplitude line plots. Scale Bar: 5 um.

worked as objects for the proof-of-concept study. Note that to do typical imaging in reflection mode may involve matching the object/camera with the modulation device[72,73] since the TM depends on the modulator's specific position. To be precise, the optical distance between the modulator and the proximal fibre end should be equal to that between object/camera and the proximal fibre end. Additionally, when matching camera with modulator, it is also suggested that they have same pixel size and pitch and that transverse displacement is minimized.

Focusing through complex media has been an interesting topic over the recent years. In order to further evaluate our system, the information in the calculated TM is utilized to perform focus

generation through the MMF. In detail, the complex conjugate of one TM row was chosen as a necessary input field for generating a focus on the distal fibre end. The position of the focus was controlled by choosing the corresponding row in the TM. To implement this complex input wave with DMD, the macro pixels where the real part is positive are selectively turned on. By doing so, it is practical to create a clear focus through the MMF, such as the one around the fibre end centre shown in Fig. 4.4 (c) and Fig. 4.4 (d) by fitting the data with a

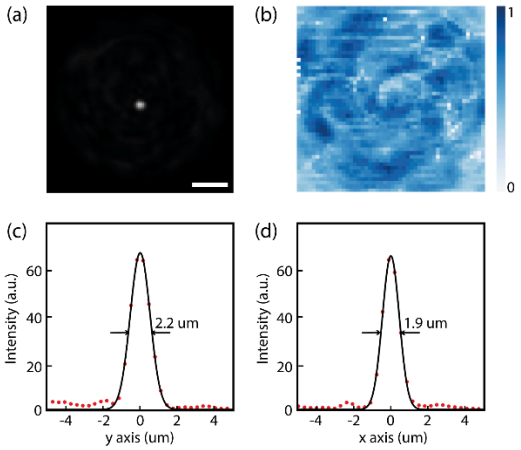

Fig. 4.4. Focus generation with the TM information. (a) A focus generated around fibre end centre. Scale bar: 10 um; (b) Normalized EF distribution across a 50 by 50 grid within distal fibre end. Grid pitch: 0.58 um; (c) Intensity profile of the focus in (a) along the y-axis; (d) Intensity profile of the focus in (a) along the x-axis.

Gaussian function. The result indicates that the full width at half maximum (FWHM) of the focus in Fig. 4.4 (a) is about 2.2 μm along the y-axis and 1.9 μm along the x-axis, The difference is attributed to the fact that the MMF is not an absolutely axisymmetric waveguide due to random fibre bending. The theoretical value of FWHM in our case is around 1.44 μm (Abbe Criterion). And the degradation results from the difference between ideal input field and practical input field. Note that input fields are processed to be binary as DMD amplitude modulation is not continuous. Such field transformation will inevitably cause that doable input is actually different from the ideal one. Moreover, by choosing different TM rows, the focus is scanned across a 50 by 50 grid within fibre end and recorded the intensity enhancement factors (EFs), defined as the ratio of the focus peak value to the average value of output generated by a random input. The normalized EF distribution is presented as a heat map in Fig. 4.4 (b). It is found that the maximum EF = 70 was obtained and the level of enhancement is obviously over the result achieved by genetic algorithm[98], thanks to fully exploiting spatial modes in the MMF and to accurate phase retrieval with the algorithm. Further improvement can be obtained by using more macro pixels on DMD and higher-NA fibres as done in Ref[58]. It is also observed

that the focus quality is not uniform over the fibre end. As mentioned, the modulation ability of DMD is limited by its binary feature and the actual input fields are more or less different from the ideal ones. Since the degree of such deflection is case by case, it is reasonable that to generate a high-quality focus is difficult in specific positions, leading to an unbalanced EF distribution. To get a higher EF or a more balanced EF distribution, one may want to utilize more macro pixels on DMD or to use SLM instead (slower though) as both approaches will bring stronger modulation ability and control the input field more precisely.

4.5 Geometry sensitivity investigation

With the demonstrated TM acquisition setup, a 30-cm MMF's sensitivity to bending is further tested. Here, the experimental setup was same as the one in Fig. 4.1 except for that the middle part of the MMF was fixed on an additional 1-D translation stage. The imaging process in Fig. 4.3 was carried out with different translation distances but only the original TM was used to retrieve the object information. The degradation of the image quality is clearly observed in Fig. 4.5 and indicates the sensitivity of the MMF. The translation step was 10 um in this experiment and one can hardly see any object information with 50-um movement. This particular MMF was much more sensitive to bending compared to the results in Ref[55,76,77]. This is attributed to

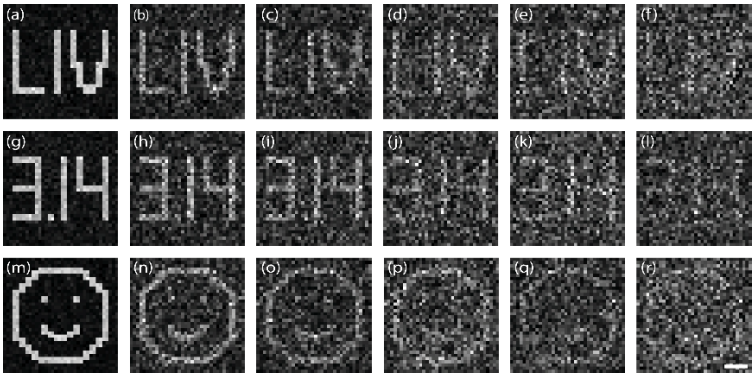

Fig. 4.5. MMF Imaging results with gradual translations. (a), (g) and (m) are results without translation; (b), (h) and (n) are results with 10-um translation; (c), (i) and (o) are results with 20-um translation; (d), (j) and (p) are results with 30-um translation; (e), (k) and (q) are results with 40-um translation; (f), (l) and (r) are results with 50-um translation. Scale bar: 5 um.

the fact that 0.22-NA step-index MMF was utilized here. As demonstrated in Ref[76,77], MMF with large NA is less sensitive. Also note that the specific S-shaped fibre was used in Ref[55,77], which is another reason for better performance. However, the practical fibre deformation cannot guarantee that the S shape is always maintained. Therefore more robust bending-

insensitive fibre geometry is looked into. To the best of our knowledge, the initial bending degree has never been studied as a factor for sensitivity. Since the degree of fibre bending indicates the degree of mode coupling, the fibre with severe initial bending is assumed to have strong initial coupling while the one with medium initial bending is supposed to have medium initial coupling. Here, a 1.5-m MMF was initialized with strong or medium coupling, which was realized by severe or mild coiling. The corresponding fibre arrangements are presented in Fig. 4.6 (a) and Fig. 4.6 (b) respectively, where the yellow arrows indicate the position and direction of additional translation from the stage. Both fibre ends were fixed during the experiments and the outputs for the same input was monitored when moving the translation

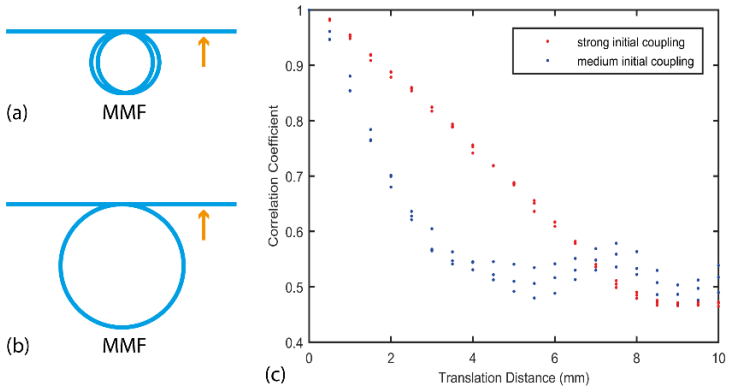

Fig. 4.6. MMF bending sensitivities with different initial coupling. (a) Fibre arrangement for strong initial coupling. (b) Fibre arrangement for medium initial coupling. (c) Sensitivity comparison between two scenarios. Yellow arrows indicate translation direction.

stage. The sensitivities of fibre with different initial coupling are compared in Fig. 4.6 (c). It is apparent that both cases are much better than the one for Fig. 4.5 since correlation coefficient is over 95% after 1-mm translation with strong initial coupling and that is over 85% after 1-mm translation with medium initial coupling. Both scenarios were tested three times to filter out the impact of system noise. It is found that the results are basically stable and are thought effective statistically. The sensitivity improvement can be explained by relative coupling change. With the same translation distance, relative coupling change is less obvious if with stronger initial coupling, leading to better sensitivity. In the real applications, one may want to keep the strong initial coupling part rigid and to use the remaining part in a semi-flexible manner.

4.6 Summary

In conclusion, distinct from previous methods, it has been demonstrated that full transmission matrix of an MMF is achievable in a reference-less setup and with phase retrieval techniques. Rather than recording holograms with interference setup to recover phase information, intensity images are recorded here and phase information are extracted by the Bayesian inference based phase retrieval algorithm. Such configuration leads to not only a simplified system but also better system stability. The TM is also calculated by the phase retrieval algorithm where TM elements and phase information are inferred iteratively until both of them are stable. The whole calibration process can be accelerated by distributed calculation, which would take around 5 hours in practice. In addition, the generated TM has also been examined to have strong prediction ability, to be able to perform diffraction-limited imaging and to be capable of concentrating light into a clean focus. Furthermore, it has been validated that MMF geometry sensitivity can be effectively depressed with strong initial coupling. It is believed that the proposed setup improves the current approaches and opens a new way for MMF characterization. As a fast, robust and semi-flexible implementation, it can also be a promising candidate for MMF focusing and endoscopic imaging.

This page is left blank intentionally.

Chapter 5 Properties of transmission matrix of multimode fibre imaging system

In the last chapter, the transmission matrix of the multimode fibre imaging system is successfully obtained in a reference-less way. To the best of our knowledge, most of the works in this area are on using transmission matrix to generate focus/patterns or to perform imaging. In contrast, other properties of the transmission matrix have not been extensively studied. In this chapter, transmission matrix of MMF is analysed mathematically and more insights are extracted from it. Specifically, the mode count inside fibre is measured accurately and eigenchannels for better energy delivery are disclosed as well. Moreover, it is observed that TM phase is more sensitive to additional bending than TM amplitude, which contributes more to TM degradation.

5.1 Measurement of mode count in multimode fibres

In fibre-based optical communication, multimode fibres have been demonstrated to have better information transport efficiency since a great number of spatial modes travelling inside enable parallel information delivery. Investigations have been carried out in directions such as mode multiplexing[99], dispersive multiplexing[100] as well as image transmission[101] through multimode fibres. However, fibres are not straight and deformation-free in most practical applications. The bending or twist of multimode fibres would impact mode properties such as mode propagation constant, mode transmittance as well as mode count in a specific fibre, leading to potential problems when utilising multimode fibres to deliver information.

Compared to ideal fibres, it is much harder to confirm the mode properties of a practical fibre with deformations to some degree. For ideal multimode fibres, one can easily estimate the mode count N_m by

$$N_m \approx 0.5 \times V^2 \tag{5-1}$$

where V stands for the normalised frequency of the multimode fibre. Equation (5-1) is obtained by solving Helmholtz function for step-index fibres and it is assumed V is large enough[102]. Further, the normalised frequency can be calculated by

$$V = 2\pi a \cdot NA / \lambda \tag{5-2}$$

where a denotes fibre core radius, NA stands for its numerical aperture and λ is laser wavelength. When dealing with fibres with deformations, one can hardly solve the wave equations due to the asymmetry of fibres, complex boundary conditions and unknown deformation situations. Therefore, it is not easy to achieve the mode properties of randomly deformed multimode fibres. In the last chapter, it has been demonstrated that transmission matrix of a multimode fibre imaging system can be achieved in a reference-less setup. This transmission matrix is able to describe how light field is changing through the whole system by relating independent modes on input plane with those on output plane. Here, it is further demonstrated that it is practical to achieve the actual mode count in a multimode fibre by calculating the rank of its transmission matrix.

In the viewpoint of mathematics, the elements in transmission matrix are coefficients of linear equations relating input and output pixels. Therefore the rank of the matrix indicates the count of independent equations, which is also the number of degrees of freedom in the imaging system. Note that the input light fields need to couple into fibre modes to propagate in the multimode fibre and that the number of the spatial modes is the count of degrees of freedom of the system. Therefore one can deduce that the rank of transmission matrix is actually the number of modes travelling in the multimode fibre. Since transmission matrix is available in the experiment, it offers a practical method to achieve a number of fibre modes regardless of the specific states of deformations and abnormal solutions of wave equations.

To record the transmission matrix of a specific multimode fibre, we used the experimental setup introduced in the last chapter. Please refer to Fig. 4.1 for detailed information. In short,

a number of random input patterns are displayed on the DMD and are delivered into the fibre proximal end. The corresponding output images on fibre distal end are captured by the camera directly without interference. The prVBEM algorithm is afterwards utilised to infer the phase information in all output images and to calculate the full elements in transmission matrix. With the transmission matrix, one can easily obtain its singular values by singular value decomposition (SVD):

$$TM = U \cdot S \cdot V^{*} \tag{5-3}$$

Here, U and V are unitary matrices while S is a diagonal matrix with non-negative real numbers on diagonal, which are singular values of TM and (*) denotes conjugate transpose. In theory, the rank of the TM is the count of positive singular values.

In terms of linear algebra, the singular value decomposition is a type of factorization of a real or a complex matrix. It is the generalization of the eigen-decomposition a positive semidefinite normal matrix to any $m \times n$ matrix by an extension of the polar decomposition. It has many useful applications in both statistics and signal processing. Generally, the singular value decomposition of an $m \times n$ matrix M is a factorization of the form $U_0 S_0 V_0^{*}$. Here, U_0 is an $m \times m$ real or complex unitary matrix, S_0 is an $m \times n$ rectangular diagonal matrix with non-negative real numbers on the diagonal, and V_0 is an $n \times n$ real or complex unitary matrix. The diagonal entries of S_0 are the so-called singular values of M. The columns of U_0 and the columns of V_0 are knowns the left-singular vectors (LSV) and right-singular vectors (RSV) of M. Since U_0 and V_0^{*} are unitary, the columns of each of them are a set of orthonormal vectors which can be seen as basis vectors. According to properties of the unitary matrix, the same is true for their conjugate transpose U_0^{*} and V_0. So the columns of U_0, U_0^{*}, V_0, and V_0^{*} are orthonormal bases.

The Singular-value decomposition can be computed by the following properties:

1. The left-singular vectors of M are a set of orthonormal eigenvectors of MM^{*}.
2. The right-singular vectors of M are a set of orthonormal eigenvectors of $M^{*}M$.
3. The non-zero singular values of M are the square roots of the non-zero eigenvalues of both MM^{*} and $M^{*}M$.

The applications employing the SVD include calculating the pseudoinverse, least squares fitting of data, multivariable control, matrix approximation, and determining the rank, range and null space of the original matrix. For instance, the rank of the original matrix is the count of its positive singular values. Also, the singular-value decomposition can be utilised to compute the pseudoinverse of a matrix. Actually, the pseudoinverse of the matrix M with singular-value decomposition as

$$M = U_0 \cdot S_0 \cdot V_0^* \tag{5-4}$$

is matrix M^+ which can be expressed as

$$M^+ = V_0 \cdot S_0^+ \cdot U_0^* \tag{5-5}$$

where S_0^+ is the pseudoinverse of S_0, which can be calculated by replacing all non-zero diagonal entries by its reciprocal and transposing the resulting matrix. Also, the pseudoinverse is one approach to address linear least squares problems.

The singular-value decomposition is quite general since it can be applied to arbitrary $m \times n$ matrix while eigenvalue decomposition (ED) can be applied only to specific types of square matrices. However, these two decompositions are related. Speaking of the singular value decomposition of any $m \times n$ matrix M, as introduced above, the following two equations exist:

$$M^*M = V_0 S_0^* U_0^* U_0 S_0 V_0^* = V_0 (S_0^* S_0) V_0^* \tag{5-6}$$

$$MM^* = U_0 S_0 V_0^* V_0 S_0^* U_0^* = U_0 (S_0 S_0^*) U_0^* \tag{5-7}$$

The right-hand sides of the two equations express the eigenvalue decomposition of the left-hand sides. Therefore, the following properties exist:

1. The columns of V_0 (right-singular vectors) are eigenvectors of M^*M.

2. The columns of U_0 (left-singular vectors) are eigenvectors of MM^*.

3. The non-zero elements of S_0 (non-zero singular values) are the square roots of the non-zero eigenvalues of M^*M or MM^*.

In the particular scenario that M is a normal matrix, which is also a square matrix by definition, the spectral theorem indicates that it can be unitarily diagonalized using a basis of eigenvectors. Therefore it can be expressed as

$$M = U_0 \cdot D_0 \cdot U_0^* \tag{5-8}$$

for a unitary matrix U_0 and a diagonal matrix D_0. When M is positive semi-definite as well, the decomposition in Equation (5-8) is a singular-value decomposition also.

In Fig. 5.1, the singular value distribution of the *TM* of a multimode fibre is presented. It is clear that the singular value drops obviously with the increasing of mode index. Since the squared singular value indicates mode transmittance, our observation is in line with the fact that higher-order modes experience larger loss. Also note that all the singular values are positive strictly in this *TM*, indicating the rank of *TM* is 1296. However, considering the noise level in the system, effective rank of the matrix is defined by the specific mode index, N_R, such that the area below the curve up to N_R is 98% of the total area. The noise level in the system is estimated by checking the correlation coefficient between predicted output and captured output (as shown in Fig. 4.1). Note that the noise level may vary for different systems, depending on

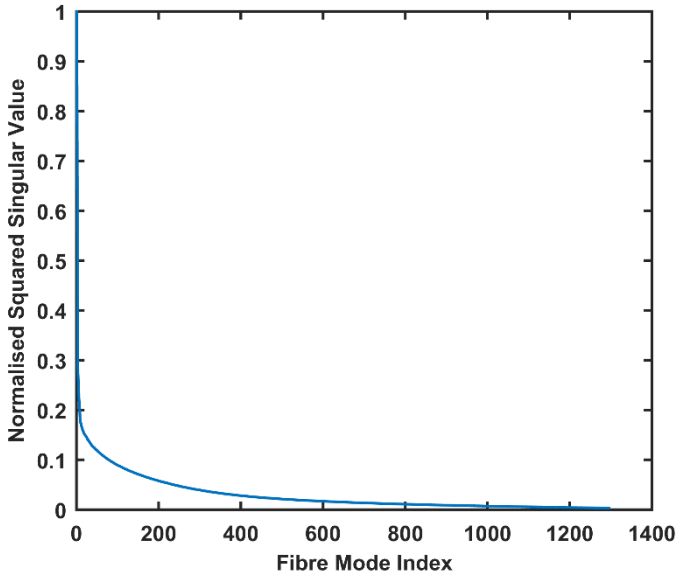

Fig. 5.1. Distribution of singular values of the TM.

detailed experimental setup. And it is calculated to be 0.02 for the system used here, therefore leading to an effective rank of 840. This the number is close to 755, half of the estimation from Equation (5-1). The reason why half estimation is used here is that a polarizer is utilised in our

experimental system. Therefore fibre modes in one polarisation direction are filtered out. Considering this, one can still see the difference. And this is due to two reasons. First, Equation (5-1) is more accurate for large normalised frequency while the one for this multimode fibre is around 50. Second, Equation (5-1) is for ideal straight fibre while the real fibre is with imperfect index distribution as well as random bending or twisting. Moreover, it is reasonable that the number of modes supported in the multimode fibre is up to its geometry, which cannot be explained by Equation (5-1). Here, the additional fibre stage further is translated to lead to the change of transmission matrix rank. As presented in Fig. 5.2, one can see fewer fibre modes are supported in the fibre if more translation is introduced. In our setup, more translation leads to more severe bending. According to fibre theory, energy is more likely to couple to cladding modes or radiation modes in this case, which can explain the decreasing of fibre mode count.

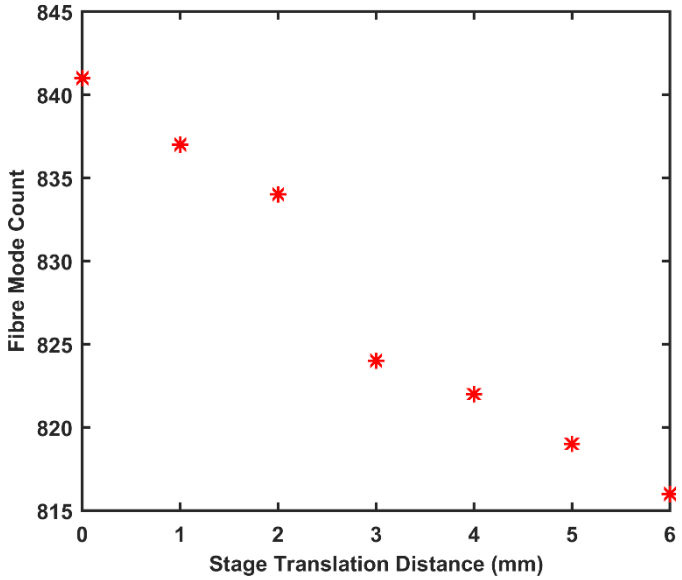

Fig. 5.2. Change of fibre mode count over additional stage translation.

5.2 Maximum energy delivery through multimode fibres

As mentioned in Chapter 2, the energy coupling efficiency is up to input field distribution as well as fibre mode distributions. Normally, more overlapping between input field and mode field will result in better coupling efficiency. Also, different modes experience various transmission loss and this is also related to specific fibre geometry. Therefore the energy transport efficiency is different for distinct input patterns. In Ref[37,38], Choi's group studied eigenchannels in scattering medium to maximise energy delivery efficiency. To the best of our

knowledge, similar work has not been done for multimode fibres. Here, the transmission matrices of multimode fibres are measured and corresponding eigenchannels are demonstrated to effectively enhance energy transport.

The experimental setup is the same as in Fig. 4.1. And to construct full transmission matrix without interference is realistic thanks to the help of prVBEM algorithm as demonstrated in Chapter 4 and last section. Similarly, one also needs to perform singular value decomposition for the transmission matrix according to Equation (5-3). In the last section, the effective rank of matrix S is used to determine the mode count in a specific fibre. Here, it is further demonstrated that the column vectors in matrix V are actually eigenchannels in the transmission matrix and the first one of them corresponds to the input patterns with maximum energy delivery efficiency. With a transmission matrix, one can first study the energy transport for each eigenchannel theoretically. In order to do this, column vectors of matrix V are virtually injected into the fibre and obtained corresponding outputs with the help of TM. The normalised

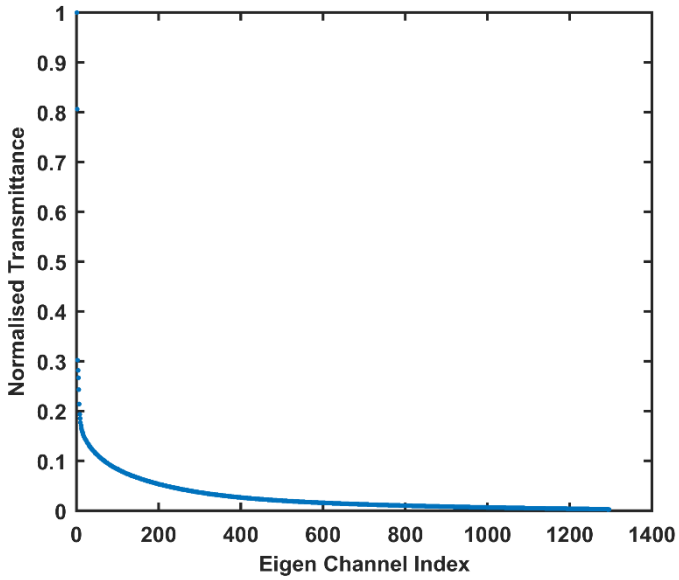

Fig. 5.3 Normalised transmittance of eigenchannels.

energy delivery efficiency is shown in Fig. 5.3 and one can clearly see the descending trend, indicating the first column vector is optimal for energy transport. Besides, the normalised energy delivery efficiency values are exactly the normalised squared singular values, indicating the physical meaning of the singular values of transmission matrix. Note that output images for random input patterns are measured in order to construct TM. Here, the input and output data

are used to calculate the energy transport efficiency for random input patterns. In addition, the best eigenchannel is implemented in the experiment and the corresponding output is recorded.

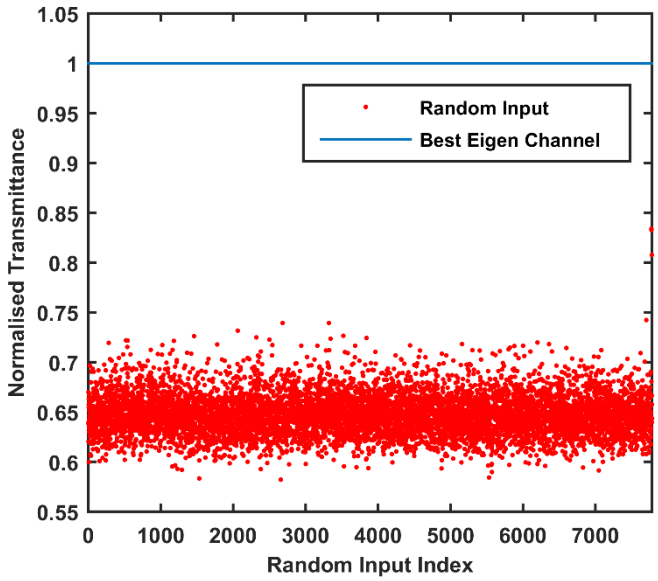

Fig. 5.4. Normalised transmittance for random input patterns.

The energy delivery efficiency for random patterns is normalised to that of best eigenchannel and the results are presented in Fig. 5.4. In this experiment, one can observe that the energy transport efficiency for the eigenchannel is obviously higher than that of random patterns. Specifically, one can expect over 1.5 times enhancement. However, this value is still certainly away from theoretical enhancement which is around 8 times in our case. Here, the optimal pattern is virtually injected into the system and theoretical enhancement factor is calculated with corresponding output predicted by TM. The primary reason for the enhancement difference is that binary amplitude modulation by the DMD is used in the system, which would inevitably involve imperfection as the ideal input pattern has both amplitude and phase information while DMD itself can only offer binary amplitude modulation. One can expect to achieve better results by using an SLM to offer phase modulation or using a DMD as phase modulator (Lee hologram). The practical eigenchannel and perfect eigenchannel are compared in Fig. 5.5 where their corresponding output patterns are also presented. The shape of the eigenchannel depends on the TM which is determined by the fibre geometry such as bending. Since the fibre is not straight placed, it is reasonable that the eigenchannel does not look symmetric. Also, although we tried to maintain a uniform input light field on DMD, a degree of uniformity may still exist. All these led to unbalanced observation. As shown, due to the difference between the realistic pattern and the ideal pattern, the outputs are clearly distinct,

leading to lower energy delivery efficiency. This drawback significantly limits our ability to generate accurate patterns on the fibre proximal end as mentioned in the last chapter. Nevertheless, the improvement on the energy transport efficiency with imperfect input patterns demonstrates the existence of eigenchannels. A great improvement may be predicted if using a phase modulator such as LC-SLM or by using a DMD with a lens to offer phase modulation as in [10]. In our experiment, the fibre proximal end is aligned with OL1 in Fig. 1 by maximizing the fibre output power with all DMD macropixels turned on. Since the transmission matrix describes the optical transmission from the DMD to the camera, the transmission properties (e.g. eigenchannels) are affected by both the distance and the angle between OL1 and the fibre proximal end.

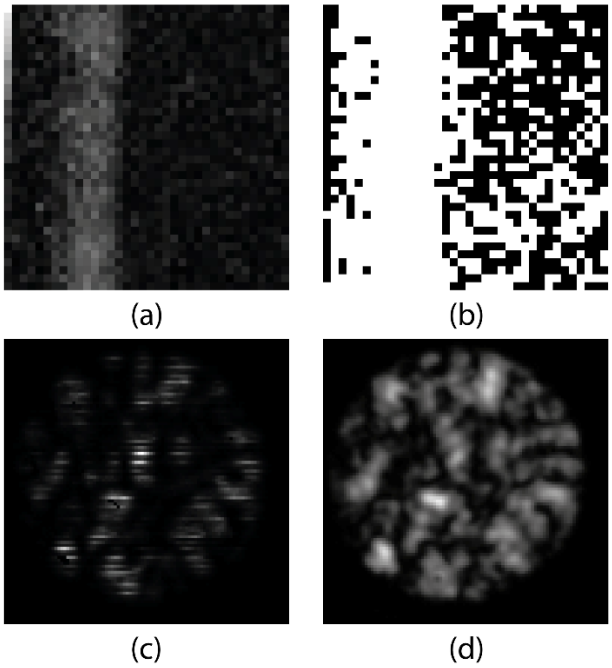

Fig. 5.5. Comparison of the ideal and practical eigenchannels. (a) Ideal input amplitude; (b) Practical input amplitude; (c) Theoretical output pattern; (d) Realistic output pattern.

5.3 TM deformation with bending

The fundamental problem preventing the multimode fibre from being used in real applications is its sensitivity to state change such as geometry and temperature. Especially, fibre deformation can lead to significant TM change and that is why demonstrated MMF imaging systems are either with limited flexibility or working with fixed MMF. In order to overcome this problem, works have been done on fibre comparison and selection to minimise

sensitivity[76,77]. Also, Caravaca-Aguirre *et al*. achieved real-time TM measurement with the help of DMD and FPGA[75] while Plöschner *et al*. realised TM prediction by accurate modelling the whole multimode fibre imaging system[79].

Fibre mode count and eigenchannels have been studied based on information in the TM in the last two sections and how TM changes with additional bending are studied in this section. A typical TM is shown in Fig. 5.6 with both amplitude and phase information. Since the pixel counts are different for input patterns and output patterns, the matrix is not square. Actually, there are much more rows (much more pixels for output patterns) here due to the requirements of the phase retrieval algorithm. As shown in Fig. 5.6, the information is quite randomly distributed in the TM. Also, there are a certain number of black rows across the whole TM amplitude distribution. Note that TM elements close to zero are illustrated in black. The reason why there are those black rows is that the camera is capturing the light field on the whole fibre end. Since the camera's field of view is a rectangle, the corner parts are always black (the light is confined to the fibre core). And the black rows can be easily explained by linear equations. The prediction by a black row of TM can be expressed by the linear equation:

$$t_1 x_1 + t_2 x_2 + t_3 x_3 + \ldots + t_n x_n = \sigma \tag{5-9}$$

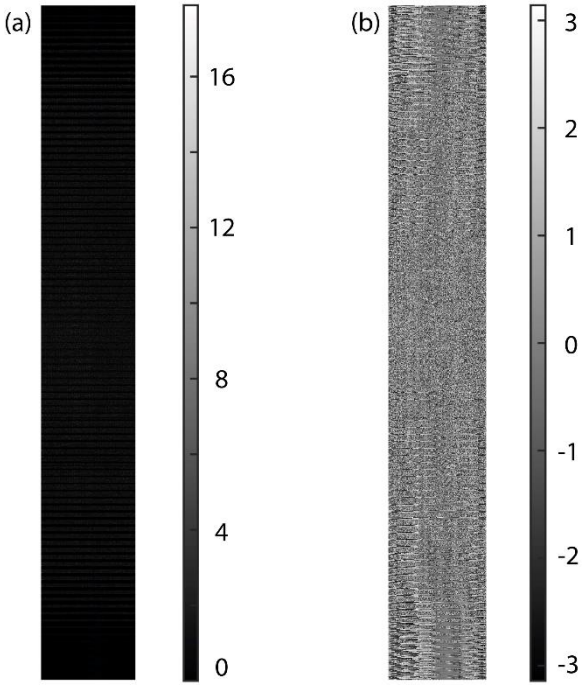

Fig. 5.6. A typical transmission matrix. (a) amplitude information; (b) phase information (rad).

where σ is a small value rather than absolute zero due to system noise, t_i is the element in one black row of the TM and x_i is the pixel value of input pattern. For the output pixels beyond fibre end, Equation (5-9) should be valid for all the possible input vectors, which means the coefficients have to be close to zero. Therefore the black rows can be observed in the TM

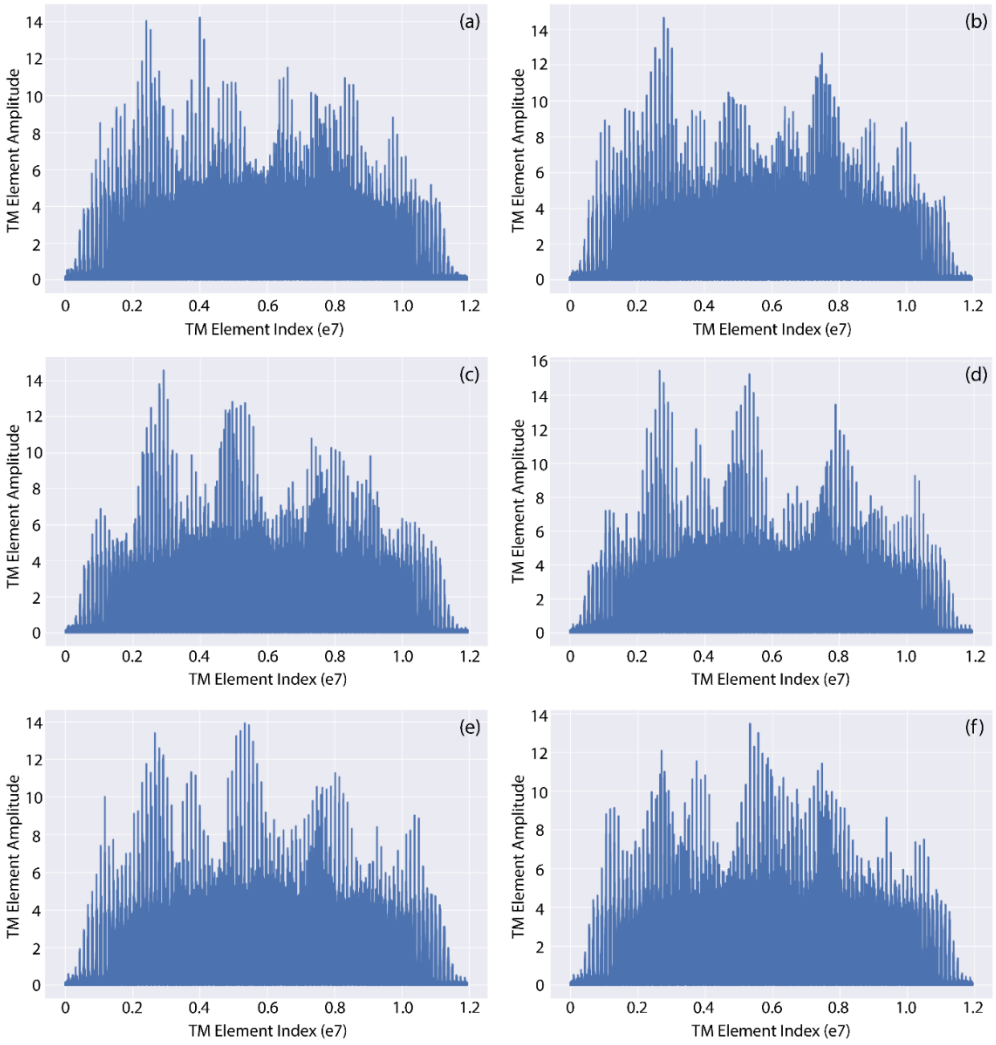

Fig. 5.7. Deformation of transmission matrix with additional bending (controlled by translation distance, d) (a) d = -2 mm; (b) d = -1 mm; (c) d = 0 mm; (d) d = 1 mm; (e) d = 2 mm; (f) d = 3 mm.

amplitude distribution and they actually indicate the positions of those pixels beyond fibre distal end. In addition, there are more black rows on the top and the bottom since they correspond to pixels on the corners in the output images.

In this section, one fibre stage is also gradually translated to introduce additional bending of the MMF. The calibration was performed for all the states. And the change of the TM can be clearly observed in Fig. 5.7. Only TM amplitude is shown here and all TM elements are rearranged horizontally for better visualisation. It is shown that there are a number of peaks in

these TM distributions and TMs are experiencing obvious change with additional bending since mode coupling situation is greatly changed. Taking phase change into account, the variation of TM is even more apparent. Although the change is obvious, it is still quite challenging to model it. Some works have been done regarding flexible MMF imaging but detailed fibre geometry needs to be clear, which is only possible in a highly controlled scenario. For randomly distributed MMF, it may be more promising to calibrate it in real time rather than to infer the updated TM by its geometry. The correlation coefficients of these TMs are calculated and presented in Fig. 5.8, indicating that TM is severely distorted with additional bending. With 1-mm translation, the correlation coefficient for TM amplitude and phase can drop to around 0.7 and 0.3 respectively in our experimental setup. Also, it is found that phase is much more sensitive to additional bending than amplitude, which contributes more to TM distortion.

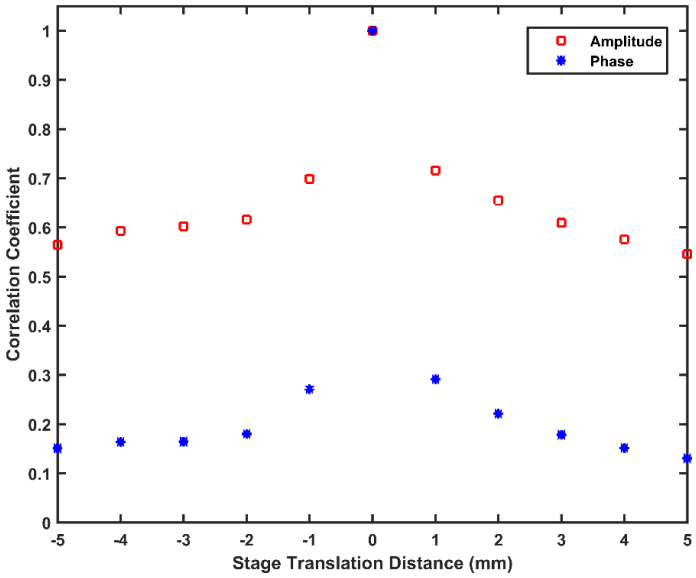

Fig. 5.8. The change of TM amplitude and phase with additional bending.

5.4 Summary

The transmission matrix can not only be used to undo image distortion. In this chapter, mathematical methods are utilised to analyse recorded transmission matrices and to extract more insights from it. As known, the rank of system transmission matrix represents the degrees of freedom of the system. For MMF imaging system, the degrees of freedom is also up to the count of supported fibre modes. Therefore, it is reasonable to infer the accurate mode count by calculating the rank of measured transmission. With the help of singular value decomposition,

the rank of the MMF transmission matrix can be easily obtained. In order to acquire accurate mode count, effective rank of the matrix is calculated since all the singular values are positive since there is noise in the experiment system. In addition, eigenchannels are also available after singular value decomposition of the transmission matrix. It has been demonstrated that the energy delivery efficiency can be obviously improved (around 50% better) by using the best eigen-channel as the input pattern. Moreover, how TM changes with additional bending is presented in detail and it is found that TM phase is much more sensitive to bending than TM amplitude, demonstrating the former contributes more to TM deformation.

This page is left blank intentionally.

Chapter 6 Summary and outlook

6.1 Summary of the thesis

The developments of single multimode fibre based imaging systems are demonstrated in the thesis both theoretically and experimentally. Due to the characteristics such as small cross section and large count of supported mode, multimode fibre is a promising component candidate for high-resolution endoscopic imaging. Specifically, the work in this thesis is divided into three parts. Firstly, modelling of single multimode fibre imaging system is presented in Chapter 3. Secondly, reference-less characterisation of multimode fibre imaging system is demonstrated in Chapter 4. Thirdly, the data analysis on transmission matrix of the multimode fibre imaging system is carried out in Chapter 5.

In Chapter 3, a theoretical model for single multimode fibre imaging system is constructed based on fibre optics as well as Fourier optics. Specifically, the light propagation in free space is described with diffraction to generalize the model since there may be space between object/image plane and fibre end while mode theory is used to deal with light travelling inside the fibre. By solving wave equation, mode count and mode propagation constants can be calculated and light field in fibre core can be expressed as the sum of fields of all the supported spatial modes. Also, it is shown that multimode fibre would normally scramble the original information and lead to speckle outputs due to complex processes including mode coupling and mode dispersion. The former is highly related to fibre geometry since fibre bending would impact mode energy change degree (i.e. coupling coefficient). This also explains why the multimode fibre imaging system is not flexible and offers a way to study the bending impact on fibre transmission characteristics. Besides, the idea of TM based image retrieval was demonstrated with our model. And it is shown that original object information can be well retrieved if TM is available after calibration. The influence of system parameters was also

studied. It is demonstrated necessary to have fibre mode count around original image pixel count to recover the information effectively because fibre mode count stands for the degree of freedom in the imaging system. It is also shown that multimode fibres supporting more spatial modes are more flexible as additional bending impact are shared among all the modes. Finally, a single-shot multimode fibre imaging system by illuminating objects with highly controlled fields was proposed and demonstrated. This system utilises knowledge of TM to generate engineered illumination fields and to retrieve object information. The TM is used more sufficiently and the setup, therefore, enables faster image acquisition. The recovery result is also comparable to that obtained with point scanning method.

In Chapter 4, distinct from previous methods, it has been demonstrated that full transmission matrix of an MMF is achievable in a reference-less setup and with phase retrieval techniques. Rather than recording holograms with interference setup to recover phase information, intensity images are recorded here and phase information is extracted by the Bayesian inference based phase retrieval algorithm. Such configuration leads to not only a simplified system but also better system stability. The TM is also calculated by the phase retrieval algorithm where TM elements and phase information are inferred iteratively until both of them are stable. The whole calibration process can be accelerated by distributed calculation, which would take around 5 hours in practice. In addition, the generated TM has also been examined to have strong prediction ability, to be able to perform diffraction-limited imaging and to be capable of concentrating light into a clean focus. Furthermore, it has been validated that MMF geometry sensitivity can be effectively depressed with strong initial coupling. It is believed that the proposed setup improves the current approaches and opens a new way for MMF characterization. As a fast, robust and semi-flexible implementation, it can also be a promising candidate for MMF focusing and endoscopic imaging.

In Chapter 5, the transmission matrix can not only be used to undo image distortion. In this chapter, mathematical methods are utilised to analyse recorded transmission matrices and to extract more insights from it. As known, the rank of system transmission matrix represents the degrees of freedom of the system. For MMF imaging system, the degrees of freedom is also up to the count of supported fibre modes. Therefore, it is reasonable to infer the accurate mode count by calculating the rank of measured transmission. With the help of singular value decomposition, the rank of the MMF transmission matrix can be easily obtained. In order to acquire accurate mode count, effective rank of the matrix is calculated since all the singular

values are positive since there is noise in the experiment system. In addition, eigenchannels are also available after singular value decomposition of the transmission matrix. It has been demonstrated that the energy delivery efficiency can be obviously improved (around 50% better) by using the best eigenchannel as the input pattern. Moreover, how TM changes with additional bending is presented in detail and it is found that TM phase is much more sensitive to bending than TM deformation.

6.2 Outlook of future works

Due to its physical nature, multimode fibre is a promising candidate for the high-resolution imaging device. However, at least two primary problems need to be addressed in order to apply it in real imaging applications.

First of all, in order to work as an endoscope, one may want to calibrate the multimode fibre without access to the distal end since this end would face objects rather than cameras in real applications. One possible solution is to produce a half reflection film on fibre distal end and to use film-reflected light to construct transmission matrix. Gu *et al*. have done theoretical work[78] on this approach and more works need to be done in experiments. Also, in order to separate the film-reflected light and the object-reflected light, one may want to carry out fluorescence imaging since the former and the latter can be well separated by wavelength. In contrast, Caravaca-Aguirre *et al*. demonstrated real-time fibre calibration and focus generation with the help of DMD and FPGA[75], which can get rid of acquiring detailed fibre geometry. By combing this scheme and reflection film on fibre distal end, it is promising to develop practical flexible endoscopes based on single multimode fibres.

In addition, another fundamental problem is how to use the multimode fibre with great flexibility. Plöschner *et al*. predicted TMs with further bending successfully by an accurate model[79]. However, the effectiveness of the model is severely limited by fibre length. More importantly, it is necessary to know the exact fibre geometry to predict TM in their model, which is not practical in real applications. In order to address this problem, it is suggested to use special multicore fibres rather than simple multimode fibres. Specifically, a type of four-core fibre has been designed by the group and has been fabricated by the Yangtze Optical Fibre and Cable Joint Stock Limited Company. This particular fibre has one large fibre core in the centre and another three small surrounding fibre cores. The centre one is used as the normal

multimode fibre core to deliver images and can be calibrated by method demonstrated before. The cross-section of this type fibre is shown in Fig. 6.1.

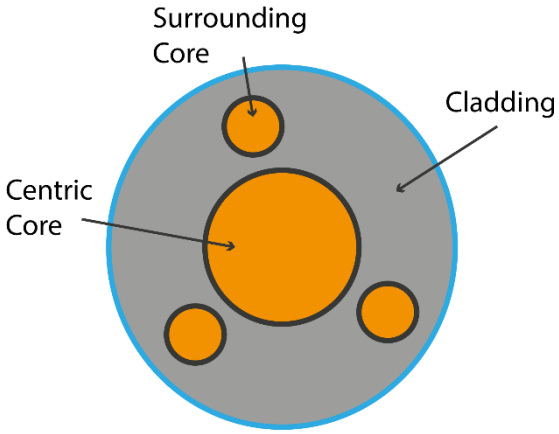

Fig. 6.1. Cross-section of designed 4-core fibre.

Also, Fibre Bragg gratings (FBGs) are supposed to be written on the three surrounding cores and to work as sensors for the fibre 3D shape. The sensing ability comes from the FBG ability to reflect specific wavelength given as

$$\lambda_{Bragg} = 2n_e P \tag{6-1}$$

where λ_{Bragg} is the Bragg wavelength, n_e denotes effective fibre core index and P stands for grating period. The structure of fibre Bragg grating is presented in Fig. 6.2 for reference. Due to the periodic change of fibre core index, the grating can work as a band-rejection filter. Note that the effective fibre core index is up to its deformation since fibre bending leads to fibre core density change. Therefore, fibre gratings can be used to detect the detailed fibre deformation which is the prerequisite to use the model in Ref[79] to further infer fibre transmission matrix with additional bending.

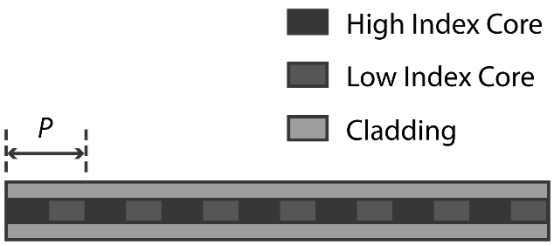

Fig. 6.2. Structure of fibre Bragg gratings.

Another promising working direction is to construct a more practical transmission function rather than transmission matrix. As discussed, the transmission function is a matrix as complex fields are being considered. However, to obtain phase information is not straightforward normally since holography setup or phase retrieval technique is therefore necessary. In contrast, applications would be much easier if it is possible to construct a transmission function based on light intensity or amplitude that are recorded by camera directly. Since phase information is missing, the transmission function is no longer a matrix in this scenario. With the rapid development of artificial intelligence (AI) these years, artificial neural networks (ANN) are being applied in many cases especially those regarding image processing or classification. It is proposed here to utilise well demonstrated convolutional neural network (CNN) to construct a transmission function bridging input image amplitude and output image amplitude directly. Some initial results in Fig. 6.3 indicate that this can be a very promising direction. Here, hand-written patterns of 1, 2 and 3 are recovered by the CNN and results are

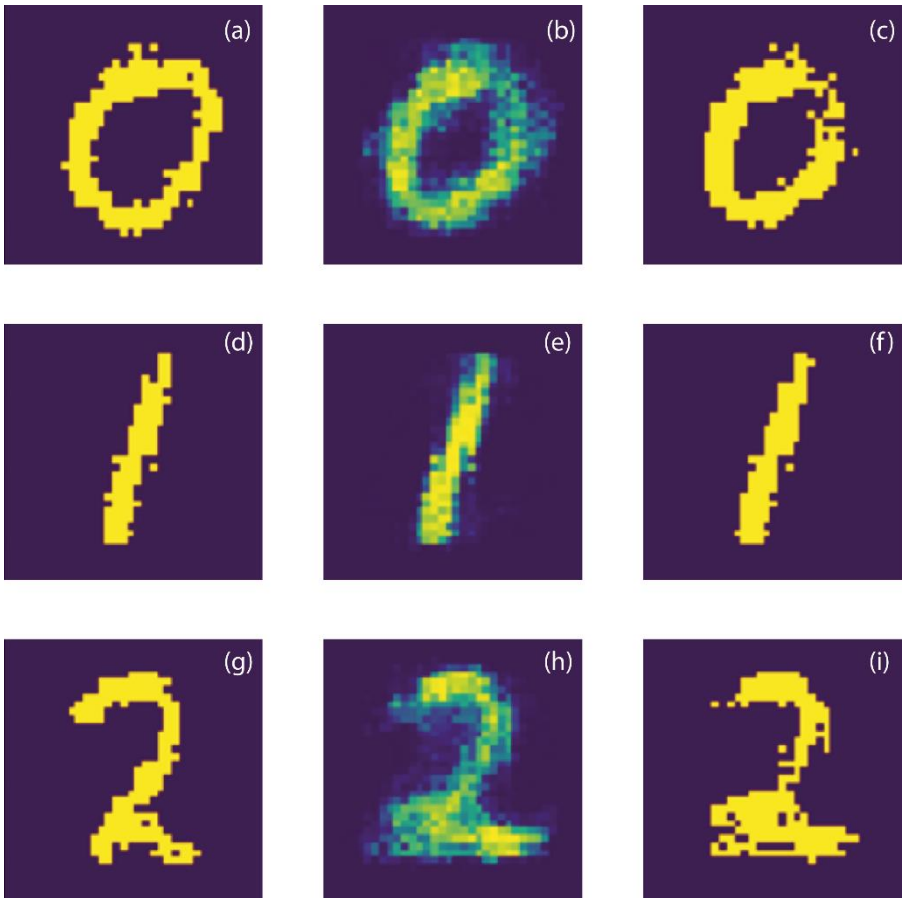

Fig. 6.3. Retrieved results by CNN. (a) Original pattern of 0; (b) Recovery result by CNN for (a); (c) Thresholding result of (b); (d) Original pattern of 1; (e) Recovery result by CNN for (d); (f) Thresholding result of (e); (g) Original pattern of 2; (h) Recovery result by CNN for (g); (i) Thresholding result of (h);

further processed with thresholding. The direct results by CNN are not extremely accurate but one can still clearly recognise the original numbers. By post-processing such as thresholding, the final retrieved patterns are highly consistent with the original ones with recovery accuracy over 90%. However, further experiments with more complicated patterns need to be done to testify this approach. Although this method opens a new way to calibrate the MMF imaging system, it does not solve the more fundamental flexibility problem due to fibre bending. Further thoughts on this scheme are whether fibre bending can be included as a variable in this CNN. If it is doable, then it is possible to train the model with a great amount of experimental data including the change of fibre bending degree. The resulted CNN may, therefore, be able to infer input images even with fibre bending to some degree. However, since the MMF is extremely sensitive and there is a great number of degrees of freedom on fibre deformation. A great deal of training data would be necessary in this case. Otherwise, one may want to limit the range of fibre bending in the initial stage to simplify the experiments.

References

1. Wang L, Ho P, Liu C, Zhang G, Alfano R. Ballistic 2-D imaging through scattering walls using an ultrafast optical kerr gate. *Science*. 1991:769-771.

2. Huang D, Swanson EA, Lin CP, et al. Optical coherence tomography. *Science*. 1991;254(5035):1178-1181.

3. Gibson A, Hebden J, Arridge SR. Recent advances in diffuse optical imaging. *Phys Med Biol*. 2005;50(4):R1.

4. Helmchen F, Denk W. Deep tissue two-photon microscopy. *Nature methods*. 2005;2(12):932-940.

5. Alex A, Považay B, Hofer B, et al. Multispectral in vivo three-dimensional optical coherence tomography of human skin. *J Biomed Opt*. 2010;15(2):026025-026025-15.

6. Vellekoop IM, Mosk A. Focusing coherent light through opaque strongly scattering media. *Opt Lett*. 2007;32(16):2309-2311.

7. Vellekoop I, Mosk A. Phase control algorithms for focusing light through turbid media. *Opt Commun*. 2008;281(11):3071-3080.

8. Vellekoop IM, Lagendijk A, Mosk A. Exploiting disorder for perfect focusing. *Nature photonics*. 2010;4(5):320-322.

9. Van Putten E, Akbulut D, Bertolotti J, Vos WL, Lagendijk A, Mosk A. Scattering lens resolves sub-100 nm structures with visible light. *Phys Rev Lett*. 2011;106(19):193905.

10. Aulbach J, Gjonaj B, Johnson PM, Mosk AP, Lagendijk A. Control of light transmission through opaque scattering media in space and time. *Phys Rev Lett*. 2011;106(10):103901.

11. Mosk AP, Lagendijk A, Lerosey G, Fink M. Controlling waves in space and time for imaging and focusing in complex media. *Nature photonics*. 2012;6(5):283-292.

12. Vellekoop IM, Mosk A. Universal optimal transmission of light through disordered materials. *Phys Rev Lett*. 2008;101(12):120601.

13. Katz O, Small E, Bromberg Y, Silberberg Y. Focusing and compression of ultrashort pulses through scattering media. *Nature photonics*. 2011;5(6):372-377.

14. McCabe DJ, Tajalli A, Austin DR, et al. Spatio-temporal focusing of an ultrafast pulse through a multiply scattering medium. *Nat Commun*. 2011;2:447.

15. Katz O, Small E, Silberberg Y. Looking around corners and through thin turbid layers in real time with scattered incoherent light. *Nature photonics*. 2012;6(8):549-553.

16. Guan Y, Katz O, Small E, Zhou J, Silberberg Y. Polarization control of multiply scattered light through random media by wavefront shaping. *Opt Lett*. 2012;37(22):4663-4665.

17. Čižmár T, Mazilu M, Dholakia K. In situ wavefront correction and its application to micromanipulation. *Nature Photonics*. 2010;4(6):388-394.

18. Dholakia K, Čižmár T. Shaping the future of manipulation. *Nature Photonics*. 2011;5(6):335-342.

19. Yaqoob Z, Psaltis D, Feld MS, Yang C. Optical phase conjugation for turbidity suppression in biological samples. *Nature photonics*. 2008;2(2):110-115.

20. Cui M, Yang C. Implementation of a digital optical phase conjugation system and its application to study the robustness of turbidity suppression by phase conjugation. *Optics express*. 2010;18(4):3444-3455.

21. Vellekoop IM, Cui M, Yang C. Digital optical phase conjugation of fluorescence in turbid tissue. *Appl Phys Lett*. 2012;101(8):081108.

22. Jang M, Sentenac A, Yang C. Optical phase conjugation (OPC)-assisted isotropic focusing. *Optics express*. 2013;21(7):8781-8792.

23. Wang D, Zhou EH, Brake J, Ruan H, Jang M, Yang C. Focusing through dynamic tissue with millisecond digital optical phase conjugation. *Optica*. 2015;2(8):728-735.

24. Popoff S, Lerosey G, Carminati R, Fink M, Boccara A, Gigan S. Measuring the transmission matrix in optics: An approach to the study and control of light propagation in disordered media. *Phys Rev Lett*. 2010;104(10):100601.

25. Popoff S, Lerosey G, Fink M, Boccara AC, Gigan S. Controlling light through optical disordered media: Transmission matrix approach. *New Journal of Physics*. 2011;13(12):123021.

26. Popoff S, Lerosey G, Fink M, Boccara AC, Gigan S. Image transmission through an opaque material. *arXiv preprint arXiv:1005.0532*. 2010.

27. Liutkus A, Martina D, Popoff S, et al. Imaging with nature: Compressive imaging using a multiply scattering medium. *Sci Rep*. 2014;4:5552.

28. Pierrat R, Ambichl P, Gigan S, Haber A, Carminati R, Rotter S. Invariance property of wave scattering through disordered media. *Proc Natl Acad Sci U S A*. 2014;111(50):17765-17770.

29. Small E, Katz O, Guan Y, Silberberg Y. Spectral control of broadband light through random media by wavefront shaping. *Opt Lett*. 2012;37(16):3429-3431.

30. Andreoli D, Volpe G, Popoff S, Katz O, Gresillon S, Gigan S. Deterministic control of broadband light through a multiply scattering medium via the multispectral transmission matrix. *Sci Rep*. 2015;5:10347.

31. Choi Y, Yoon C, Kim M, Choi W, Choi W. Optical imaging with the use of a scattering lens. *IEEE Journal of Selected Topics in Quantum Electronics*. 2014;20(2):61-73.

32. Kim M, Choi W, Choi Y, Yoon C, Choi W. Transmission matrix of a scattering medium and its applications in biophotonics. *Optics express*. 2015;23(10):12648-12668.

33. Choi Y, Yang TD, Fang-Yen C, et al. Overcoming the diffraction limit using multiple light scattering in a highly disordered medium. *Phys Rev Lett*. 2011;107(2):023902.

34. Park Y, Choi W, Yaqoob Z, Dasari R, Badizadegan K, Feld MS. Speckle-field digital holographic microscopy. *Optics express*. 2009;17(15):12285-12292.

35. Choi Y, Kim M, Yoon C, Yang TD, Lee KJ, Choi W. Synthetic aperture microscopy for high resolution imaging through a turbid medium. *Opt Lett*. 2011;36(21):4263-4265.

36. Choi Y, Hillman TR, Choi W, et al. Measurement of the time-resolved reflection matrix for enhancing light energy delivery into a scattering medium. *Phys Rev Lett*. 2013;111(24):243901.

37. Choi W, Mosk AP, Park Q, Choi W. Transmission eigenchannels in a disordered medium. *Physical Review B*. 2011;83(13):134207.

38. Kim M, Choi Y, Yoon C, et al. Maximal energy transport through disordered media with the implementation of transmission eigenchannels. *Nature photonics*. 2012;6(9):581-585.

39. Conkey DB, Caravaca-Aguirre AM, Piestun R. High-speed scattering medium characterization with application to focusing light through turbid media. *Optics express*. 2012;20(2):1733-1740.

40. Lee W. Binary computer-generated holograms. *Appl Opt*. 1979;18(21):3661-3669.

41. Nixon M, Katz O, Small E, et al. Real-time wavefront shaping through scattering media by all-optical feedback. *Nature Photonics*. 2013;7(11):919-924.

42. Vellekoop IM, Aegerter CM. Scattered light fluorescence microscopy: Imaging through turbid layers. *Opt Lett*. 2010;35(8):1245-1247.

43. Bertolotti J, van Putten EG, Blum C, Lagendijk A, Vos WL, Mosk AP. Non-invasive imaging through opaque scattering layers. *Nature*. 2012;491(7423):232-234.

44. Katz O, Heidmann P, Fink M, Gigan S. Non-invasive single-shot imaging through scattering layers and around corners via speckle correlations. *Nature photonics*. 2014;8(10):784-790.

45. Katz O, Small E, Guan Y, Silberberg Y. Noninvasive nonlinear focusing and imaging through strongly scattering turbid layers. *Optica*. 2014;1(3):170-174.

46. Freund I, Rosenbluh M, Feng S. Memory effects in propagation of optical waves through disordered media. *Phys Rev Lett*. 1988;61(20):2328.

47. Feng S, Kane C, Lee PA, Stone AD. Correlations and fluctuations of coherent wave transmission through disordered media. *Phys Rev Lett*. 1988;61(7):834.

48. Freund I. Looking through walls and around corners. *Physica A: Statistical Mechanics and its Applications*. 1990;168(1):49-65.

49. Goodman JW. *Speckle phenomena in optics: Theory and applications.* Roberts and Company Publishers; 2007.

50. Fienup JR. Phase retrieval algorithms: A comparison. *Appl Opt*. 1982;21(15):2758-2769.

51. Conkey DB, Brown AN, Caravaca-Aguirre AM, Piestun R. Genetic algorithm optimization for focusing through turbid media in noisy environments. *Optics express*. 2012;20(5):4840-4849.

52. Hsieh C, Pu Y, Grange R, Laporte G, Psaltis D. Imaging through turbid layers by scanning the phase conjugated second harmonic radiation from a nanoparticle. *Optics express*. 2010;18(20):20723-20731.

53. Gmitro AF, Aziz D. Confocal microscopy through a fiber-optic imaging bundle. *Opt Lett*. 1993;18(8):565-567.

54. Chen X, Reichenbach KL, Xu C. Experimental and theoretical analysis of core-to-core coupling on fiber bundle imaging. *Optics express*. 2008;16(26):21598-21607.

55. Choi Y, Yoon C, Kim M, et al. Scanner-free and wide-field endoscopic imaging by using a single multimode optical fiber. *Phys Rev Lett*. 2012;109(20):203901.

56. Yoon C, Choi Y, Kim M, Moon J, Kim D, Choi W. Experimental measurement of the number of modes for a multimode optical fiber. *Opt Lett*. 2012;37(21):4558-4560.

57. Choi Y, Yoon C, Kim M, Yang J, Choi W. Disorder-mediated enhancement of fiber numerical aperture. *Opt Lett*. 2013;38(13):2253-2255.

58. Kim D, Moon J, Kim M, et al. Toward a miniature endomicroscope: Pixelation-free and diffraction-limited imaging through a fiber bundle. *Opt Lett*. 2014;39(7):1921-1924.

59. Papadopoulos IN, Farahi S, Moser C, Psaltis D. Focusing and scanning light through a multimode optical fiber using digital phase conjugation. *Optics express*. 2012;20(10):10583-10590.

60. Papadopoulos IN, Farahi S, Moser C, Psaltis D. High-resolution, lensless endoscope based on digital scanning through a multimode optical fiber. *Biomedical optics express*. 2013;4(2):260-270.

61. Čižmár T, Mazilu M, Dholakia K. In situ wavefront correction and its application to micromanipulation. *Nature Photonics*. 2010;4(6):388-394.

62. Čižmár T, Dholakia K. Shaping the light transmission through a multimode optical fibre: Complex transformation analysis and applications in biophotonics. *Optics Express*. 2011;19(20):18871-18884.

63. Plöschner M, Čižmár T. Compact multimode fiber beam-shaping system based on GPU accelerated digital holography. *Opt Lett*. 2015;40(2):197-200.

64. Cizmar T, Dholakia K. Exploiting multimode waveguides for pure fibre-based imaging. *Nat Commun*. 2012;3:1027.

65. Kim G, Menon R. An ultra-small three dimensional computational microscope. *Appl Phys Lett*. 2014;105(6):061114.

66. Kim G, Domínguez-Caballero JA, Menon R. Design and analysis of multi-wavelength diffractive optics. *Optics express*. 2012;20(3):2814-2823.

67. Kim G, Nagarajan N, Capecchi MR, Menon R. Cannula-based computational fluorescence microscopy. *Appl Phys Lett*. 2015;106(26):261111.

68. Papadopoulos IN, Farahi S, Moser C, Psaltis D. Increasing the imaging capabilities of multimode fibers by exploiting the properties of highly scattering media. *Opt Lett*. 2013;38(15):2776-2778.

69. Laporte GP, Stasio N, Moser C, Psaltis D. Enhanced resolution in a multimode fiber imaging system. *Optics express*. 2015;23(21):27484-27493.

70. Mahalati RN, Gu RY, Kahn JM. Resolution limits for imaging through multi-mode fiber. *Optics express*. 2013;21(2):1656-1668.

71. Bianchi S, Rajamanickam V, Ferrara L, Di Fabrizio E, Liberale C, Di Leonardo R. Focusing and imaging with increased numerical apertures through multimode fibers with micro-fabricated optics. *Opt Lett*. 2013;38(23):4935-4938.

72. Loterie D, Farahi S, Papadopoulos I, Goy A, Psaltis D, Moser C. Digital confocal microscopy through a multimode fiber. *Optics express*. 2015;23(18):23845-23858.

73. Loterie D, Goorden SA, Psaltis D, Moser C. Confocal microscopy through a multimode fiber using optical correlation. *Opt Lett*. 2015;40(24):5754-5757.

74. Farahi S, Ziegler D, Papadopoulos IN, Psaltis D, Moser C. Dynamic bending compensation while focusing through a multimode fiber. *Optics express*. 2013;21(19):22504-22514.

75. Caravaca-Aguirre AM, Niv E, Conkey DB, Piestun R. Real-time resilient focusing through a bending multimode fiber. *Optics express*. 2013;21(10):12881-12887.

76. Caravaca-Aguirre AM, Piestun R. Single multimode fiber endoscope. *Optics Express*. 2017;25(3):1656-1665.

77. Loterie D, Psaltis D, Moser C. Bend translation in multimode fiber imaging. *Optics Express*. 2017;25(6):6263-6273.

78. Gu RY, Mahalati RN, Kahn JM. Design of flexible multi-mode fiber endoscope. *Optics express*. 2015;23(21):26905-26918.

79. Plöschner M, Tyc T, Čižmár T. Seeing through chaos in multimode fibres. *Nature Photonics*. 2015;9(8):529-535.

80. Kolenderska SM, Katz O, Fink M, Gigan S. Scanning-free imaging through a single fiber by random spatio-spectral encoding. *Opt Lett*. 2015;40(4):534-537.

81. Segev M, Silberberg Y, Christodoulides DN. Anderson localization of light. *Nature Photonics*. 2013;7(3):197-204.

82. Karbasi S, Mirr CR, Frazier RJ, Yarandi PG, Koch KW, Mafi A. Detailed investigation of the impact of the fiber design parameters on the transverse anderson localization of light in disordered optical fibers. *Optics express*. 2012;20(17):18692-18706.

83. Karbasi S, Frazier RJ, Koch KW, Hawkins T, Ballato J, Mafi A. Image transport through a disordered optical fiber mediated by transverse anderson localization. *arXiv preprint arXiv:1307.4160*. 2013.

84. Amitonova LV, Mosk AP, Pinkse PW. Rotational memory effect of a multimode fiber. *Optics express*. 2015;23(16):20569-20575.

85. Stasio N, Moser C, Psaltis D. Calibration-free imaging through a multicore fiber using speckle scanning microscopy. *Opt Lett*. 2016;41(13):3078-3081.

86. Porat A, Andresen ER, Rigneault H, Oron D, Gigan S, Katz O. Widefield lensless imaging through a fiber bundle via speckle correlations. *Optics express*. 2016;24(15):16835-16855.

87. Goodman JW. *Introduction to fourier optics.* Roberts and Company Publishers; 2005.

88. Cvijetic M, Djordjevic I. *Advanced optical communication systems and networks.* Artech House; 2013.

89. Igarashi K, Souma D, Tsuritani T, Morita I. Performance evaluation of selective mode conversion based on phase plates for a 10-mode fiber. *Optics express*. 2014;22(17):20881-20893.

90. Lee CM, Engelbrecht CJ, Soper TD, Helmchen F, Seibel EJ. Scanning fiber endoscopy with highly flexible, 1 mm catheterscopes for wide-field, full-color imaging. *Journal of biophotonics*. 2010;3(5-6):385-407.

91. Gu RY, Mahalati RN, Kahn JM. Noise-reduction algorithms for optimization-based imaging through multi-mode fiber. *Optics express*. 2014;22(12):15118-15132.

92. Gaskill JD. Linear systems, fourier transforms, and optics. *Linear Systems, Fourier Transforms, and Optics by Jack D.Gaskill New York, NY: John Wiley and Sons, 1978*. 1978;1.

93. Scherzer O. *Handbook of mathematical methods in imaging.* Springer Science & Business Media; 2010.

94. Kim MK. Digital holographic microscopy. In: *Digital holographic microscopy.* Springer; 2011:149-190.

95. Psaltis D, Moser C. Imaging with multimode fibers. *Opt Photonics News*. 2016;27(1):24-31.

96. Drémeau A, Krzakala F. Phase recovery from a bayesian point of view: The variational approach. . 2015:3661-3665.

97. Bernardo J, Bayarri M, Berger J, et al. The variational bayesian EM algorithm for incomplete data: With application to scoring graphical model structures. *Bayesian statistics*. 2003;7:453-464.

98. Rosen S, Gilboa D, Katz O, Silberberg Y. Focusing and scanning through flexible multimode fibers without access to the distal end. *arXiv preprint arXiv:1506.08586*. 2015.

99. Saffman M, Anderson DZ. Mode multiplexing and holographic demultiplexing communication channels on a multimode fiber. *Opt Lett*. 1991;16(5):300-302.

100. Stuart HR. Dispersive multiplexing in multimode optical fiber. *Science*. 2000;289(5477):281-283.

101. Tai AM, Friesem A. Transmission of two-dimensional images through a single optical fiber by wavelength–time encoding. *Opt Lett*. 1983;8(1):57-59.

102. Teich MC, Saleh B. Fundamentals of photonics. *Canada, Wiley Interscience*. 1991;3.